UNIVERSITY OF ROCHESTER
LABORATORY FOR LASER ENERGETICS

Volume 68
July–September 1996
DOE/SF/19460-139

LLE Review

Quarterly Report

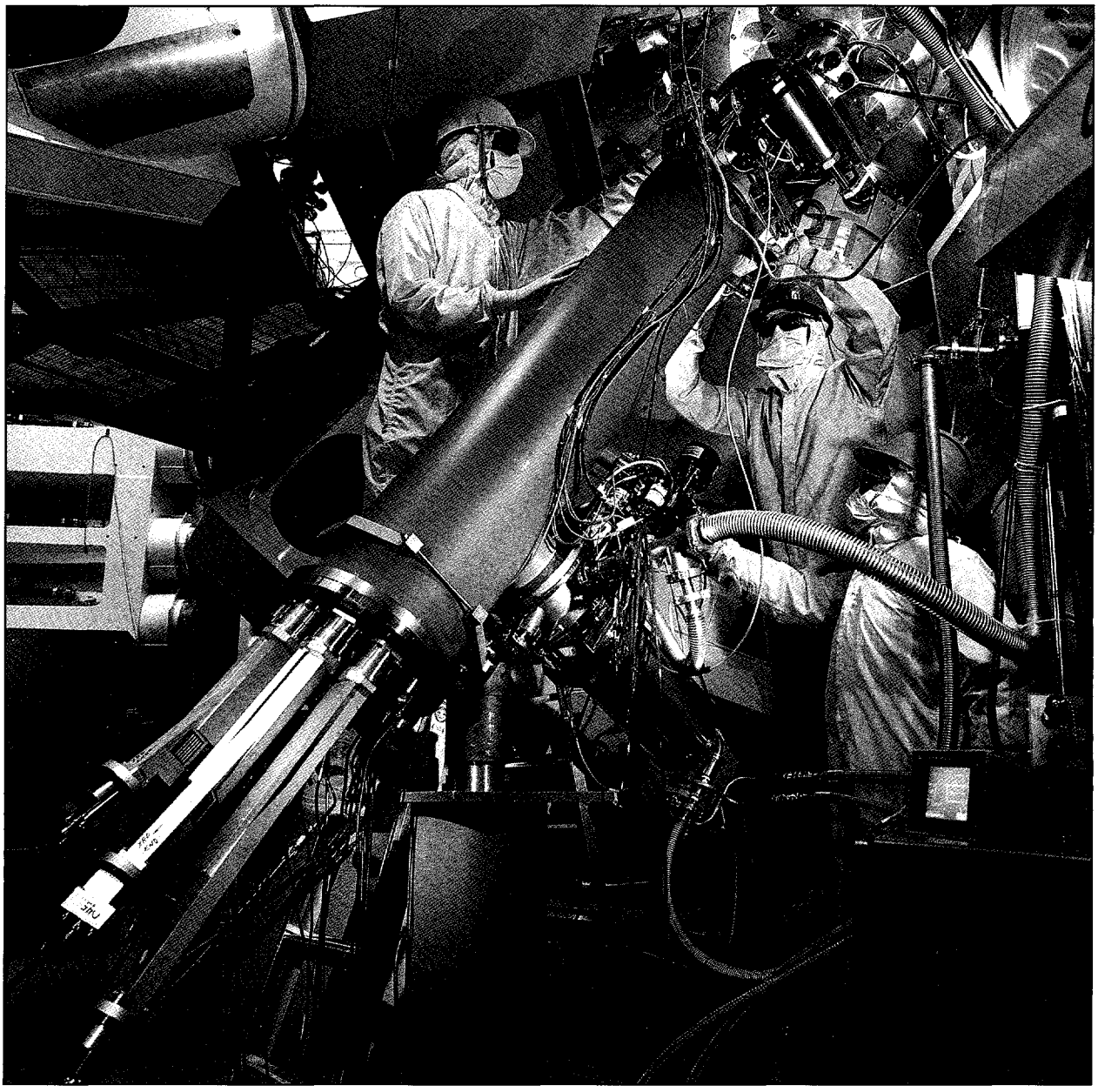

About the Cover:

Lance Lund, LLE research engineer (left), Robert Costa, LLNL technologist (center), and Greg Pien, LLE senior lab engineer (lower right), install the DANTE diagnostic into the OMEGA target chamber. This instrument, a 12-channel, soft x-ray diode array with multigigahertz bandwidth, was used to measure hohlraum temperatures during a proof-of-principle series of indirect-drive experiments. These experiments, carried out in collaboration with LANL and LLNL, demonstrated the feasibility of using OMEGA to study indirect drive.

The work described in this volume includes current research at the Laboratory for Laser Energetics, which is supported by New York State Energy Research and Development Authority, the University of Rochester, the U.S. Department of Energy Office of Inertial Confinement Fusion under Cooperative Agreement No. DE-FC03-92SF19460, and other agencies.

Printed in the United States of America
Available from
National Technical Information Services
U.S. Department of Commerce
5285 Port Royal Road
Springfield, VA 22161

Price codes: Printed Copy A04
Microfiche A01

For questions or comments, contact Mark D. Skeldon, *Editor*, Laboratory for Laser Energetics, 250 East River Road, Rochester, NY 14623-1299, (716) 275-4781.

UNIVERSITY OF ROCHESTER
LABORATORY FOR LASER ENERGETICS

Volume 68
July–September 1996
DOE/SF/19460-139

LLE Review

Quarterly Report

UR LLE

Contents

In Brief

This volume of the LLE Review, covering the period of July–September 1996, includes a description of an important experiment carried out on OMEGA by researchers from LANL, LLNL, and LLE to demonstrate the feasibility of using OMEGA for indirect drive. Additional topics include tetrahedral hohlraums, the speckle properties of phase-converted laser beams, design criteria for SSD phase modulators, and the design of slab amplifiers.

Highlights of the research presented in this issue are

- Results from the proof-of-principle indirect-drive experiments in which up to 40 OMEGA beams were used to irradiate cylindrical hohlraums. Nova results were reproduced, and new capabilities not available on other lasers were demonstrated.

- A discussion of tetrahedral hohlraums (spherical hohlraums with four laser entrance holes) as a means of achieving better capsule irradiation uniformity. Tetrahedral hohlraums also allow the use of all 60 OMEGA beams and may provide an alternate route to ignition on the NIF.

- An analysis of the residual target irradiation nonuniformity due to the fine laser speckle remaining on the beam after being phase converted by the DPP's. A model shows how a uniformly ablating plasma atmosphere reduces the speckle contribution to the effective time-averaged irradiation nonuniformity.

- A discussion of the theory, design, manufacture, testing, and implementation of the microwave SSD phase modulators used on OMEGA for two-dimensional SSD. The modulators are capable of operating in the gigahertz frequency range.

- A discussion of the design and performance of a large-aperture, high-gain Nd:glass zig-zag slab amplifier for materials testing. The design incorporates improvements from previous work in addition to improvements obtained from careful design choices guided by analytic calculations.

Mark D. Skeldon
Editor

Proof-of-Principle Hohlraum Experiments

During a two-week period in June 1996 researchers from LANL, LLNL, and LLE performed experiments to demonstrate the utility of OMEGA for indirect drive. The main objectives of these experiments, which were all accomplished, were to verify the ability of the OMEGA system to perform hohlraum experiments, to reproduce results obtained with the Nova laser, and to demonstrate new capabilities not available on other lasers.

A total of 42 shots were taken, and the target performance was diagnosed using six x-ray pinhole cameras, two x-ray microscopes, three x-ray framing cameras, DANTE (time-resolved, absolutely calibrated soft x-ray emission), neutron yield and neutron time-of-flight detectors, a single-hit neutron detector array, and a number of other laser and plasma diagnostics. This represents one of the largest arrays of diagnostics ever fielded on a hohlraum target campaign to date.

These experiments took advantage of a number of capabilities recently added to OMEGA including pulse shaping and a new 10-in. manipulator (TIM 4). The experiments were also the first on OMEGA to simultaneously use three framing cameras. Most of these experiments were carried out using 1-ns square pulses, with 500 J per beam delivered to the target. A small number of shots were taken for pointing tests using 160-ps Gaussian pulses, with a peak power of ~0.5 TW per beam.

The targets consisted of thin-wall Nova "scale-one" hohlraums[1] mounted at an angle to the stalk of 63.4° (as opposed to 90° on Nova). The hohlraums were of 2100- to 2800-μm inside length and 1600-μm inside diameter. The walls were made of 100 μm of epoxy with a gold lining. The gold thickness was 1 μm for the pointing shots on the first shot day, but 2 μm for the rest of the shots. The laser entrance holes (LEH's) were 1200 μm in diameter except for two shots that had 900-μm-diam LEH's.

The beams were arranged in three beam cones on each side of the hohlraum, consisting of five, five, and ten beams, respectively, centered on a pentagonal diagnostic port. The half-angles of the beam cones were 21.42°, 42.02°, and 58.85° (see Fig. 68.1). (A fourth beam cone of half-angle 81.25° was not useful for these experiments since these beams cannot make it

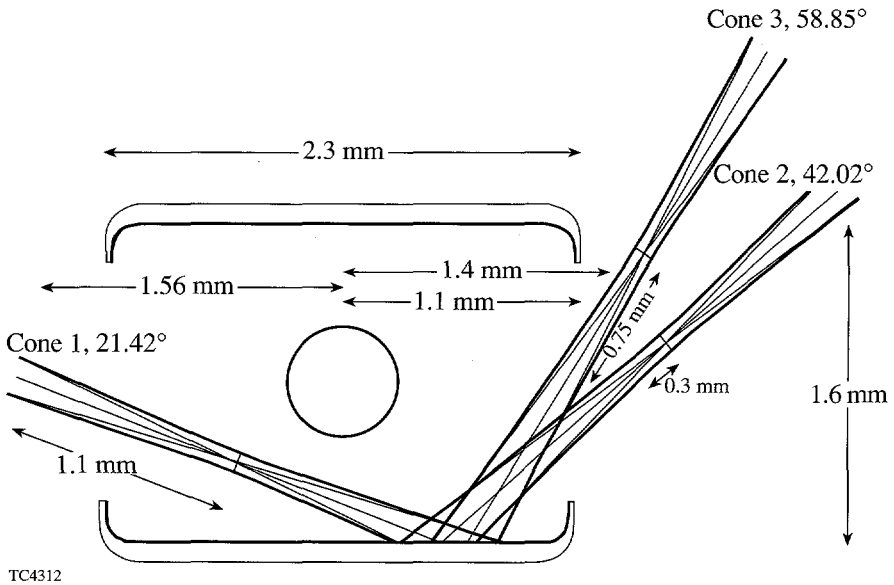

Figure 68.1
Target design and typical beam pointing for the first set of indirect-drive experiments on OMEGA.

through the LEH for cylindrical hohlraums.) Experiments were performed with some or all of the beam cones. Cones 2 and 3 were used for most experiments, with cone 1 used for a few as well. For diagnostic reasons, the hohlraums were aligned along two different axes (each passing through the centers of a ring of five beams) during the experiments.

The positions of the beams were specified by the distance from the center of the hohlraum to the point where the beams cross the axis of the hohlraum. This is referred to as the beam pointing. The focusing of the beams is referenced to that crossing point. If the best focus position is moved back toward the lens, then the defocusing is negative; if it is moved away from the lens, the defocusing is positive. The defocusing distances for these shots were set so that a beam containing 650 J would give about 10^{15} W/cm^2 on the wall of the hohlraum (Table 68.I), i.e., comparable intensities to those on Nova. The pointing was initially verified with two-sphere pointing targets consisting of two 1588-μm-diam plastic spheres coated with about 1 μm of gold (Fig. 68.2). For most of these shots, the spacing between the centers of the spheres was 2200 μm. The centers of the spheres corresponded to the pointing of cone 3 for the majority of the experiments. As a test of "dead reckoning" pointing, one two-sphere target with 2800-μm spacing was also shot after moving the beam pointing 300 μm for each beam cone.

The main purpose of the first series of experiments was to verify the ability of the system to point the beams. A short (160-ps FWHM) Gaussian laser pulse was used to illuminate a 2300-μm-long hohlraum. The targets were imaged with pinhole cameras from six locations allowing the beam positions to be verified. The results (see Fig. 68.3) indicated that the beams were pointed to their desired locations in the hohlraum to an accuracy of 30 μm.

Table 68.I Beam cone angles and defocusing distances.

	Cone Angle	Defocus
Cone 1	21.42°	+1100 μm
Cone 2	42.02°	−300 μm
Cone 3	58.85°	−750 μm

The next series of experiments was a set of symmetry scans[2] to verify the same dependence of hohlraum symmetry on beam pointing as was obtained with previous experiments on Nova. Hohlraums with lengths varying from 2100 μm to 2500 μm were used with standard plastic symmetry capsules (440-μm inside diameter, 55-μm wall thickness, 50-atm D_2 fill, 0.1-atm Ar). Time-integrated hohlraum symmetry was determined from the distortion of the imploded core as measured by gated x-ray images.

In the first experiment, two of the beam cones were pointed in such a way that they formed a single ring of beam spots on the interior wall of the hohlraum. The results from OMEGA were consistent with results of similar Nova experiments.

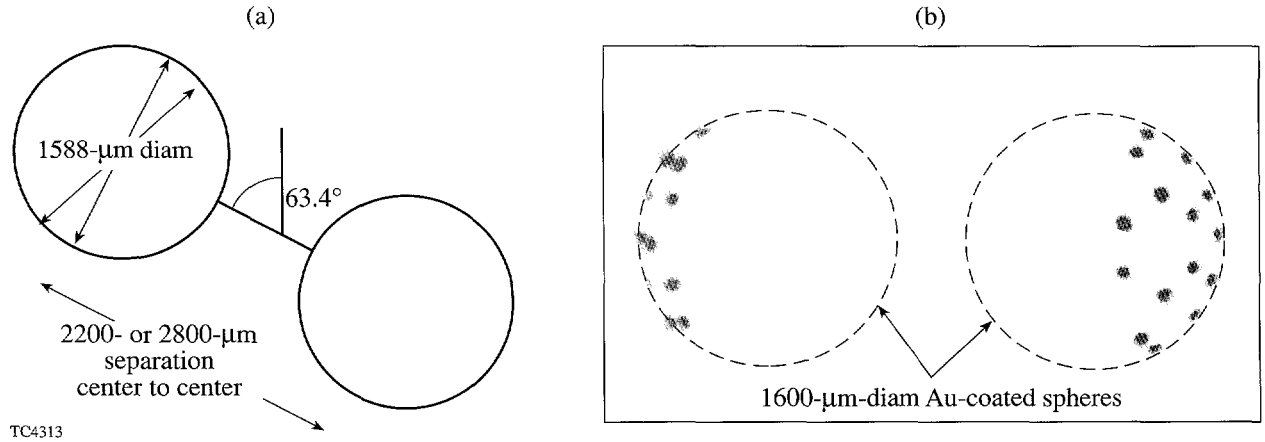

Figure 68.2
(a) Double-sphere pointing target used to verify beam pointing for indirect-drive experiments; (b) x-ray pinhole camera image from one such target.

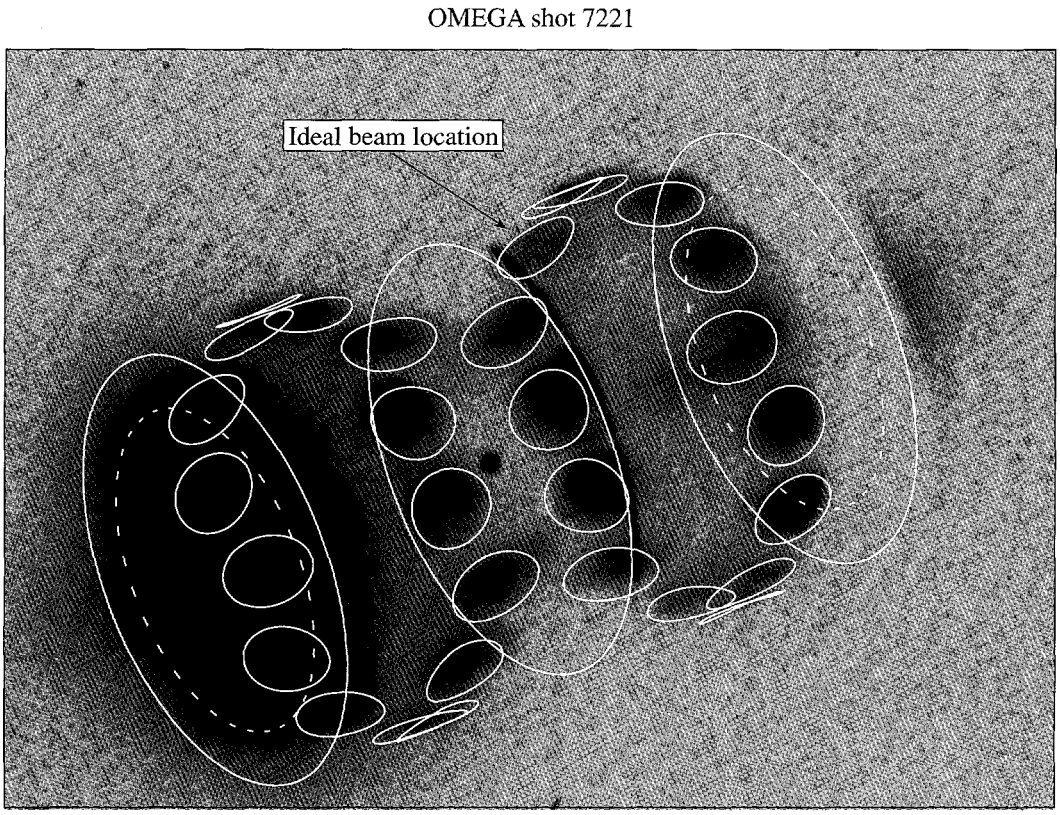

Figure 68.3
X-ray pinhole camera image of a thin-wall-hohlraum implosion target. The implosion core at the center of the hohlraum is clearly seen, as are the cut in the hohlraum midplane made when mounting the capsule, the beam spots, and the LEH on the left. The solid lines indicate the calculated locations of the laser spots, the LEH's, and the hohlraum midplane.

A different pointing scan was performed in which the pointing of beam cone 3 was held constant, while that of cone 2 was moved. A weighted spot position was then calculated, with the weight given by the number of beams in each ring and an inverse-square dependence on the distance to the center of the capsule. For one set of experiments, cone 1 was also added. The results (Fig. 68.4) indicate that, except for one experiment that utilized all three beam cones, the symmetry of the capsule is consistent with Nova results when the weighted spot position is used in place of the single-ring spot position from Nova experiments. Comparisons were also made when a simple model of spot motion[3] was included. Here, the wall was assumed to move inward by 150 μm, leading to motion of the spots toward the LEH for Nova and OMEGA cones 2 and 3, and toward the midplane of the hohlraum for OMEGA cone 1 [Fig. 68.4(b)].

Neutron yields were measured on all of the implosion experiments (Fig. 68.5) and found to be in agreement with yields from similar Nova experiments. Further, the dependence of yield on implosion symmetry was found to be similar for 15-kJ shots (a full scan was not carried out at 20 kJ). The highest yields were obtained for round (symmetric) implosions. When the drive was higher on the equator and a prolate implosion resulted, the yield dropped somewhat. A larger drop in the yield was seen in experiments with a pole-high drive resulting in an oblate implosion, consistent with Nova experiments.

A set of experiments were performed to measure the radiation drive produced in the hohlraum. For this purpose, a multichannel soft-x-ray spectrometer (DANTE) was moved from Nova to OMEGA. This spectrometer measured the flux exiting a diagnostic hole on the wall of the hohlraum and viewed an unilluminated portion of the interior wall of the hohlraum.

Several steps are necessary to reduce these data beyond those that are required to reduce Nova data. First, the thickness of the hohlraum wall must be included when calculating the apparent size of the diagnostic hole. The 100-μm thickness results in a "tunnel effect" when calculating the open area, which decreases the apparent hole size faster than a simple cosine dependence. In addition, since the diagnostic hole was not monitored with a framing camera for these experiments, the effects of hole closure must be calculated. The diagnostic holes on these targets were not lined since the wall was already made of a low-Z material (epoxy). However, the low-energy channels may have been affected by blowoff from the walls of

the hole. The results for radiation temperature, including the "tunnel effect" and effects of hole closure, are still lower than expected from Nova results and simple scalings. A number of other effects must be considered, and detailed analysis is in progress.

One of the advantages OMEGA has over Nova is the increased azimuthal symmetry due to the larger number of beams. By using beam cones 2 and 3 with the beams pointed to cross the hohlraum axis and form a single ring of beam spots, one obtains a nearly uniformly spaced set of 15 beam spots on each

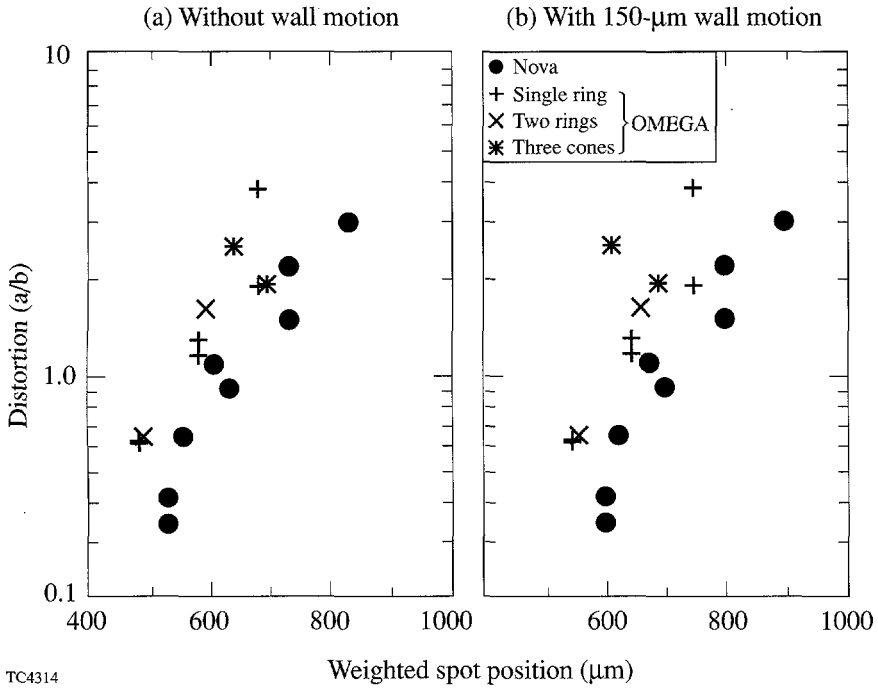

Figure 68.4
Distortion as a function of weighted spot position with and without a simple wall motion component included.

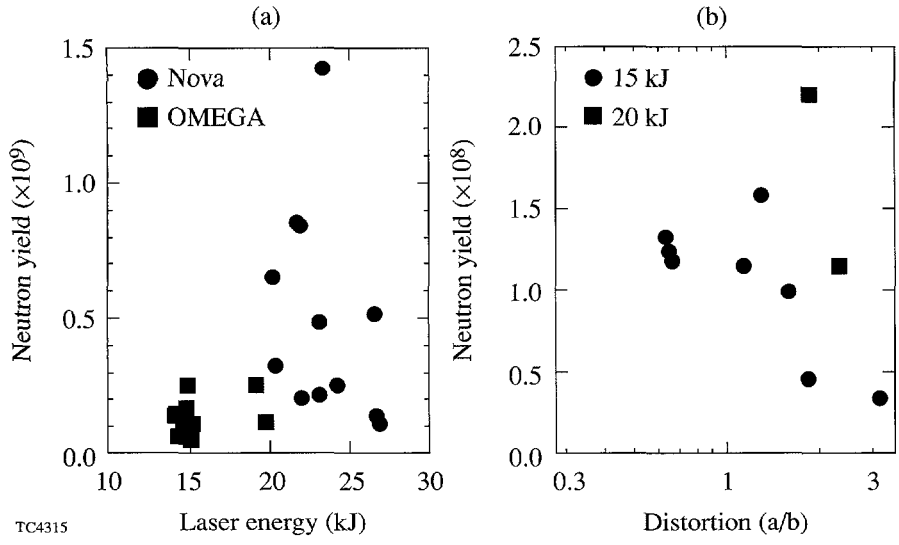

Figure 68.5
Yield as a function of (a) laser energy for OMEGA and Nova experiments, and (b) implosion distortion for OMEGA experiments. Neutron yields shown for the OMEGA experiments are approximate (±50%) and subject to change as a result of further calibration.

side of the hohlraum. Further, the rings on opposite sides are out of phase with each other so that a beam spot on one side of the hohlraum corresponds to a gap in the beams on the other.

A lack of comparable azimuthal symmetry on Nova, where there is a strong $m = 5$ beam pattern, may be responsible for some observed disagreements between Nova data and two-dimensional simulations. The $m = 15$ arrangement of the OMEGA beams offers the capability to test this hypothesis. Two sets of experiments were thus performed: one with the nominal $m = 15$ geometry, and the other with the beams moved to create an $m = 5$ geometry similar to that of Nova. A set of implosions were performed similar to the symmetry scans done previously. X-ray framing-camera imaging was, however, performed along the hohlraum axis. Preliminary inspection of the data shows that round implosion images were obtained in both cases. In the $m = 5$ case (Fig. 68.6) it is not possible to identify a clear $m = 5$ component in the radiation drive.

The $m = 5$ radiation pattern was also monitored with a reemission ball.[4] In these shots, a glass capsule coated with bismuth was substituted for the implosion capsule. As the bismuth heats up due to the impinging radiation from the hohlraum, it emits hard x rays in an amount dependent on its temperature. This method is particularly sensitive to early-time irradiation asymmetry. However, an image was obtained (Fig. 68.7) that again showed no clear $m = 5$ asymmetry.

An unanticipated feature of these experiments is the appearance of distinct stagnation features on the axis of the hohlraum. This stagnation is observable in the pinhole image in Fig. 68.3 but can be seen with greater clarity in the framing-camera images taken during the drive shots (Fig. 68.8). These are not usually seen on Nova and are attributed to the greater degree of symmetry available on OMEGA. Phenomena such as this will allow useful comparisons to be made with two-dimensional hohlraum simulations.

In summary, a wide range of indirect-drive experiments were successfully carried out on the OMEGA laser system. Results were generally consistent with the existing Nova database. Some of the experiments demonstrated unique features of the OMEGA system not available on Nova. Indirect-drive experiments will continue on an ongoing basis in collaboration with LLNL and LANL; those planned for the near future include beam phasing in cylindrical hohlraums and proof-of-principle experiments using tetrahedral hohlraums (see the following article).

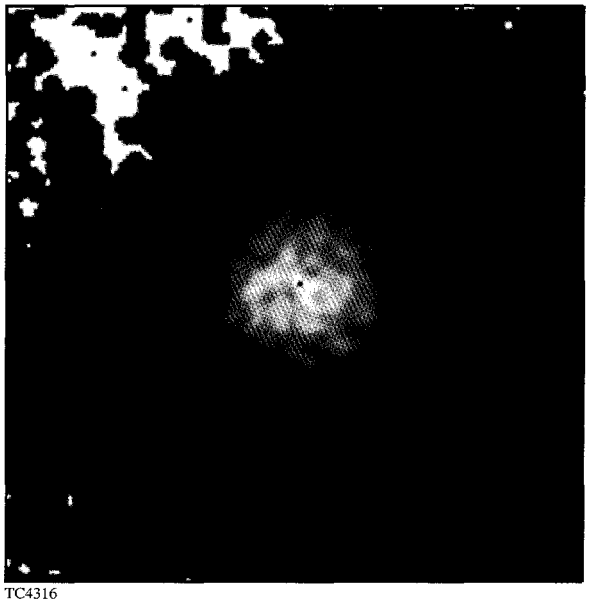
TC4316

Figure 68.6
Implosion image for an imposed $m = 5$ drive asymmetry, obtained from a framing camera viewing along the hohlraum axis.

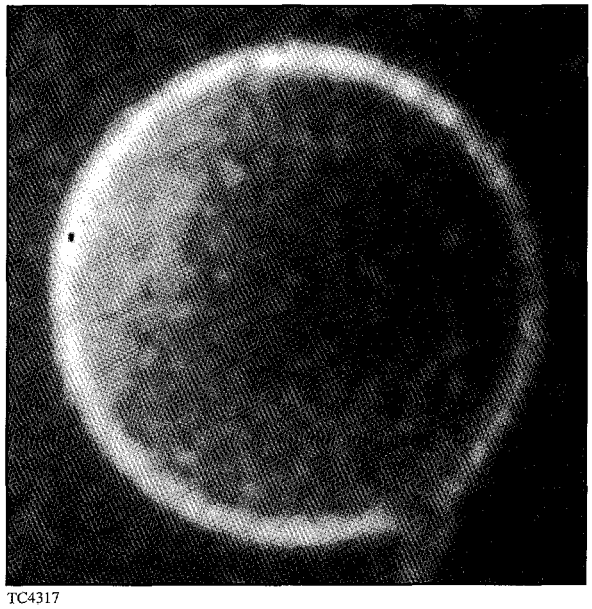
TC4317

Figure 68.7
Reemission image for an imposed $m = 5$ drive asymmetry, obtained from a framing camera viewing along the hohlraum axis.

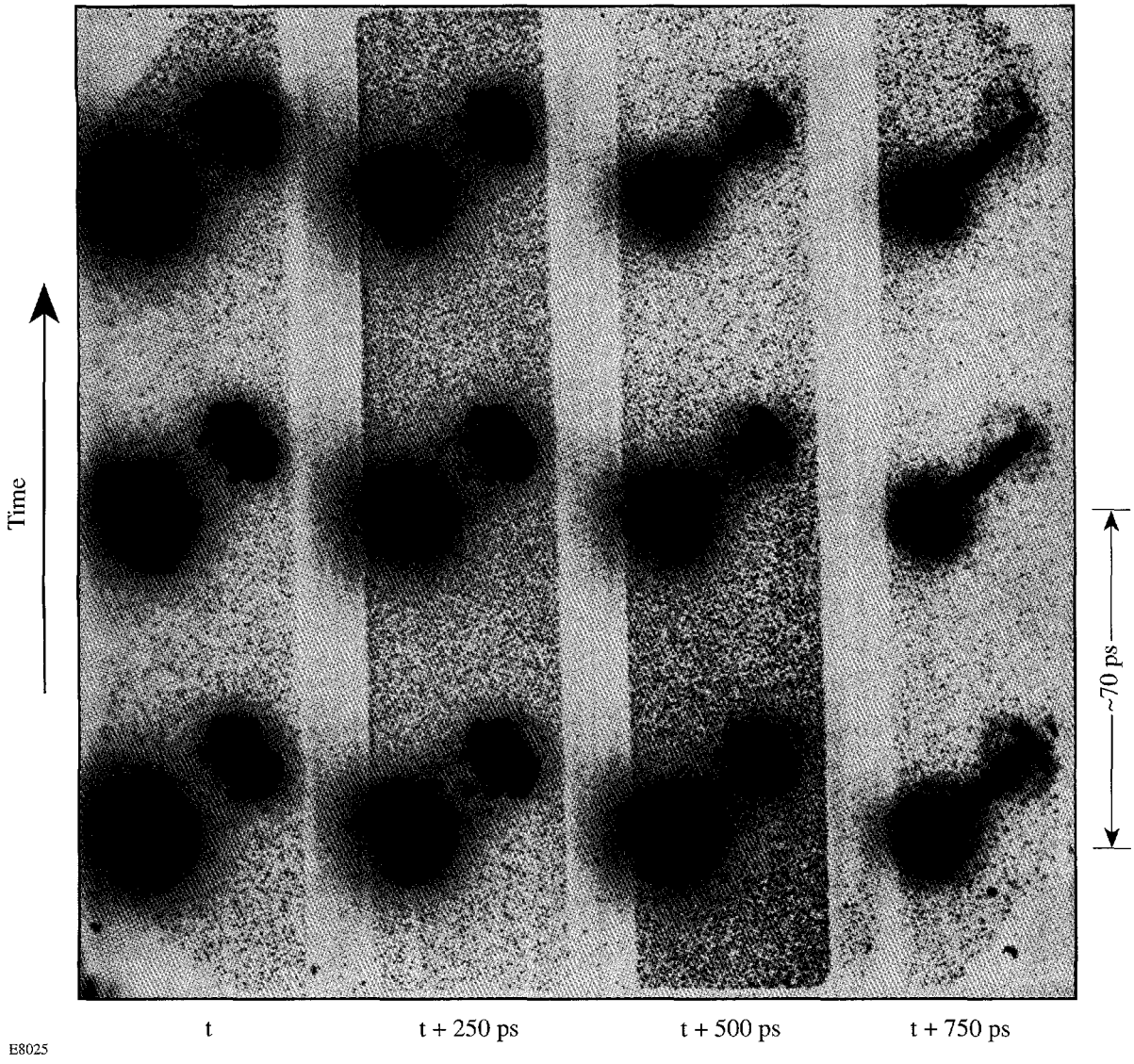

Figure 68.8
X-ray framing-camera images showing the formation of stagnation features on the axis of the hohlraum late in time.

ACKNOWLEDGMENT

This work was supported by the U.S. Department of Energy Office of Inertial Confinement Fusion under Cooperative Agreement No. DE-FC03-92SF19460, the University of Rochester, and the New York State Energy Research and Development Authority. The support of DOE does not constitute an endorsement by DOE of the views expressed in this article.

REFERENCES

1. N. D. Delamater *et al.*, Phys. Plasmas **3**, 2022 (1996).
2. A. Hauer *et al.*, Rev. Sci. Instrum. **66**, 672 (1995).
3. L. J. Suter *et al.*, Phys. Rev. Lett. **73**, 2328 (1994).
4. N. D. Delamater, G. R. Magelssen, and A. A. Hauer, Phys. Rev. E **53**, 5240 (1996).

Tetrahedral Hohlraums—An Alternative Approach to Indirect Drive on OMEGA and the NIF

The preceding article reported on the first indirect-drive experiments carried out on OMEGA, using cylindrical hohlraums. This article advocates the use of tetrahedral hohlraums, by which are understood spherical hohlraums with four laser entrance holes (LEH's) placed at or near the vertices of a tetrahedron. This alternative approach appears to be well suited to the OMEGA geometry and could offer an alternate route to ignition on the National Ignition Facility (NIF).

The primary advantage provided by the tetrahedral hohlraum is better radiation uniformity on the capsule. Historically, the cylindrical hohlraum[1] has been the preferred approach. Among the reasons for this may be that the cylindrical geometry is two-dimensional (2-D) and therefore permits detailed hydrodynamic modeling and optimization, while the tetrahedral hohlraum is intrinsically 3-D and thus not amenable to modeling with currently available hydrodynamic codes. However, a comparison between the two approaches is now possible using a new, 3-D view-factor code named *BUTTERCUP*. While this code does not include any hydrodynamics, it does enable reasonable predictions to be made for cylindrical and tetrahedral hohlraums on both OMEGA and the NIF.

On OMEGA, the target chamber geometry provides an exact tetrahedral symmetry, permitting the irradiation of tetrahedral hohlraums with all 60 beams. In comparison, only 40 beams can be used for cylindrical hohlraums. For the NIF, assuming that 72 ports are provided to accommodate direct drive (as is the current baseline), it will be possible to irradiate a tetrahedral hohlraum with 44 out of the 48 beams without in any way compromising the geometrical arrangement of beams required for cylindrical hohlraums or direct drive. On both laser systems, *BUTTERCUP* predicts that good irradiation uniformity (~2% rms) will be obtained on the capsule at all times during the implosion. This uniformity is relatively insensitive to albedo and other changing conditions inside the hohlraum. "Beam phasing" (the use of different temporal pulse shapes in different beams), which is required for cylindrical hohlraums, may not be necessary for tetrahedral hohlraums.

The cylindrical and tetrahedral geometries considered in this article are shown in Fig. 68.9. Each type of hohlraum can be irradiated on each laser system. The z axis is taken to lie along the hohlraum axis for conventional cylindrical hohlraums. This corresponds to the true vertical direction for the NIF, and to a pent-pent axis for the experiments on OMEGA described in the preceding article. The cylindrical hohlraum for OMEGA is a scale-1 Nova hohlraum. The tetrahedral hohlraums are viewed from different angles—from the vertical for the NIF and along a hex-hex axis for OMEGA. For tetrahedral hohlraums on OMEGA, each LEH faces a hexagon on the target chamber located at a vertex of a regular tetrahedron. The target chamber geometry permits ten distinct orientations of the hohlraum.

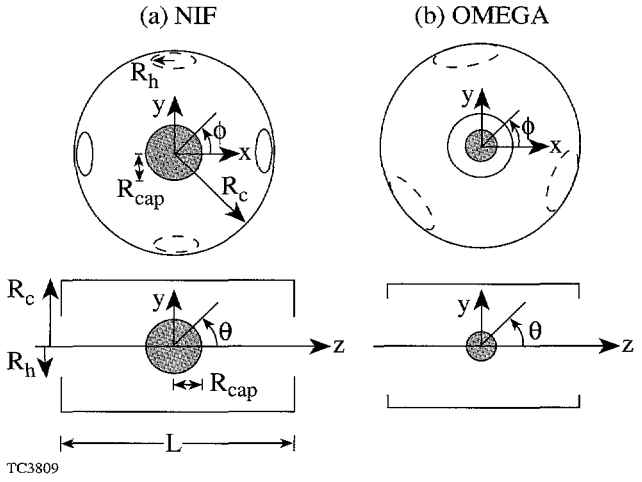

Figure 68.9
Tetrahedral and cylindrical hohlraums for (a) the NIF and (b) OMEGA with the capsule shown shaded. For each laser system the two hohlraums are drawn to the same scale. Tetrahedral hohlraums for the NIF are viewed from the vertical (z) direction and have laser entrance holes (LEH's) at $\theta = 55°$ and 125°. Those for OMEGA are viewed from one LEH, taken to define the z axis, and the other LEH's are arranged in tetrahedral symmetry with $\theta = 109.5°$; each LEH is aligned with a hexagonal face of the target chamber.

This article will review the issue of indirect-drive uniformity, describe the code *BUTTERCUP*, and present results for OMEGA and the NIF. Given the demonstrated ability of the OMEGA laser to perform precision indirect-drive experiments, as described in the preceding article, it is clear that OMEGA is uniquely capable of investigating the feasibility of tetrahedral hohlraums.

Indirect-Drive Uniformity

Many issues are crucial for the success of indirect-drive ICF. These include ensuring a high conversion efficiency of laser energy to x rays, ensuring that the laser energy can enter the hohlraum unimpeded by plasma ablating from around the laser entrance holes (LEH's), avoiding absorption of the laser energy into low-density plasma whether from the capsule or the wall, avoiding laser-plasma instabilities, tailoring the radiation drive on the capsule by designing a suitably shaped laser pulse, and maximizing the energy coupling into the capsule by making the capsule as large as possible and the LEH's as small as possible relative to the dimensions of the case. However, the most critical issue may be that of ensuring an acceptable level of radiation drive uniformity on the capsule.

In the standard cylindrical hohlraum, the uniformity issue is indeed critical. On the Nova laser at the Lawrence Livermore National Laboratory, for example, there are ten laser beams, five through each LEH, whose irradiation pattern on the inside of the case may be represented as two rings in a cylindrically symmetric geometry. In reality, of course, there are ten more or less distinct laser spots with some azimuthal asymmetry. The uniformity experienced by the capsule varies in three stages: (a) initially, the x-ray flux arises predominantly from the laser-irradiated spots; (b) later, the hohlraum wall "warms up," contributing a component with deficits at the poles of the capsule (the points that face the LEH's); and (c) still later, as plasma expands from the curved portion of the case, the laser energy is absorbed closer to the LEH's, an effect known as spot motion, and the component due to the laser-heated spots develops a surplus at the poles. These three stages of time-dependent uniformity have been well documented.[1–3] While these time-dependent nonuniformities may average out to a certain extent,[1] it is desirable to maintain good uniformity throughout the implosion. According to Refs. 1 and 4, the tolerable level of time-dependent nonuniformity may be of the order of 4%–10%, depending on the details of the target design, as long as the time-averaged uniformity is $\lesssim 1\%$. (In Ref. 5, however, it is asserted, based on a simplified, thin-shell hydrodynamic model, that time-dependent asymmetries should not exceed ±2%.) Another effect—laser-beam steering in gas-filled hohlraums (hohlraums filled with low-density, low-Z gas intended to prevent high-Z plasma from the walls from filling the hohlraum[1,4])—has also been identified as significant.[6]

In the base-line design[4] for a cylindrical hohlraum on the NIF, the 48 beams (each a two-by-two array of sub-beams) are arranged on the target chamber in eight rings, each corresponding to a different angle θ with respect to the vertical (z) direction in the target area. When focused onto the hohlraum wall, the rings overlap in pairs, so that the inner surface of the hohlraum is effectively irradiated with two rings in each of the north and south hemispheres. By varying the relative powers of the different rings ("beam phasing"),[1] it is possible to eliminate the P_2 spherical-harmonic component of irradiation nonuniformity on the capsule at all times and the P_4 component in the time-averaged sense. The desired beam power histories may be obtained through "integrated calculations," which include the two-dimensional hydrodynamic evolution of the hohlraum (assumed azimuthally symmetric) and detailed radiation transport.

The P_2 component of nonuniformity is avoided entirely in tetrahedral hohlraums. Using a geometric treatment, Phillion and Pollaine[7] found that with strict tetrahedral symmetry, all $l = 1$, 2, and 5 spherical-harmonic components are identically zero, regardless of spot motion, beam steering, or other real physical effects; in addition, with a combination of judiciously selected beam locations and beam phasing, the $l = 3$ and 4 components can be made to vanish at all times. Tetrahedral hohlraums thus offer improved uniformity compared with cylindrical hohlraums. Possible drawbacks include the following: (a) beam placements designed with true tetrahedral symmetry as in Ref. 7 would be incompatible with cylindrical hohlraums and thus with the NIF; (b) the hydrodynamics are harder to model as the configuration is 3-D rather than 2-D; (c) with four holes rather than two, there may be more radiation losses; and (d) there may be more LEH clearance problems. The tradeoff between these issues remains to be resolved. However, on the basis of uniformity considerations, this article suggests that the tetrahedral hohlraum may be a viable approach worth pursuing on the NIF, complementary to the cylindrical hohlraum.

Aside from Ref. 7, the tetrahedral geometry has been studied previously only to a limited extent. To the best of our knowledge, Azechi[8] was the first to describe it in the ICF literature. In this reference, the target was conceived as a "cannonball" target, in which the capsule would be imploded not by x rays but by the plasma ablated off the inside of the hohlraum wall. Spherical cannonball targets with 2, 4, and 12 holes are

described in Ref. 9, which also presents some tomographic x-ray images of the compressed core.

The cannonball approach was dropped in favor of the radiation-drive approach, where, for reasons of uniform capsule drive, it is necessary to avoid the wall plasma contributing to the drive on the capsule. For many years radiation drive was conceived in the literature as occurring with a spherical radiation case. (In 1990, though, Kato[10] published experimental work on cylindrical hohlraums that clearly demonstrated the importance of the $\ell = 2$ nonuniformity.) Mochizuki[11] considered two concentric spherical surfaces and calculated the geometrical smoothing associated with radiation emission from the outer to the inner surface. Murakami[12] extended this approach to use a spherical-harmonic decomposition of the radiation source on the case—each spherical-harmonic mode is damped by some appropriate factor to give the smoothed radiation drive on the capsule. Murakami gave examples for two-hole spherical hohlraums but did not include the contributions from portions of the case not irradiated directly by the laser beams; thus he did not consider nonuniformities on the capsule resulting from the finite size of the LEH's. The spherical-harmonic approach was also used in Ref. 7. Wilson[13] considered three- and four-hole spherical hohlraums from the point of view of distributing the laser-irradiated spots as uniformly as possible on the interior of the hohlraum wall. Murakami[14] used a view-factor code, close in spirit to the present work, to calculate the on-capsule uniformity in ellipsoidal and spherical cavities for ion-beam and laser drivers, respectively. Other work on radiation symmetrization is found in Ref. 15, which includes a model of the radiative heat wave moving into the wall; Ref. 16, which also considers a cylindrical hohlraum; and Ref. 17, which includes a treatment of the unirradiated hohlraum wall using a multiple-reemission smoothing factor.

The Code *BUTTERCUP*

The primary tool used in this article is the 3-D view-factor code *BUTTERCUP*. This code has been used to generate designs for cylindrical and tetrahedral hohlraums on both the NIF and the OMEGA laser systems. It considers the geometries shown in Fig. 68.9, which also serves to define some notation (the case radius R_c, the hole radius R_h, the capsule radius R_{cap}, and the conventional spherical angles θ and ϕ).

The code starts by tracing rays in 3-D from each laser beam, through the LEH's, and into the hohlraum. The rays are represented using a 2-D grid that covers the beam cross section. Typical beam paths into tetrahedral and cylindrical hohlraums are shown in Fig. 68.10. Each beam is calculated independently, allowing for independent energies, pointings, etc. No symmetries are assumed. The NIF beams are assumed to derive from phase plates and to comprise parallel rays in the far field with a 500×1000-μm elliptical cross section,[4] oriented so that their intersections with the planes of the LEH's are approximately circular. The size of the cross section is determined from plasma physics considerations: i.e., smaller spots, while preferable for fitting through the LEH's, result in laser intensities (especially near the LEH's) that may be too high from the point of view of plasma instabilities. For OMEGA, phase plates are not assumed, but the beams are assumed to be focused through vacuum just outside the hohlraums, as is currently done on Nova. (The standard direct-drive phase plates on OMEGA have best-focus spot sizes of ~0.8 mm— too large for indirect drive.)

The code is written to follow each ray through multiple reflections within the hohlraum, depositing some fraction $A(\theta_i)$

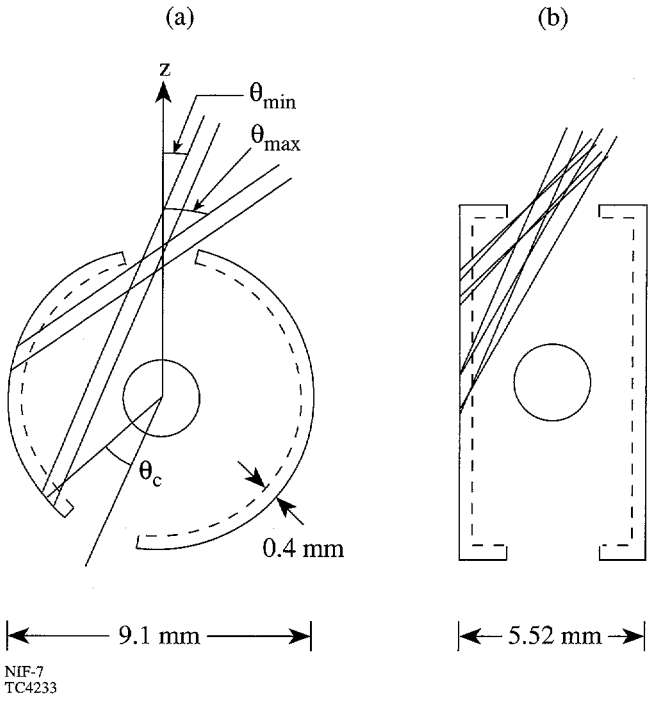

Figure 68.10
Representative beam paths into (a) tetrahedral and (b) cylindrical hohlraums, with dimensions appropriate to the NIF. In tetrahedral hohlraums the laser spots are spread fairly uniformly on the hohlraum wall, while in cylindrical hohlraums they lie on a small number of discrete rings. To account in a simple way for wall motion, the solid and dashed lines indicate the initial and final wall locations. For the tetrahedral hohlraums, the beams incident with θ_{min} and θ_{max} are drawn to illustrate clearance issues. One of these beams is drawn with a clearance angle θ_c from an opposing LEH. For an LEH angle $\theta_{LEH} = 55°$, $\theta_{min} = 23.0°$, $\theta_{max} = 54.8°$, and the smallest $\theta_c = 23.7°$.

each time where θ_i is the angle of incidence. The code can also impose a random scattering on the reflected rays, e.g., with a deflection cone having a specified shape and angular width. The code can be used to investigate glint—the early-time reflection of laser light from the hohlraum wall to the capsule. However, for the work presented here, the simple assumption is made that $A(\theta) = 1$. This should be a very good approximation for the large hohlraums of current interest, and especially for NIF hohlraums. For hohlraums on Nova, the absorption has been measured to be in excess of 90%.[18] The main physical process not modeled here is distributed absorption along the ray path. This is especially important for hohlraums that are initially empty (i.e., not gas filled), in which the light can be absorbed at low densities in the ablating gold plasma whose expansion is unimpeded.

After all of the rays have been traced, *BUTTERCUP* calculates a background radiation temperature T_r that is spatially independent. The radiation field within the hohlraum is then treated as a Planckian distribution at this temperature. Experimentally, this is a rather good approximation.[19] The temperature T_r at a given time is calculated using a simple, global energy balance between the power entering the radiation field from the laser source and the power lost from the radiation field, there being insignificant energy stored in the radiation field:

$$P_{\text{las}}(1-\beta_l) = \sigma T_r^{\,4}\left(\beta_c A_c + NA_h + \beta_w\ A_w\right), \qquad (1)$$

where P_{las} is the total laser power absorbed by the case, β_l is the fraction of this power that is not converted to x rays, σ is Planck's constant, and the term $(\beta_c A_c + NA_h + \beta_w A_w)$ may be thought of as the effective area of the hohlraum. The quantities A_c, A_h, and A_w are the areas of the capsule, an LEH, and the wall, respectively, in a hohlraum with N holes. The quantity β_w is defined as $1-\alpha_w$, where α_w is the wall albedo defined as the fraction of the x-ray energy incident on the hohlraum wall that is reradiated into the hohlraum; β_c $(=1-\alpha_c$, where α_c is the capsule albedo) is similarly defined. The wall albedo α_w increases with time and, at the peak of the laser pulse, is typically 0.8 for Nova or OMEGA and 0.9 for the NIF. The capsule albedo α_c is taken here to be small (0.1); reemission from the capsule is in any case a minor factor in Eq. (1). The x-ray conversion efficiency, $1-\beta_l$, depends on the irradiation conditions[1] and is taken to be 0.7 here.

Given the background temperature T_r, the emission intensity I_e (power per unit area) at any point on the interior of the case can be calculated from local energy balance. Incoming fluxes comprise radiation from the cavity $(\sigma T_r^{\,4})$ and the absorbed laser energy I_l. Subtracting the respective fractions β_w and β_l that are not re-radiated, one finds I_e:

$$I_e = (1-\beta_w)\,\sigma\, T_r^{\,4} + (1-\beta_l)\,I_l\,. \qquad (2)$$

One can then define an effective radiation temperature T_e by equating I_e to $\sigma T_e^{\,4}$, and, more important from the point of view of the code, the brightness (power per unit area per unit solid angle) $B = I_e/\pi$ at all points on the hohlraum wall.

At present, the code assumes that the albedos are spatially independent. This is not an intrinsic limitation since *BUTTERCUP* could easily be linked to some model giving the spatially dependent albedos through Eqs. (1) and (2). Another assumption implicit in the code is that the x-ray conversion efficiency is independent of the angle of incidence of the laser beams. Greater accuracy here would require a self-consistent hydrodynamic calculation.

Given the brightness distribution B on the wall, *BUTTERCUP* then scans over a number of points on the capsule and, for each point (θ, ϕ), determines the incoming irradiation intensity $I(\theta, \phi)$ by integrating the brightness over all angles (see Fig. 68.11). *BUTTERCUP* makes use of the fundamental result that, for radiation transport in vacuum, the spectral brightness is constant along a ray;[20] it thus suffices to follow each ray from the capsule, with spherical coordinates (θ', ϕ') relative to the capsule normal, to its intersection point on the wall and look up the brightness there. The incoming intensity is then given by

$$I(\theta,\phi) = \iint B(\theta',\phi')\,\cos\theta'\sin\theta'\,d\theta'\,d\phi'\,. \qquad (3)$$

The $\cos\theta'$ factor accounts for the angle between a surface element of the capsule and the incoming ray, and the $\sin\theta'$ factor for the solid angle. The code does not split each of the outer and inner surfaces into segments for which cross-coupling coefficients are calculated, as is generally done in view-factor codes.[14] Thus, while *BUTTERCUP* is known loosely as a view-factor code, "direct integration" would be a better description of its algorithm. The difference between the two approaches is minor; both approaches should give the same answers within the limits of numerical resolution.

Examples of *BUTTERCUP* predictions are given in Fig. 68.12 for tetrahedral hohlraums on OMEGA and the NIF. One-dimensional lineouts of the intensity on the capsule are shown as functions of azimuthal angle ϕ for various values of

θ, as are lineouts along θ for various values of ϕ. The symmetries shown in Fig. 68.9 are easily seen in the azimuthal scans. In Fig. 68.12(a) the scans at $\theta = 45°$ and 135° reflect the two-fold symmetry of the NIF, while the scan around the equator ($\theta = 90°$) shows a four-fold symmetry. For the OMEGA geometry, the expected three-fold symmetry is seen. In all cases the intensity minima correspond to points on the capsule facing an LEH.

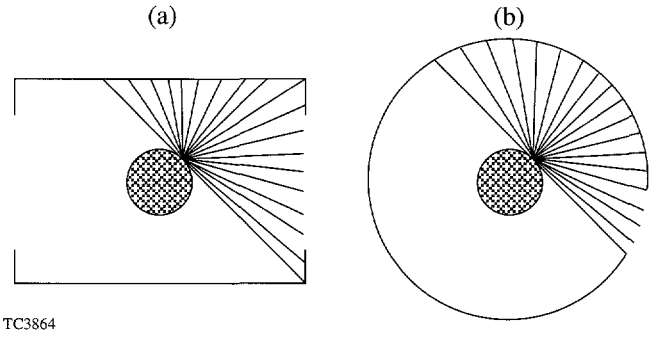

Figure 68.11
Schematic of the algorithm used by the view-factor code *BUTTERCUP*. The radiation flux incident at each point on the capsule is determined by integrating the brightness $B = \sigma T_e^4/\pi$ of the wall over a hemispherical solid angle. The algorithm is essentially independent of whether the hohlraum is (a) cylindrical or (b) tetrahedral.

Tetrahedral Hohlraums on OMEGA

A comparison has been made between cylindrical and tetrahedral hohlraums on OMEGA, using the parameters listed in Table 68.II. The cylindrical hohlraums are standard Nova hohlraums, except that slightly smaller LEH's are used.

As in the preceding article, the cylindrical hohlraums are conveniently irradiated with the axis of the cylinder oriented to pass through the centers of opposing pentagons on the target chamber. This provides, for each LEH, two rings of five beams with angles of incidence 21.4° and 42.0°, and a ring of ten beams at 58.9°. Figure 68.13 shows a possible design with beams pointed onto three rings on the cylinder wall. This combination of beams can deliver 20 kJ of energy in a 1.0-ns pulse.

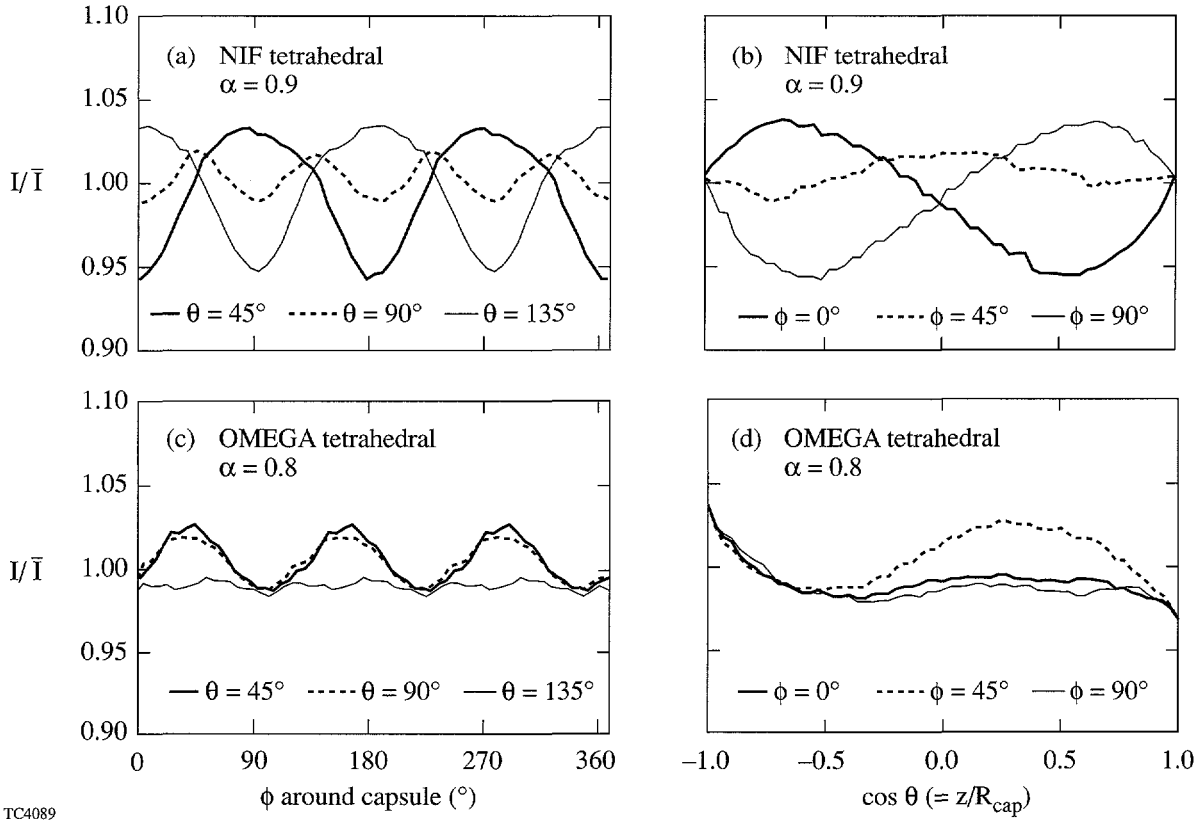

Figure 68.12
Representative results from *BUTTERCUP* calculations. The radiation intensity on the capsule is plotted against ϕ and $\cos\theta$ for NIF and OMEGA tetrahedral hohlraums. The different patterns correspond to the different orientations shown in Fig. 68.9. In all cases the minima occur at points facing the LEH's.

Table 68.II: Dimensions of cylindrical and tetrahedral hohlraums for the NIF and for OMEGA as used in this article. (In calculations where wall motion is included, these are the initial dimensions.)

		NIF		OMEGA	
		Cylindrical	Tetrahedral	Cylindrical	Tetrahedral
Case radius	R_c (mm)	2.76	4.55	0.8	1.4
Hole radius	R_h (mm)	1.38	1.14	0.5	0.4
Length	L (mm)	10.4	—	3.0	—
Capsule radius	R_{cap} (mm)	1.13	1.13	0.2	0.2
R_{cap}/R_c		0.41	0.25	0.25	0.14
Case area	A_c (mm^2)	216.2	243.8	17.53	22.62
Total hole area	A_h (mm^2)	11.96	16.33	1.57	2.01
A_h/A_c		0.055	0.067	0.09	0.09
Energy	(kJ)	1800	1650	20	30

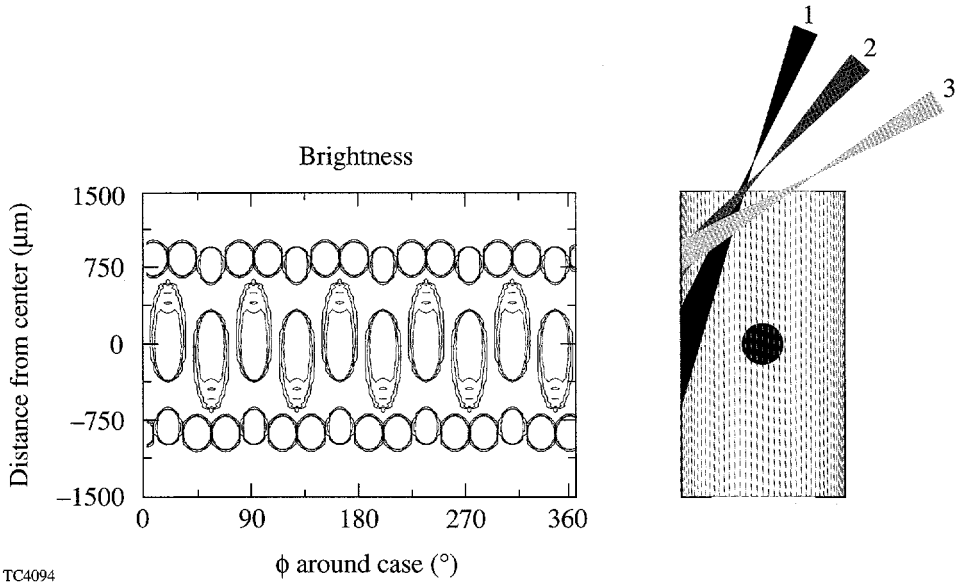

Figure 68.13
A possible irradiation geometry for cylindrical hohlraums on OMEGA (right) and corresponding contours of brightness B (left). A 40-beam subset of the 60 beams is used, comprising three different rings from each hemisphere of the target chamber. The inner and middle rings (1 and 2) possess five beams each, while the outer rings (3) have ten beams spaced in five pairs around the azimuth. The resulting pattern on the hohlraum wall comprises three bands, two with 15 beams each (as used in most of the experiments described in the preceding article) and one with ten beams.

With a tetrahedral hohlraum, however, all 60 beams can be used for a total of 30 kJ of laser energy. The four groups of 15 beams entering the four LEH's are equivalent to each other with respect to rotations within the tetrahedral group. Through each LEH there are two sets of six beams, with $\theta = 23.2°$ and 47.8°, respectively, and one set of three beams with $\theta = 58.8°$.

A sinusoidal map (Fig. 68.14) of the locations of all 60 OMEGA beams on the wall of a tetrahedral hohlraum shows generally uniform coverage of the wall. The beams clear the LEH's with minimum clearances of 50 μm upon entering the case and 150 μm on the inside of the case.

The dependence of the rms nonuniformity σ_{rms} on albedo is shown in Fig. 68.15 for both cylindrical and tetrahedral hohlraums on OMEGA. Low albedo corresponds to early times, while the maximum albedo corresponds to the peak of the pulse or later times. For each type of hohlraum, one curve applies to "full power," i.e., equal beam energies, and the other to a "tuned" case, i.e., with the energy in some beams being reduced. The tuning carried out here is time independent; thus, the beams have different energies but the same pulse shape. (By appropriate detuning of the frequency-conversion crystals, this can probably be accomplished quite accurately on OMEGA.) For both cylindrical and tetrahedral hohlraums the

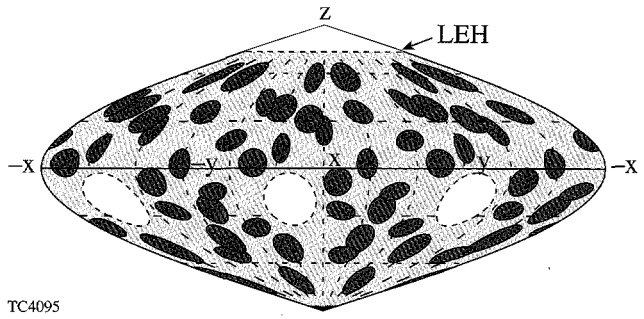

Figure 68.14
Sinusoidal map of the locations of all 60 OMEGA beam spots on the interior wall of a tetrahedral hohlraum. One LEH is centered on the z axis [as in Fig. 68.9(b)] and the others are shown as dashed circles. The exact tetrahedral symmetry of the OMEGA beam locations and the even distribution of beam spots on the hohlraum wall effectively eliminate all spherical harmonic modes other than those present in true tetrahedral geometry.

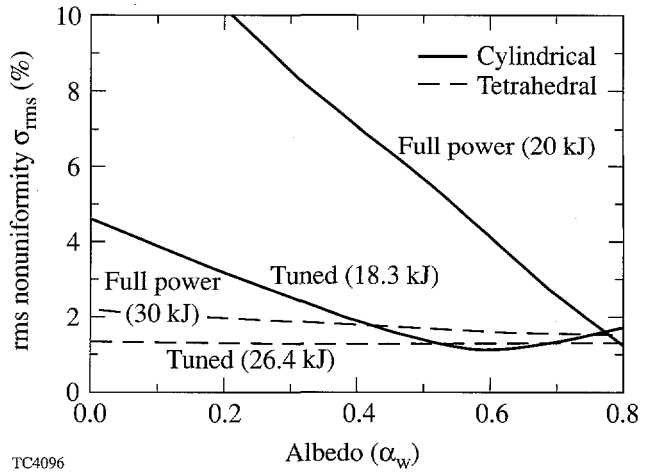

Figure 68.15
Nonuniformity σ_{rms} as a function of albedo for cylindrical and tetrahedral hohlraums on OMEGA, for equal beam energies ("full power") and for optimized relative beam energies ("tuned"). Each hohlraum is designed for optimum symmetry (at full power) at an albedo of 0.8. The cylindrical hohlraum is sensitive to large swings in the P_2 and P_4 Legendre modes and thus requires tuning, while the tetrahedral hohlraum is dramatically less sensitive to albedo. This is due to the uniform coverage of the hohlraum wall seen in Fig. 68.14 (Note that time-dependent tuning, not considered here, is needed for cylindrical hohlraums for optimum performance.)

tuning was carried out to optimize the uniformity at or near the end of the laser pulse, where the albedo is approximately 0.8. Tuning the tetrahedral hohlraum was accomplished by noting that the symmetry of the system results in five groups of beams and adjusting the five available independent parameters.

Figure 68.15 shows a strong dependence of σ_{rms} on albedo (and thus time) in the case of the cylindrical hohlraum. While the tuned case performs significantly better, the time-dependent nonuniformity (dominated by the P_2 mode) is still evident. In contrast, the insensitivity to albedo for the tetrahedral hohlraum is striking. The reason is clear from Fig. 68.14—the laser spots are distributed so uniformly around the case that the contribution to the capsule uniformity due to the direct laser source shares the same intrinsic spatial distribution as the background radiation source. Thus, as the increasing albedo changes the proportions of these two sources, the net effect seen by the capsule is essentially zero. Using the same argument, it is probable that this picture will be unaffected by other effects such as wall motion, beam steering, and laser-beam refraction. It is hard to conceive of any processes that can systematically upset the uniform distribution of laser spots on the hohlraum wall.

The tuned tetrahedral curve exhibits some further improvement. This is achieved by increasing the relative weighting of beams near the LEH's, which results in a greater effect at early times. The tuned tetrahedral hohlraum achieves a total rms nonuniformity of 1.5% or less throughout the whole range of albedos. The slightly better performance of the OMEGA tetrahedral hohlraum in comparison with that of the NIF (see below) is due in part to the absence on OMEGA of the Y_{20} spherical-harmonic component.

Tetrahedral Hohlraums on the NIF

Similar calculations have been performed for tetrahedral hohlraums on the NIF. The hohlraum dimensions are listed in Table 68.II. (The dimensions for cylindrical hohlraums are given for comparison, although results for cylindrical hohlraums are not given in this article.)

Figure 68.16(a) shows a sinusoidal plot of the NIF port locations for the most recent design. The ring of 12 beams at $\theta_5 = 77.45°$ is provided to accommodate direct drive. The azimuthal angles between each of rings 1 through 4 and their reflections in the lower hemisphere are chosen so that beam dumps are located a quarter of a port spacing from the ports in the opposing rings. The relative azimuthal angle between rings 1 and 3 is chosen over other possibilities to give the configuration best suited to tetrahedral hohlraums. Specifically, the ϕ's of the first beam port in each of the ten rings, from top to bottom, are 78.75°, 33.75°, 16.875°, 39.375°, 24.375°, 5.625°, 5.625°, 28.125°, 56.25°, and 11.25°.

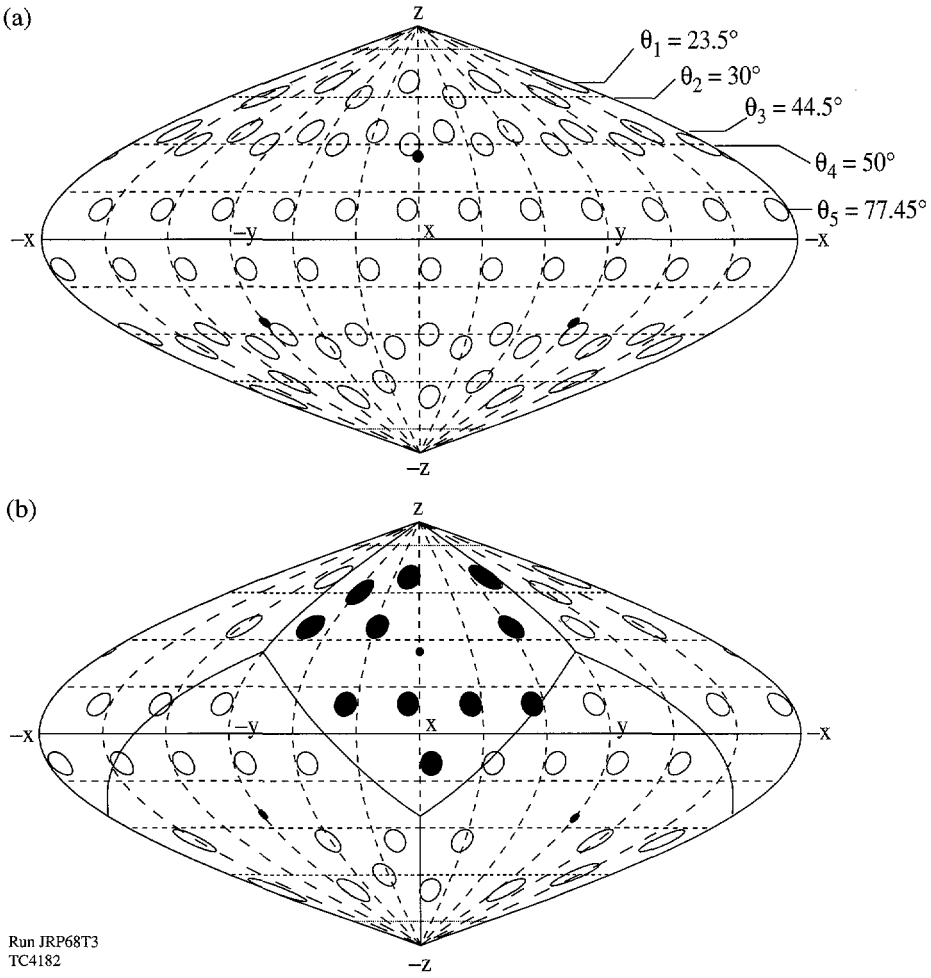

Figure 68.16
(a) Sinusoidal map of the proposed port locations on the NIF target chamber. Cylindrical hohlraums are irradiated with rings 1 through 4, and direct-drive targets with rings 1, 3, and 5. The small solid circles indicate LEH placements with $\theta_{LEH} = 55°$. The subset used for tetrahedral hohlraums is shown in (b), which also divides the surface of the sphere into the four regions closest to each LEH.

Figure 68.16(b) illustrates the surface of the sphere divided into the four sectors corresponding to tetrahedral symmetry. The LEH's are placed at the vertices of a true tetrahedron (i.e., $\theta_{LEH} = 55°$). It is possible to use 11 out of the 12 available beams. It may be noted that one beam from the lower hemisphere is pointed into the LEH shown in the upper hemisphere. Each beam is directed into the closest LEH.

BUTTERCUP calculations for a representative design were carried out for three separate hohlraum radii: 4.55 to 4.15 mm, allowing for 0.4 mm of wall motion during the laser pulse (see Fig. 68.17). This is consistent with a 1-D *LASNEX* calculation.[21] From the *LASNEX* calculation it was also possible to estimate the time and incident laser power corresponding to each value of albedo. These are indicated in Fig. 68.17, where the appropriate portions of the three curves are shown solid.

The rms nonuniformity σ_{rms} is close to 2% for all values of albedo. In this calculation time-independent tuning was used (as in Fig. 68.15 for OMEGA). This resulted in an energy into the hohlraum of 1.3 MJ [out of the available untuned energy of 1.65 MJ (11/12 × 1.8 MJ)]. However, with time-dependent tuning, significantly more than 1.3 MJ can be used because the tuning is only needed at early time (low albedo). Thus, if the hohlraum were tuned in a time-dependent way, i.e., during the rising part of the laser pulse but not during the final, maximum-power portion, close to 1.65 MJ would be delivered to the hohlraum and σ_{rms} would stay within 2% throughout the pulse.

The incidence angles of the 11 beams through the LEH are 23.0°, 23.7°, 31.5°, 32.2°, 39.2°, 43.6°, 47.2°, 47.8°, 53.8°, 53.9°, and 54.9°. Beam paths with the minimum and maximum angles are shown in Fig. 68.10. Some design flexibility is available by making minor adjustments to the (θ,ϕ) coordinates of the LEH and by not pointing some beams through the center of the LEH. However, experiments aimed at exploring clearance and symmetry issues in tetrahedral hohlraums are needed before such detailed design issues are addressed.

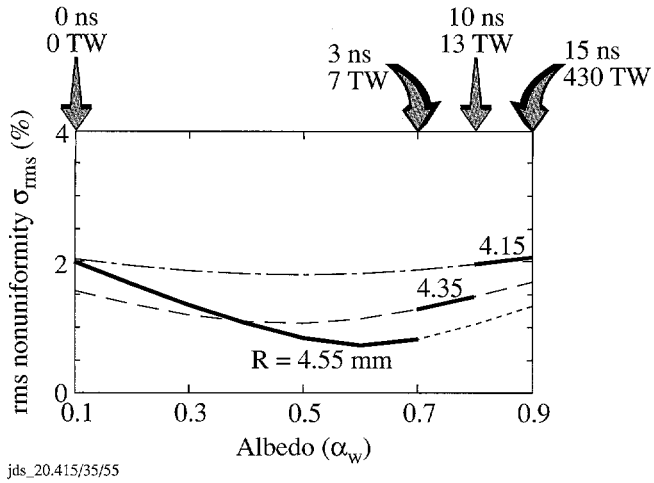

Figure 68.17
Nonuniformity σ_{rms} as a function of albedo for a NIF tetrahedral hohlraum. Wall motion is treated by assuming that the hohlraum radius reduces from 4.55 mm to 4.15 mm during the 15-ns laser pulse. The mapping shown between time (and power) in the laser pulse and albedo is obtained from a *LASNEX* calculation. The solid portions of the curves indicate the appropriate radius to use for σ_{rms} at a given time, based on the same *LASNEX* calculation.

Summary

A view-factor code has been developed to carry out a comparative study of indirect-drive uniformity in cylindrical and tetrahedral hohlraums. This code does not include hydrodynamics and radiation physics, but it has the merit of being fully 3-D. It has been used to model both types of hohlraum, for both the NIF and OMEGA laser systems.

The results for cylindrical hohlraums are in accord with what has been well established, namely that the P_2 nonuniformity is the dominant nonuniformity and must be compensated through varying the relative powers of the different laser beams as a function of time, a process known as beam phasing. Tetrahedral hohlraums, on the other hand, display a significantly reduced sensitivity to the changing wall albedo and may not require beam phasing at all if an rms nonuniformity around the capsule of 2% or less at all times is acceptable.

Examination of the NIF geometry has shown that, by appropriately using the extra beam ports proposed for direct drive, it is also possible to irradiate tetrahedral hohlraums on the NIF. Instead of diverting 24 of the 48 beams to the equatorial region of the target chamber, as for direct drive, one diverts 20 beams, all 8 beams from each of the rings at 50° and 2 beams from each of the rings at 30°, to the equator. On-capsule uniformity of ~2% throughout the pulse can be obtained. The main uncertainty appears to relate to issues of clearance through the LEH's; this is a greater problem than for cylindrical hohlraums because some laser beams intersect the hohlraum wall close to the LEH's. Clearance of the capsule plasma is not significantly different in the two cases. While tuning may not be necessary for a tetrahedral hohlraum, appropriate tuning (which could be time independent on OMEGA and time dependent on the NIF) can enhance the uniformity with a minimal energy penalty.

Tetrahedral hohlraums have an intrinsically better uniformity than cylindrical hohlraums, but suffer the disadvantages of being fully 3-D, harder to model, and harder to diagnose experimentally. However, with advances in modeling and diagnostic capabilities, these disadvantages may become minor. At the very least, tetrahedral hohlraums merit consideration as an alternative route to indirect-drive ignition and gain on the NIF. The OMEGA laser is ideally suited to carry out proof-of-principle experiments on tetrahedral hohlraums. The first such experiments are being planned in collaboration with the Los Alamos National Laboratory and the Lawrence Livermore National Laboratory.

More details on the work reported in this article can be found in Ref. 22.

ACKNOWLEDGMENT

The authors are pleased to acknowledge many detailed discussions with Dr. S. M. Pollaine over an extended period of time. The interest of Dr. D. Eimerl and Dr. M. D. Rosen has also been greatly appreciated. This work was supported by the U.S. Department of Energy Office of Inertial Confinement Fusion under Cooperative Agreement No. DE-FC03-92SF19460, the University of Rochester, the New York State Energy Research and Development Authority, and by the Laboratory for Laser Energetics Summer High-School Research Program, supported by National Science Foundation Contract No. ESI9256079.

REFERENCES

(a) Also J. C. Wilson Magnet High School, Rochester, NY 14611. Current address: Harvard University, Cambridge, MA 02138.

1. J. Lindl, Phys. Plasmas **2**, 3933 (1995).
2. A. A. Hauer *et al.*, Phys. Plasmas **2**, 2488 (1995).
3. L. J. Suter *et al.*, Phys. Rev. Lett. **73**, 2328 (1994).
4. S. W. Haan *et al.*, Phys. Plasmas **2**, 2480 (1995).
5. S. E. Bodner, Comments Plasma Phys. Control. Fusion **16**, 351 (1995).
6. N. D. Delamater *et al.*, Phys. Plasmas **3**, 2022 (1996).
7. D. W. Phillion and S. M. Pollaine, Phys. Plasmas **1**, 2963 (1994).

8. H. Azechi *et al.*, Jpn. J. Appl. Phys. **20**, L477 (1981).

9. C. Yamanaka *et al.*, in *Plasma Physics and Controlled Nuclear Fusion Research 1984* (IAEA, Vienna, 1985), Vol. 3, p. 3.

10. Y. Kato *et al.*, in *Plasma Physics and Controlled Nuclear Fusion Research 1990* (IAEA, Vienna, 1991), Vol. 3, p. 89.

11. T. Mochizuki, S. Sakabe, and C. Yamanaka, Jpn. J. Appl. Phys. **22**, L124 (1983).

12. M. Murakami and K. Nishihara, Jpn. J. Appl. Phys. **25**, 242 (1986).

13. D. C. Wilson *et al.*, Bull. Am. Phys. Soc. **35**, 2021 (1990).

14. M. Murakami and J. Meyer-ter-Vehn, Nucl. Fusion **31**, 1333 (1991).

15. M. Murakami and J. Meyer-ter-Vehn, Nucl. Fusion **31**, 1315 (1991).

16. G. D. Tsakiris, Phys. Fluids B **4**, 992 (1992).

17. M. Murakami, Nucl. Fusion **32**, 1715 (1992).

18. R. L. Kauffman *et al.*, Phys. Rev. Lett. **73**, 2320 (1994).

19. M. D. Cable *et al.*, Phys. Rev. Lett. **73**, 2316 (1994).

20. Ya. B. Zel'dovich and Yu. P. Raizer, in *Physics of Shock Waves and High-Temperature Hydrodynamic Phenomena,* edited by W. D. Hayes and R. F. Probstein (Academic Press, New York, 1966), Vol. I, p. 131.

21. S. M. Pollaine, private communication (1996).

22. J. D. Schnittman and R. S. Craxton, Phys. Plasmas **3**, 3786 (1996).

Properties of the Speckle of Focused, Phase-Converted Laser Beams and the Reduction of Time-Averaged Irradiation Nonuniformity in Laser-Driven Plasmas due to Target Ablation

Highly uniform irradiation and energy absorption at the surface of fuel-filled capsules are among the most important requirements for successful inertial confinement fusion (ICF) implosions.[1,2] In most laser-plasma experiments of interest to ICF, laser beams are phase converted by being passed through distributed phase plates (DPP's).[3] DPP's greatly improve the uniformity of focused beams by reducing large-scale beam structure, leaving intensity profiles with well-controlled, reproducible envelopes modulated by fine speckle.[3,4] However, the nonuniformity remaining in the speckle is still more than the maximum allowable nonuniformity for ICF. This article presents an analytical model of this speckle and uses this model to show how a uniformly ablating plasma atmosphere acts to reduce the contribution of the speckle to the effective, time-averaged irradiation nonuniformity.

DPP's are transparent plates divided into a large number of flat area elements that are all identical, except that each of them adds a random phase delay to the transmitted light. This random distribution of phase delays effectively divides the beam into mutually spatially incoherent beamlets. When the beam is focused onto a surface, the irradiation pattern is a superposition of all the beamlets, where the envelope of the total intensity distribution is the same as the envelope of each individual beamlet. The shape and size of this envelope are determined by the shape and size of the individual phase-plate area element. The speckle in the intensity profile is the result of the mutual interference of the beamlets. The random spatial correlation among all beamlet phases results in a speckle modulation spectrum that is much flatter than would be obtained from a beam without DPP's, where the strong short-range spatial correlations in the beam phase profile result in correspondingly strong long-scale structure in the focused intensity pattern. DPP's with continuous phase distributions have been developed recently. They function with the same effect as discrete DPP's, except that their focused intensity profiles do not have the side lobes characteristic of the discrete area elements of discrete DPP's, and appreciably more of the laser energy can be focused onto a spherical target.[5]

This article shows that the effects of the speckle in the intensity distribution within a plasma average out in time due to a number of optical and hydrodynamic effects of uniform ablation that cause the irradiation-intensity distribution to move relative to the plasma. Any local effect of the irradiation speckle on the plasma that is cumulative, such as the conversion of laser intensity peaks into thermal energy peaks by absorption, will be reduced in proportion to this time averaging. The most direct measure of irradiation uniformity is that of the intensity distribution at a given surface, such as a surface fixed in space or a surface of constant electron density near where laser energy is absorbed. All effects that cause the irradiation-intensity distribution to move relative to this surface will contribute to a reduction in the effective irradiation nonuniformity by time averaging.

A number of laser-system modifications have been developed that cause the speckle to change rapidly in time so that their effects on the plasma will average out in time. These include induced spatial incoherence (ISI),[6] where the temporal coherence of the laser beam is disrupted, and smoothing by spectral dispersion (SSD),[7] where the laser is modulated electro-optically to expand the bandwidth of the laser. With both ISI[6,8] and SSD,[9,10] significant reduction in the effects of irradiation nonuniformity has been obtained, certainly more than the reduction that can be attributed to ablation-induced effects alone. Progress in developing these techniques has been driven in large part by the need to shorten their averaging times so that the cumulative effects of the irradiation nonuniformity can be averaged away very early in the pulse, before they can be imprinted irreversibly on the target.[10,11] Consequently, the possibility of additional speckle averaging at early times by all possible means remains an important question.

One source of averaging due to ablation is the continuous accumulation of ablated plasma in the beam path between the laser and the surface where the uniformity is measured. The dispersive effect of the ablated plasma reduces the total phase of light propagating through it between any two fixed points,

and the resulting refraction foreshortens the speckled interference pattern along the axial direction so that it appears to have receded from the target, back toward the laser. The continuous feeding of the atmosphere by ablation from the target results in a continuously increasing phase reduction and refraction, resulting in a steady recession of the intensity distribution past any surface fixed in the plasma at a point of constant electron density. The hydrodynamic motion of the plasma makes a comparably important contribution to the total motion of the intensity distribution relative to this surface. Both effects have been identified by Dewandre *et al.*[12] as sources of the frequency shift of light reflected from the atmosphere of an ablating target. These ablation-induced time-averaging effects are interesting not only because they are potentially beneficial, but also because they are unavoidable consequences of ablation that must be considered in interpreting any ICF experiment, past and future, where the quantitative effects of irradiation nonuniformity are a matter of concern.

For the purposes of this article, irradiation uniformity will be considered to be the uniformity of the intensity distribution at the absorption surface, which is defined simply as a surface of constant electron density, n_{abs}, where the absorption occurs. Absorption does occur over a finite distance, however, and some degree of additional smoothing of the effects of the irradiation nonuniformity can be expected since an appropriately weighted, instantaneous spatial average of the absorbed intensity distribution over this distance is a better measure of the true effective nonuniformity. Identifying this weighting would take this article beyond its intended subject of irradiation uniformity to the problem of relating the uniformity of ablative drive to the irradiation uniformity.

Thermal conduction and radiative transport in the atmosphere of an ablating target are other processes that smooth the nonuniformities in the thermal-energy distribution that are driven by nonuniform energy deposition.[1,13,14] These smoothing mechanisms can be effective only in the presence of a plasma atmosphere where there is a separation between the absorption region and the ablation region, where the pressure gradient driving the ablation is concentrated. Consequently, neither of these effects can smooth nonuniformities at the beginning of the laser pulse before an atmosphere has developed. It has been suggested that a suitable atmosphere could be formed by a flash of x rays applied before the laser pulse[15] or by coating the outside of the target with a thick outer layer of very light polymer foam.[16] A crucial advantage of ablation-induced time averaging of speckle over thermal smoothing and instantaneous axial averaging over an absorption interval is that it does not require that an atmosphere be present initially, only that one has begun to form.

This article first develops an analytical model for the intensity distribution and the spatial spectrum of the speckle pattern in the focal region for the case of random DPP's with discrete phase elements. The paraxial approximation is applied to the beam propagation in a uniform plane-parallel atmosphere. In this model, the reduction in the speckle spectrum due to averaging over an interval of time at a given absorption surface is equivalent to a spatial average over the corresponding interval of the propagation axis that represents the thickness of the portion of the intensity profile that would have passed through the absorption surface during the given time interval.

A simple idealized atmosphere model is used to obtain estimates of various contributions to this averaging interval. The plasma contribution is considered separately, and it is seen that the accumulation of typical ablation plasmas over typical hydrodynamic scale times can displace the speckle distribution over distances that are significant on the scale of the speckle structure. The total of the hydrodynamic and plasma effects is calculated in terms of a planar target accelerated by the expansion of an isothermal atmosphere. From this, it is seen that the plasma and hydrodynamic effects tend to cancel each other in a solid target during the beginning of the ablation, which is the crucial period when the atmosphere is most susceptible to a permanent imprint of the irradiation nonuniformity. The rates at which these averaging effects occur are calculated using 1-D hydrocode simulations of the ablation of a planar target for a range of irradiation intensities. These numerical results are well fit by the analytical approximations, which verifies that the analytical results are applicable. The averaging rates are the crucial final result because useful speckle averaging requires that the intensity nonuniformities must move through the plasma quickly enough to limit their cumulative, irreversible effects.

It is found that the averaging times in a solid CH target due to the plasma and hydrodynamic effects vary with the irradiation intensity and can be as little as a few hundred picoseconds for a beam of $f/7$ focal ratio, 0.351-μm wavelength, and 10^{15} W/cm^2 intensity. This smoothing time is short, compared with the hydrodynamic time scales of ICF implosions, but not short enough to avoid a permanent imprint of the irradiation nonuniformity on the plasma. While the plasma and hydrodynamic effects counteract each other early in the pulse, the hydrodynamic effect reverses at later times, as the target

accelerates, and the two effects add constructively, giving a much larger effect. Even then, the total averaging effect remains much slower than SSD and ISI smoothing times.

Many ICF experiments have already shown that ISI[6,8] and SSD[9,10] significantly reduce the effects of irradiation nonuniformity. The results of these experiments imply that any ablative smoothing effects that might have occurred in these experiments were dominated by SSD or ISI, but they do not rule out that ablative effects were important enough to have affected the quantitative comparisons between the results of measurements made with and without ISI or SSD. In the absence of SSD and ISI, it is likely that the ablative effects are an important smoothing mechanism, and they should be considered in interpreting experiments intended to determine the beneficial effects of these laser-system smoothing techniques. The main conclusion to be drawn from this work is that the formation of an ablated plasma atmosphere does act to reduce the effects of radiation nonuniformity and that understanding these effects is essential to a complete quantitative understanding of the effects of irradiation nonuniformity on these plasmas.

Beam Speckle Modulation Spectrum in the Focal Region

1. Derivation of the Beam Speckle Modulation Spectrum

The first task is to solve the electromagnetic wave equation

$$\left[\frac{\partial^2}{\partial t^2} - c^2\nabla^2 + \omega_p^2(z)\right]\mathbf{E}(\mathbf{x},t) = 0 \tag{1}$$

for a monochromatic beam of frequency ω focused onto a plane-parallel plasma target whose electron density $n_e(\mathbf{x}) = n_e(z)$ varies in the axial direction, the z direction, normal to the target surface. In what follows, the electron plasma frequency $\omega_p(z)$ will be expressed as

$$\omega_p^2(z) = \omega^2 \frac{n_e(z)}{n_c(\omega)}, \tag{2}$$

in terms of the critical electron density $n_c(\omega)$. Using the paraxial approximation, a solution to Eq. (1) can be obtained in terms of the reduced field quantity $\mathbf{U}(\mathbf{x})$, which represents the electrical field $\mathbf{E}(\mathbf{x})$ with the axial-wave phase removed,

$$\mathbf{E}(\mathbf{x},t) = \mathbf{U}(\mathbf{x})\exp\left[i\int_0^z k(z')dz' - i\omega t\right]. \tag{3}$$

The reduced field can be used to calculate the intensity of the irradiation,

$$I(\mathbf{x}) = |\mathbf{U}(\mathbf{x})|^2. \tag{4}$$

The wave vector of the axial wave $k(z)$ obeys the dispersion relation

$$c^2 k^2(z) = \omega^2 - \omega_p^2(z) \tag{5}$$

for a plane wave in an unmagnetized plasma. Note that the ω dependence of n_c and the z dependence of n_e and k will not always be written, but they are always understood to apply.

For the present purpose, the paraxial approximation is the assumption that nearly all the z dependence of $\mathbf{E}(\mathbf{x})$ is contained in the axial phase factor of Eq. (3), rather than in $\mathbf{U}(\mathbf{x})$, so that

$$\left|\frac{\partial^2 \mathbf{U}}{\partial z^2}\right| << k\left|\frac{\partial \mathbf{U}}{\partial z}\right|. \tag{6}$$

Using Eqs. (3), (5), and (6), the paraxial-wave equation,

$$\nabla_\perp^2 \mathbf{U} + 2ik\frac{\partial \mathbf{U}}{\partial z} + i\frac{\partial k}{\partial z}\mathbf{U} = 0, \tag{7a}$$

where

$$\nabla_\perp^2 = \frac{\partial^2}{\partial x^2} + \frac{\partial^2}{\partial y^2}, \tag{7b}$$

is obtained from the full-wave equation, Eq. (1).

The desired solution to Eqs. (7) is that of a beam of total power P, emerging through a planar aperture of area A oriented normal to the z axis. The beam is focused at the aperture with a device of focal length z_0 so that it converges all the way from the aperture plane, which intersects the z axis at the point $\mathbf{x} = (0,0,-z_0)$, to the focal point at the origin of the coordinates, $\mathbf{x} = 0$. This solution can be written in the form of an integral sum of converging waves,

$$U(\mathbf{x}) = \frac{k_v}{2\pi z_0}\sqrt{\frac{k_v}{k}\frac{P}{A}}\iint_A W(\mathbf{q}) \times \exp\left\{-i\left[\frac{k_v}{z_0}\mathbf{q}\cdot\mathbf{x} + \frac{k_v q^2 \zeta(z)}{2z_0^2} + \phi(\mathbf{q})\right]\right\} d^2q. \tag{8}$$

It is assumed that the field at the aperture is uniformly polarized. As a result, the field at the point $\mathbf{x}$ is identically polarized

everywhere, and polarization can be removed from the expression for the focused field, leaving Eq. (8) as a scalar expression. The vector variable $\mathbf{q}$ represents a point on the aperture. The vacuum wave number of a plane wave of frequency ω is $k_v = \omega/c$. The function $\zeta(z)$ is given by

$$\zeta(z) = \int_0^z \frac{k_v}{k(z')} dz' \tag{9}$$

and is the only z-dependent quantity in the phase of the solution. It is a measure of distance along the beam axis from the focal point that reduces to $\zeta(z) = z$ in a vacuum. In all expressions below, where the distance measure $\zeta(z)$ is written as ζ, its z dependence is understood. The boundary conditions of this solution are the function $W(\mathbf{q})$, the amplitude distribution in the aperture plane, which is real, positive, and normalized so that

$$\iint_A W^2(\mathbf{q}) d^2q = A, \tag{10}$$

and $\phi(\mathbf{q})$, which contains all the phase information in the beam at the aperture, including the intrinsic phase distribution of the beam plus the segmented phase profile added by the DPP.

The integral in Eq. (8) can be written as a sum of integrals over the N individual, identical, and identically oriented area elements that completely fill the aperture. Mathematically, this is a useful simplification because the phase $\phi(\mathbf{q})$ varies randomly and abruptly from element to element. Physically, this represents the beam as an array of beamlets of mutually spatially incoherent phase. The solution, written in this way, is

$$\begin{aligned} U(\mathbf{x}) = {} & \frac{k_v}{2\pi z_0}\sqrt{\frac{k_v}{k}\frac{P}{A}} \sum_{j=1}^{N} W(\mathbf{q}_j - \mathbf{q}_0) \\ & \times \exp\left\{-i\left[\frac{k_v}{z_0}\mathbf{q}_j \cdot \mathbf{x} + \frac{k_v q_j^2 \zeta}{2 z_0^2} + \phi(\mathbf{q}_j)\right]\right\} \\ & \times \iint_{a_j} \exp\left\{-i\left[\frac{k_v}{z_0}\xi \cdot \mathbf{x} \right.\right. \\ & \left.\left. + \frac{k_v \zeta}{z_0^2}\mathbf{q}_j \cdot \xi + \frac{k_v \xi^2 \zeta}{2 z_0^2}\right]\right\} d^2\xi , \end{aligned} \tag{11}$$

where each element is of area $a_j = a = A/N$. The substitution $\mathbf{q} = \mathbf{q}_j + \xi$ has been made, where the constant $\mathbf{q}_j$ denotes the center point of the jth DPP element. It is assumed that both $W(\mathbf{q})$ and $\phi(\mathbf{q})$ vary slowly enough within each DPP element to be approximated as the constants W_j and ϕ_j, respectively. Thus far no restriction has been placed on the distribution $W(\mathbf{q})$, other than that it must vanish for $\mathbf{q}_j$ large enough to cause Eq. (11) to violate the paraxial condition stated by Eq. (6). It is now assumed that $W(\mathbf{q}')$ describes a distribution centered at $\mathbf{q}' = 0$ so that Eq. (11), written as shown in terms of $W(\mathbf{q} - \mathbf{q}_0)$, represents a beam that originates from an illumination distribution on the aperture plane, centered off-axis at a point $\mathbf{q}_0$, and converges to a focal point on the z axis. This displacement $\mathbf{q}_0$ corresponds to an angle of incidence $\psi = \tan^{-1}(q_0/z_0)$, where $q_0 = |\mathbf{q}_0|$, or $\psi \cong q_0/z_0$ for small angles within the paraxial approximation, $q_0 << z_0$.

Equation (11) can be simplified by discarding negligible terms. What remains is

$$\begin{aligned} U(\mathbf{x}) = {} & \frac{k_v}{2\pi z_0}\sqrt{\frac{k_v}{k}\frac{P}{A}} \iint_a \exp\left\{-i\left[\frac{k_v}{z_0}\xi \cdot \mathbf{x}\right]\right\} d^2\xi \\ & \times \sum_{j=1}^{N} W_j \exp\left\{-i\left[\frac{k_v}{z_0}(\mathbf{q}_j + \mathbf{q}_0) \cdot \mathbf{x} \right.\right. \\ & \left.\left. + \frac{k_v (q_j^2 + 2\mathbf{q}_j \cdot \mathbf{q}_0 + q_0^2)\zeta}{2 z_0^2} + \phi_j\right]\right\}. \end{aligned} \tag{12}$$

The transform $\mathbf{q} \rightarrow \mathbf{q} + \mathbf{q}_0$ has been made from coordinates centered at the z axis to coordinates centered at the center of the beam on the aperture plane, so that the set of all $\mathbf{q}_j$ is centered about the origin $\mathbf{q} = 0$ and so that $\mathbf{q}_0$ represents the displacement of the entire beam from normal incidence.

The restriction of the paraxial approximation on Eqs. (8), (11), and (12), as stated by Eq. (6), requires that the focal convergence of the beam be slow and that the angle of incidence be small. This implies that the beam must not be followed into the plasma too close to what would be the turning point of any ray in a geometrical-optics ray-tracing treatment of the same problem. A clearer statement of a condition that is sufficient to satisfy Eq. (6) can be obtained using Eqs. (9) and (12). This is

$$\frac{k_v (q_j^2 + 2\mathbf{q}_j \cdot \mathbf{q}_0 + q_0^2)}{2 z_0^2} \frac{k_v}{k} << k \tag{13}$$

for all j. The meaning of this condition is made adequately clear by considering the case of a circular aperture of radius R, which gives

$$\frac{(R+q_0)^2}{2z_0^2} << \left(1-\frac{n_e}{n_c}\right), \tag{14a}$$

or, writing this in terms of the angle of incidence $\psi \cong q_0/z_0$ and the focal ratio or f-number of the beam $f = z_0/2R$,

$$\left(\frac{1}{2f}+\psi\right)^2 << 2\left(1-\frac{n_e}{n_c}\right). \tag{14b}$$

Equations (14) are essentially the same as the condition that no ray in the laser beam should approach its turning point. This turning point can be identified for each component of the plane-wave decomposition expressed in Eq. (12) as the point where the wave vector has become purely transverse. The transverse component $\mathbf{k}_\perp$ of the wave vector $\mathbf{k}$ of each component of the plane-wave decomposition of the reduced field can be identified in Eq. (12) as

$$\mathbf{k}_\perp = \frac{k_v}{z_0}(\mathbf{q}+\mathbf{q}_0). \tag{15}$$

As the beam propagates deeper into the plasma, $n_e(z)$ increases and k^2 decreases to the point where $\mathbf{k} = \mathbf{k}_\perp$, which defines the turning-point electron density n_{turn}. Combining Eqs. (2), (5), and (15), the turning-point density for the most obliquely incident ray is

$$\frac{n_{\text{turn}}}{n_c} = 1-\left(\frac{1}{2f}+\psi\right)^2 \tag{16}$$

for the case of a circular aperture. Even though the more normally incident rays penetrate further than this, it is clear that the paraxial approximation for the treatment of the whole beam has become invalid at $n_e = n_{\text{turn}}$. For the present purposes, either the condition $n_e < n_{\text{turn}}$ or Eqs. (14) can be taken as a validity condition. A more thorough validity study will not be undertaken here.

Equation (12) can be used in Eq. (4) to obtain the intensity, which can be written as the product

$$I(\mathbf{x}) = N\, I_0(\mathbf{x})\, G(\mathbf{x}), \tag{17}$$

where $I_0(\mathbf{x})$ is the intensity profile of a single beamlet,

$$I_0(\mathbf{x}) = \frac{(P/A)}{4\pi^2}\left(\frac{k_v}{k}\right)\left(\frac{k_v a}{z_0}\right)^2 \left|\frac{1}{a}\iint_a \exp\left\{-i\frac{k_v\,\xi\cdot\mathbf{x}}{z_0}\right\} d^2\xi\right|^2, \tag{18}$$

and where $G(\mathbf{x})$ is the speckle modulation factor

$$G(\mathbf{x}) = \frac{1}{N}\sum_{j=1}^{N} W_j^2 + \frac{1}{N}\sum_{j=1}^{N}\sum_{k\neq j}^{N} W_j W_k \exp\left\{-i\left[\Delta\phi_{jk} + \frac{k_v}{z_0}\Delta\mathbf{q}_{jk}\cdot\mathbf{x} + \frac{k_v\zeta}{z_0^2}\left(\overline{\mathbf{q}}_{jk}+\mathbf{q}_0\right)\cdot\Delta\mathbf{q}_{jk}\right]\right\}. \tag{19}$$

The factors in Eq. (18), the beam envelope expression, have been grouped so that they are all dimensionless, except for the intensity P/A.

The first term of the modulation factor given by Eq. (19) represents all the identical noninterfering pairs and is simplified by using the discrete-sum equivalent of Eq. (10),

$$\frac{1}{N}\sum_{j=1}^{N} W_j^2 = 1. \tag{20}$$

The second term in Eq. (19) is the sum of interference terms that represent the speckle modulation. For each element pair (j,k), there is a phase difference $\Delta\phi_{jk} = \phi_j - \phi_k$, a mean position $2\overline{\mathbf{q}}_{jk} = \mathbf{q}_j + \mathbf{q}_k$, and a separation $\Delta\mathbf{q}_{jk} = \mathbf{q}_j - \mathbf{q}_j$. Since the set of the positions of the DPP element centers $\{\mathbf{q}_j\}$ forms a regular lattice, a particular separation vector $\Delta\mathbf{q}_{jk}$ occurs repeatedly. Let N_p, then, be the number of distinct separation vectors, let $\Delta\mathbf{q}_m$ be a particular one among them, and let $N(\Delta\mathbf{q}_m)$, abbreviated by N_m when convenient, be the number of element pairs that have the separation $\Delta\mathbf{q}_m$. Any one of the N_m different pairs of points that share a particular $\Delta\mathbf{q}_m$ can be distinguished because they all have distinct $\overline{\mathbf{q}}_{jk}$, each of which can be denoted as $\overline{\mathbf{q}}_n$. The element pairs can now be identified by the indices (m,n), as well as (j,k), so each $\Delta\phi_{jk}$ can also be denoted as $\Delta\phi_{mn}$, and similarly, W_jW_k is a particular element (m,n) of the matrix formed by the outer product $\mathbf{W}\otimes\mathbf{W}$. From this point on, the analysis will assume uniform illumination of the beam aperture so that $W_j = 1$. The modulation function can

now be written as

$$G(\mathbf{x}) = 1 + \sum_{m=2}^{N_p} C(\Delta\mathbf{q}_m, \zeta) \exp\left[-i \frac{k_v}{z_0} \Delta\mathbf{q}_m \cdot \mathbf{x}\right], \quad (21a)$$

where

$$C(\Delta\mathbf{q}_m, \zeta) = \frac{1}{N} \sum_{n=1}^{N_m} \exp\left\{-i\left[\Delta\phi_{mn} + \frac{k_v \zeta}{z_0^2}(\bar{\mathbf{q}}_n + \mathbf{q}_0) \cdot \Delta\mathbf{q}_m\right]\right\}. \quad (21b)$$

From the set of all possible $\Delta\mathbf{q}_m$, $m = 1$ is chosen for $\Delta\mathbf{q} = 0$, which is excluded from the sum in Eq. (21a), since all $\Delta\mathbf{q} = 0$ pairs have already been summed to obtain the first term.

2. Evaluation of the Speckle Modulation Spectrum

Equation (21a) expresses the speckle modulation as a Fourier series whose coefficients, given by Eq. (21b), can also be expressed as a correlation sum

$$C(\Delta\mathbf{q}_m, \zeta) = \frac{1}{N} \sum_{n=1}^{N_m} f\left(\bar{\mathbf{q}}_n + \frac{1}{2}\Delta\mathbf{q}_m, \zeta\right) f^*\left(\bar{\mathbf{q}}_n - \frac{1}{2}\Delta\mathbf{q}_m, \zeta\right) \quad (22a)$$

of the function

$$f(\mathbf{q}, \zeta) = \exp\left\{-i\left[\frac{k_v |\mathbf{q} + \mathbf{q}_0|^2 \zeta}{2 z_0^2} + \phi(\mathbf{q})\right]\right\}. \quad (22b)$$

As was stated earlier, $\phi(\mathbf{q})$ is uniformly random over the interval $[0, 2\pi]$, from element to element on the DPP, or from term to term in the sum in Eq. (22a). In this section, the speckle modulation is being calculated at a single instant or at a fixed value of ζ, so the entire exponent in Eq. (22b) has the statistical properties of a uniformly random phase. Therefore, at any one target plane and at one particular spatial frequency $\mathbf{K}_m$, where

$$\mathbf{K}_m = \frac{k_v}{z_0} \Delta\mathbf{q}_m, \quad (23)$$

the contribution to the speckle modulation is given by a correlation sum of random phases, which gives

$$N^2 \left\langle \left| C(\Delta\mathbf{q}_m) \right|^2 \right\rangle = N_m. \quad (24)$$

This is obtained from Eqs. (22) by recognizing that the amplitude of a sum of terms of random phase accumulates as the quadrature sum of the amplitudes of the terms, just as the total distance in a random walk accumulates as the square root of the number of steps.[17] It should not be forgotten that Eq. (24) pertains to random-phase DPP's. The speckle modulation can be appreciably less than that suggested by Eq. (24) if the DPP is constructed with a nonrandom pattern whose spatial correlation function is less than random. If the phase imperfections of the laser beam are small enough, then irradiation uniformity can be improved simply by choosing the DPP pattern appropriately.[18]

According to the estimate stated in Eq. (24), the spectral density of the modulation pattern at a spatial frequency $\mathbf{K}_m$ is determined by N_m, the number of DPP element pairs within the aperture A that are separated by the vector $\Delta\mathbf{q}_m$. One method of counting all such pairs is illustrated by Fig. 68.18. Figure 68.18(a) shows an aperture A with center point O where one pair of area elements is represented by points J and K. Figure 68.18(b) shows this same aperture along with an exact duplicate A', which is obtained by moving every point in A by the displacement $\Delta\mathbf{q}_m$. For every point P in A, there is a point P' in A'. Note in particular that this displacement brings point K to K', which is congruent to J, and that this point is within $A \cap A'$, the intersection of A and A'. Similarly, any other pair of points within A with the same separation $\Delta\mathbf{q}_m$ corresponds, one-to-one, with a single point in $A \cap A'$. Therefore, the number of element pairs in A separated by the displacement $\Delta\mathbf{q}_m$ is the area of $A \cap A'$ divided by $a = A/N$, the area of a single element, or

$$N(\Delta\mathbf{q}_m) = \iint_{A \cap A'} \frac{d^2\bar{q}}{a}. \quad (25)$$

Equation (25) is an exact result. Writing the quantity $N(\Delta\mathbf{q}_m)$ as a function of $\Delta\mathbf{q}_m$ facilitates the transition from a function whose domain consists of a discrete set of vectors $\{\Delta\mathbf{q}_m\}$ to $N(\Delta\mathbf{q})$, a function of a continuous vector variable $\Delta\mathbf{q}$.

The result obtained from Eqs. (24) and (25) for a circular aperture of radius R is

$$\left\langle \left| C(\Delta q) \right|^2 \right\rangle = \frac{2}{\pi N}\left[\cos^{-1}\left(\frac{\Delta q}{2R}\right) - \left(\frac{\Delta q}{2R}\right)\sqrt{1 - \left(\frac{\Delta q}{2R}\right)^2}\right], \quad (26a)$$

where $\Delta q = |\Delta\mathbf{q}|$ and

$$\Delta q \le 2R. \quad (26b)$$

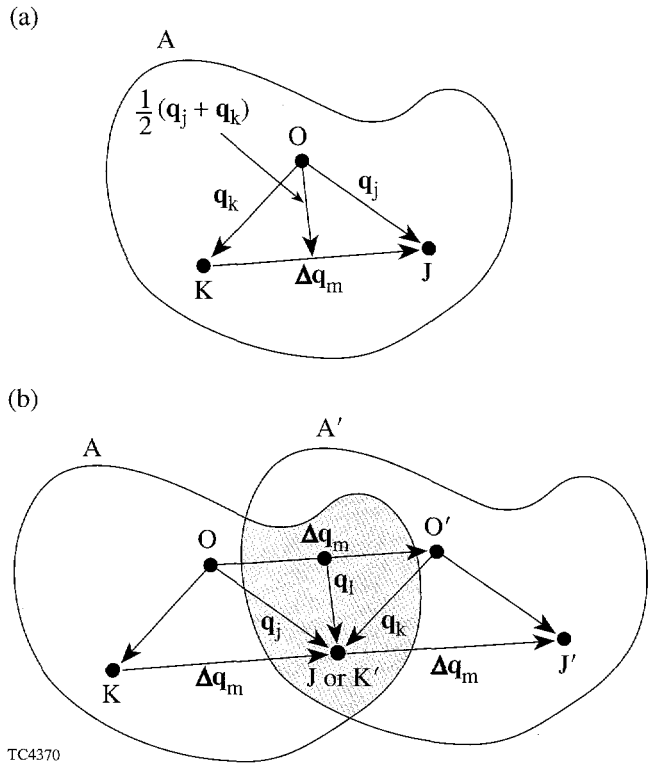

Figure 68.18
The spectral intensity of the speckle pattern at a spatial frequency $\mathbf{K}_m$ is determined by the number of DPP element pairs within an aperture A in the DPP plane that are separated by the vector $\Delta\mathbf{q}_m$. Counting these pairs is simplified by noting that each pair within an aperture A, points J and K as shown here, for example, corresponds, one-to-one, with a point L within the intersection of A and an identical aperture A' obtained from A by a displacement $\Delta\mathbf{q}_m$. This displacement brings any point P to P'. In particular, point J is congruent to point K', both of which are equivalent to the point L. The measure of the spectral intensity of the speckle at spatial frequency $\mathbf{K}_m$ is the area of the intersection of A and A'.

The symmetry of the circular aperture allows one to obtain the rms contribution of all speckle of the scalar spatial frequency corresponding to $\Delta q = |\Delta\mathbf{q}|$ with a simple integral over the direction θ,

$$\left\langle \left|C(\Delta q)\right|^2 \right\rangle = \int_0^{2\pi} \left\langle \left|C(\Delta\mathbf{q})\right|^2 \right\rangle \frac{\Delta q}{a^{1/2}}\, d\theta, \tag{27}$$

which gives

$$\left\langle \left|C(\Delta q)\right|^2 \right\rangle = \frac{8}{(\pi N)^{1/2}} \left(\frac{\Delta q}{2R}\right) \left[\cos^{-1}\left(\frac{\Delta q}{2R}\right) - \left(\frac{\Delta q}{2R}\right) \sqrt{1 - \left(\frac{\Delta q}{2R}\right)^2} \right]. \tag{28}$$

The argument $\Delta q/2R$ can be replaced by the equivalent expression

$$\frac{\Delta q}{2R} = \frac{K}{K_0}, \tag{29}$$

where the quantities not yet introduced are $K_0 = k_v/f$, the maximum spatial frequency present in the speckle modulation, and $f = z_0/2R$, the focal ratio or f number of the incident circular beam. The modulation spectrum from Eq. (28),

$$\left\langle \left|C(\Delta q)\right|^2 \right\rangle^{1/2},$$

is shown plotted in Fig. 68.19(a) as the "$\Delta\zeta/z_R = 0$" case. In this plot, the spectrum is normalized to give a peak value of unity, and the frequency variable is expressed in units of K_0 so that $\Delta q/2R = 1$ at full scale. This figure shows other results modified by axial averaging $(\Delta\zeta \neq 0)$, which will be explained in the following section. The speckle modulation results shown in Fig. 68.19 and in all subsequent figures are calculated for the case of the circular aperture.

The quantity $\left\langle \left|C(\Delta\mathbf{q})\right|^2 \right\rangle$ can be interpreted as the speckle power within an area $k_v{}^2\, a/z_0{}^2$ of the spatial frequency plane. This also represents the strength of the speckle modulation due to the interference between all DPP element pairs whose separations are given by all displacements within an area a centered about $\Delta\mathbf{q}$ on the $\mathbf{q}$ plane. The quantity $\left\langle \left|C(\Delta q)\right|^2 \right\rangle$, which has been integrated azimuthally, is to be interpreted as the speckle power within an interval $k_v\, a^{1/2}/z_0$ of spatial frequency $k_v\, \Delta q/z_0$. This is also the strength of the speckle modulation due to the interference between all DPP element pairs separated by all distances within a range $a^{1/2}$ of Δq.

Axial Averaging of the Speckle Spectrum

The time-averaged spatial distribution of the irradiation intensity at a surface within a plasma can be expressed as an axial average of the intensity distribution, as stated above. The results of the previous sections are now applied to the smoothing of speckle by axial averaging. The axial dependence of speckle modulation described by Eq. (21b) and ignored in the previous section is now considered. It will suffice for the present to consider simple uniform averaging over a range $\Delta\zeta$ of ζ,

$$\overline{C}(\Delta\mathbf{q}_m, \Delta\zeta) = \frac{1}{\Delta\zeta} \int_{-\Delta\zeta/2}^{\Delta\zeta/2} C(\Delta\mathbf{q}_m, \zeta)\, d\zeta. \tag{30}$$

This is appropriate if both the intensity and the plasma density are constant over this axial interval, such as when the time average is performed at a surface of constant electron density.

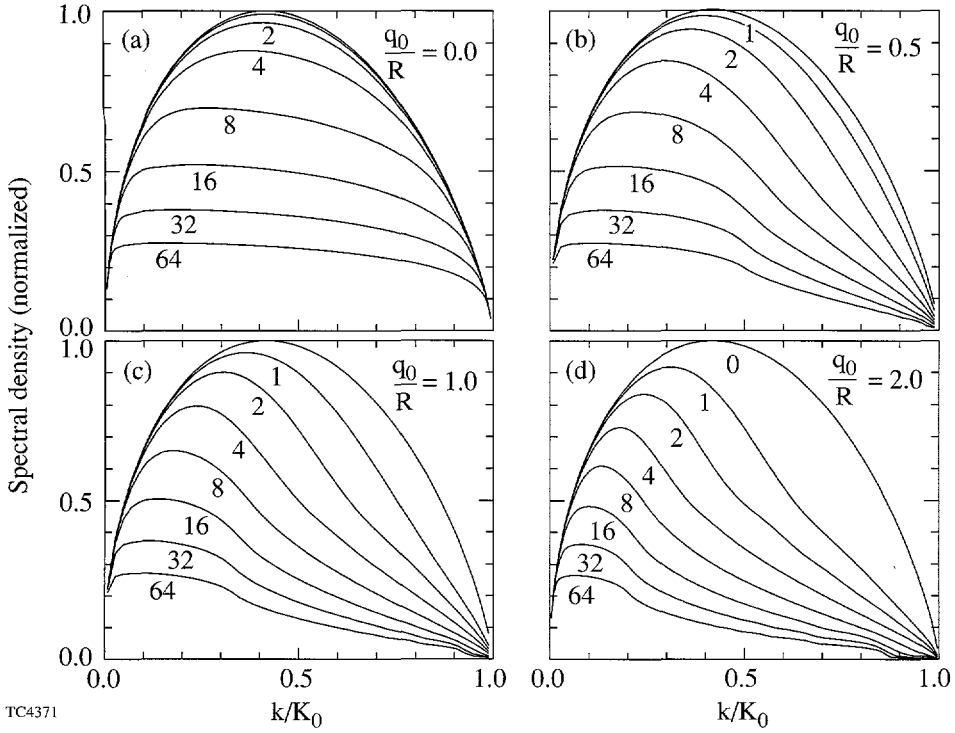

Figure 68.19
The spectral density of the speckle modulation factor, integrated over all directions of **K**, is plotted for various values of the smoothing distance, given in units of the Rayleigh range z_R. The spectral and frequency quantities are scaled to be plotted in units of their respective maximum values. Figure 68.19(a) shows results for normal incidence, $q_0/R = 0$. The unsmoothed spectrum is slightly asymmetric, and smoothing is only slightly more effective at higher frequencies. For the cases of non-normal incidence, $q_0/R = 0.5$, 1.0, and 2.0, plotted in (b), (c), and (d), respectively, the smoothing effect is much stronger overall, particularly at higher frequencies.

In the case of an observer remaining at a fixed position so that $\Delta z = 0$ and where the local electron density remains constant, an evolving plasma atmosphere causes the value of ζ at that fixed point to change in time, resulting in a time average that is equivalent to an average over an interval of ζ. This simple average can also serve as a first-order estimate of results for cases where the weighting is not severely skewed due to absorption, intensity variability, or plasma inhomogeneity.

Applying Eq. (21b) to Eq. (30), the average obtained is

$$\overline{C}(\mathbf{\Delta q}_m, \Delta\zeta) = \frac{1}{N}\sum_{n=1}^{N_m} \frac{\sin\left[\frac{k_v \Delta\zeta}{2z_0^2}(\overline{\mathbf{q}}_n + \mathbf{q}_0)\cdot\mathbf{\Delta q}_m\right]}{\frac{k_v \Delta\zeta}{2z_0^2}(\overline{\mathbf{q}}_n + \mathbf{q}_0)\cdot\mathbf{\Delta q}_m} e^{-i\Delta\phi_{mn}}. \quad (31)$$

The expectation value of this sum is

$$\left\langle \left|\overline{C}(\mathbf{\Delta q}_m, \Delta\zeta)\right|^2 \right\rangle = \frac{1}{N^2}\sum_{n=1}^{N_m} \frac{\sin^2\left[\frac{k_v \Delta\zeta}{2z_0^2}(\overline{\mathbf{q}}_n + \mathbf{q}_0)\cdot\mathbf{\Delta q}_m\right]}{\left[\frac{k_v \Delta\zeta}{2z_0^2}(\overline{\mathbf{q}}_n + \mathbf{q}_0)\cdot\mathbf{\Delta q}_m\right]^2}, \quad (32)$$

instead of Eq. (24). Just as Eq. (25) gives

$$\left\langle \left|C(\mathbf{\Delta q})\right|^2 \right\rangle = \frac{1}{N^2}\iint\limits_{A\cap A'} \frac{d^2\overline{q}}{a} \quad (33)$$

as the large-N limit of Eq. (24), one obtains

$$\left\langle \left|\overline{C}(\mathbf{\Delta q}, \Delta\zeta)\right|^2 \right\rangle = \frac{1}{N^2}\iint\limits_{A\cap A'} \frac{\sin^2\left[\frac{k_v \Delta\zeta}{2z_0^2}(\overline{\mathbf{q}} + \mathbf{q}_0)\cdot\mathbf{\Delta q}\right]}{\left[\frac{k_v \Delta\zeta}{2z_0^2}(\overline{\mathbf{q}} + \mathbf{q}_0)\cdot\mathbf{\Delta q}\right]^2} \frac{d^2\overline{q}}{a} \quad (34a)$$

as the large-N limit of Eq. (32) for $\Delta\zeta \neq 0$. The same expression can be written

$$\left\langle \left|\overline{C}(\mathbf{\Delta q}, \Delta\zeta)\right|^2 \right\rangle = \frac{1}{N^2}\iint\limits_{A\cap A'} \frac{\sin^2\left[2\frac{\Delta\zeta}{z_R}\frac{(\overline{\mathbf{q}} + \mathbf{q}_0)}{R}\cdot\frac{\mathbf{\Delta q}}{2R}\right]}{\left[2\frac{\Delta\zeta}{z_R}\frac{(\overline{\mathbf{q}} + \mathbf{q}_0)}{R}\cdot\frac{\mathbf{\Delta q}}{2R}\right]^2} \frac{d^2\overline{q}}{a} \quad (34b)$$

for the case of the circular aperture, where the variables $\bar{\mathbf{q}}$ and $\Delta\mathbf{q}$ have been scaled in terms of the aperture radius R and where $\Delta\zeta$ has been scaled in terms of the Rayleigh range,[19]

$$z_R = \frac{8f^2}{k_v}. \tag{35a}$$

This is the axial scale length of the intensity structure of a focused circular beam of focal ratio f and is the appropriate scale for measuring axial averaging distances. The magnitude of the oblique offset of the beam from normal incidence, $q_0 = |\mathbf{q}_0|$, is related to an angle of incidence ψ, where

$$\frac{q_0}{R} = 2f\tan\psi. \tag{36a}$$

For small angles, $q_0 << 2fR$, this gives

$$\psi \approx 4.09^\circ \frac{(q_0/R)}{(f/7)}, \tag{36b}$$

which shows that the sizable effects of oblique incidence expected with $q_0 \sim R$ are obtained with small angles of incidence.

Figure 68.19 shows several normalized speckle spectra,

$$\left\langle \left|\bar{C}(\Delta q, \Delta\zeta)\right|^2 \right\rangle^{1/2},$$

plotted as functions of spatial frequency K, written in units of $K_0 = k_v/f$, the maximum spatial frequency present in the speckle modulation. The quantities $\mathbf{K}$ and $\Delta\mathbf{q}$ are related by Eq. (23). These results have been obtained by evaluating Eq. (34b) numerically to obtain $\left\langle \left|\bar{C}(\Delta\mathbf{q}, \Delta\zeta)\right|^2 \right\rangle$, which is then averaged numerically over all directions of $\mathbf{K}$. Figure 68.19(a) shows results for normal incidence, $q_0/R = 0$. Each curve represents a different degree of axial averaging and is labeled by the smoothing interval $\Delta\zeta/z_R$, expressed in units of the Rayleigh range z_R. It is seen that values of $\Delta\zeta$ of the order of several z_R are needed for significant smoothing. The cases of nonnormal incidence, $q_0/R = 0.5$, 1.0, and 2.0, are plotted in Figs. 68.19(b), 68.19(c), and 68.19(d), respectively. These results show that the smoothing effect is enhanced significantly by only a slight tilt of the beam, particularly at higher spatial frequencies. According to Eqs. (36), the $q_0/R = 2.0$ case, for example, represents an angle of incidence of only 8.2° for a focal ratio of *f*/7.

Since higher transverse speckle frequencies correspond to stronger axial dependence, it would be expected that the smoothing for a given $\Delta\zeta$ would be strongest at higher speckle frequencies, but the $q_0/R = 0$ case plotted in Fig. 68.19(a) shows an averaging effect that is surprisingly symmetric about the middle speckle frequencies where it is strongest, in contrast to the highest and lowest frequencies where it is weakest. The least smoothing is expected at the lowest frequencies since this modulation is due to the interference of ray pairs that are closest in angle and thus produce interference structure with the weakest axial and transverse dependence. The high-frequency components, on the other hand, are dominated by interfering wave pairs that cross at the largest angles. This should lead to strong axial dependence, but the ray pairs with the largest crossing angles all originate from nearly opposite positions near the rim of the aperture at nearly opposite angles from the beam axis. In this limit, the interference patterns lack spatial dependence along the axis of the beam. Consequently, axial averaging has a vanishing effect at the highest speckle frequencies. Away from normal incidence, the symmetry axes of the beam and the plasma profile no longer coincide, and spatial averaging along the z axis does reduce the speckle modulation at the highest frequencies.

The spectral information plotted in Fig. 68.19 is recast in Fig. 68.20 as sets of curves, each representing the spatial frequency indicated by its label and each plotted as a function of the axial averaging distance. As in previous figures, the spatial frequency is written in units of the maximum frequency $K_0 = k_v/f$, and the averaging distance is expressed in units of the Rayleigh range z_R. The case of normal incidence is shown in Fig. 68.20(a), and the cases of nonnormal incidence, $q_0/R = 0.5$, 1.0, and 2.0, are shown in Figs. 68.20(b), 68.20(c), and 68.20(d), respectively. The $(\Delta\zeta)^{-1/2}$ scaling of the smoothing effect is seen clearly for large $\Delta\zeta/z_R$. Figure 68.20(e) summarizes these results with a set of curves, each representing the rms spectral average of the speckle modulation spectrum obtained for a given angle of incidence, plotted as functions of the averaging interval $\Delta\zeta/z_R$. Each curve is labeled by the assumed value of q_0/R.

The spectral information plotted in Fig. 68.19 is also recast in Fig. 68.21, where Figs. 68.21(a), 68.21(b), and 68.21(c) show sets of curves obtained for axial smoothing distances $\Delta\zeta/z_R$ = 2.0, 4.0, and 8.0, respectively, now plotted as functions of the incidence parameter of q_0/R. Each curve represents the spatial frequency indicated by its label, and each curve is plotted as a function of the angle of incidence, represented in the plot by the oblique offset q_0/R. As in

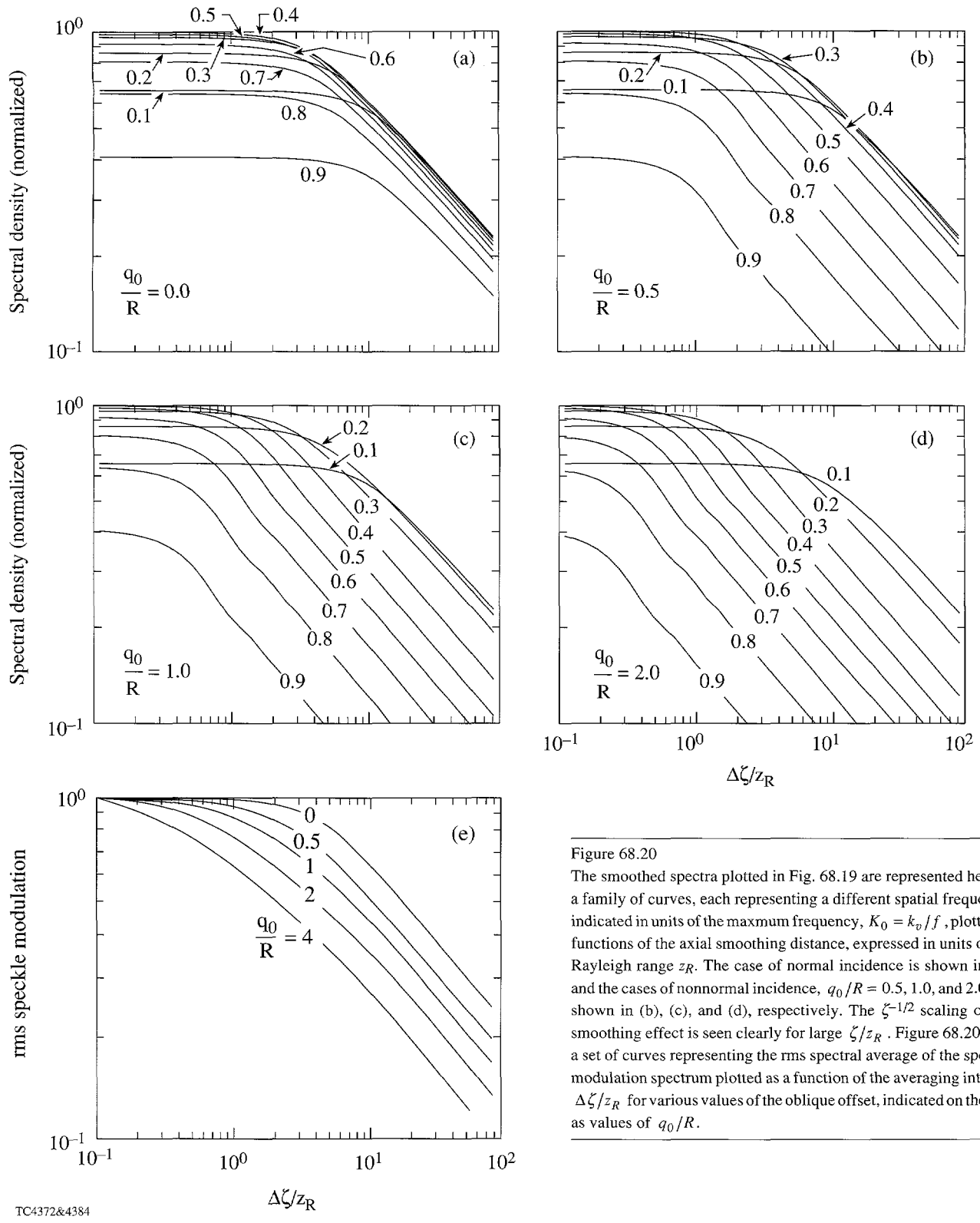

Figure 68.20
The smoothed spectra plotted in Fig. 68.19 are represented here as a family of curves, each representing a different spatial frequency, indicated in units of the maxmum frequency, $K_0 = k_v/f$, plotted as functions of the axial smoothing distance, expressed in units of the Rayleigh range z_R. The case of normal incidence is shown in (a), and the cases of nonnormal incidence, $q_0/R = 0.5$, 1.0, and 2.0, are shown in (b), (c), and (d), respectively. The $\zeta^{-1/2}$ scaling of the smoothing effect is seen clearly for large ζ/z_R. Figure 68.20(e) is a set of curves representing the rms spectral average of the speckle modulation spectrum plotted as a function of the averaging interval $\Delta\zeta/z_R$ for various values of the oblique offset, indicated on the plot as values of q_0/R.

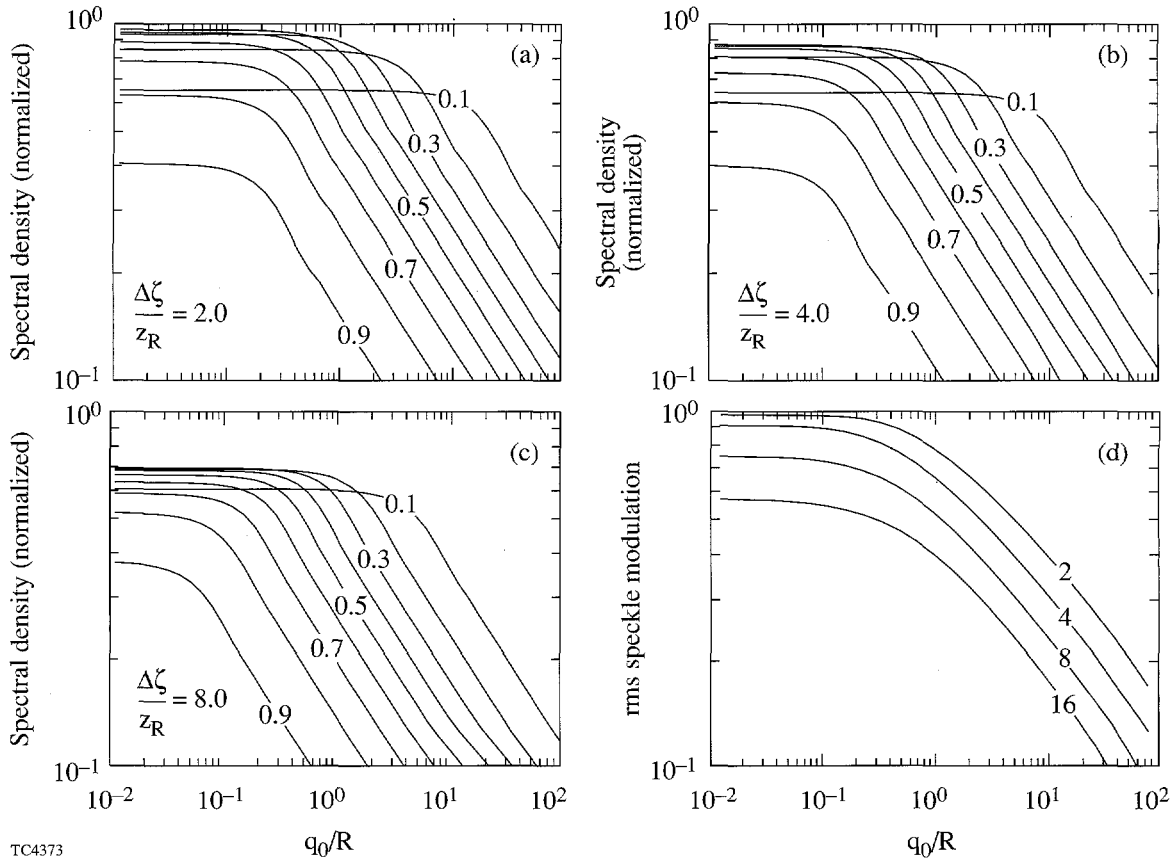

Figure 68.21
The smoothing of the spectra plotted in Fig. 68.19 is represented here as a family of curves, each representing a different spatial frequency indicated in units of the maximum frequency, $K_0 = k_v/f$, plotted as functions of the oblique offset, represented in units of q_0/R, for values of the axial smoothing distance $\Delta\zeta/z_R$ = 2.0, 4.0, and 8.0, in (a), (b), and (c), respectively. The curves are carried out to large values of q_0/R in order to show more clearly the $(q_0/R)^{-1/2}$ scaling of the smoothing effect, even though the paraxial approximation is violated for values of q_0/R that are not small compared to the focal ratio. Figure 68.21(d) is a set of curves representing the rms spectral average of the speckle modulation spectrum plotted as a function of oblique offset for various smoothing distances indicated on the plot as values of $\Delta\zeta/z_R$.

previous figures, the spatial frequency is written in units of the maximum frequency $K_0 = k_v/f$. The curves are carried out to large values of q_0/R for the sole purpose of highlighting the $(q_0/R)^{-1/2}$ scaling of the axial-averaging effect. It must be remembered that the paraxial approximation is valid only for values of q_0/R that are small compared to the focal ratio f. Figure 68.21(d) summarizes these results with a set of curves, each representing the rms spectral average of the speckle modulation spectrum obtained for a given axial-averaging interval, plotted as a function of the oblique offset q_0/R. Each curve is labeled by the assumed value of $\Delta\zeta/z_R$.

Figures 68.20(e) and 68.21(d) show what size axial-averaging interval $\Delta\zeta/z_R$ and oblique offset q_0/R are needed for a given reduction in the rms speckle modulation. For the purposes of this discussion, a factor of 2 will be taken as the nominal desired smoothing factor. At normal incidence, an axial-averaging interval of about 20.0 z_R is needed for this amount of smoothing. This is about one order of magnitude greater than expected, given that the Rayleigh range z_R is the characteristic length of the axial dependence of the speckle distribution. This surprising result is due to a surprising degree of axial independence in the speckle distribution along the beam axis. At only a modest angle of incidence, however, the same amount of smoothing is obtained with a much shorter axial-averaging interval. Oblique displacements of $q_0/R = 0.5$, 1.0, 2.0, and 4.0 reduce the axial-averaging interval to approximately $\Delta\zeta/z_R$ = 10.0, 7.0, 4.0, and 2.0, respectively. An

approximate scaling relationship for the oblique displacements and averaging intervals needed to obtain a smoothing reduction factor r can be inferred from the asymptotic behavior seen in Figs. 68.20 and 68.21 and from the above $\Delta\zeta/z_R$ and q_0/R values found to produce a speckle reduction factor of 0.5:

$$r^2 \approx 2.5\left(\frac{\mathbf{q}_0}{R}+0.5\right)^{-1}\left(\frac{\Delta\zeta}{z_R}\right)^{-1}. \tag{37a}$$

Since this expression has been fit to results that are not well into the scaling regimes of $\Delta\zeta/z_R$ and, in particular, q_0/R, this expression must be applied with caution as no more than a guide for the parameter ranges under consideration.

For the purposes of the discussion to follow, the range of $\Delta\zeta/z_R$ from 2 to 4 will be taken as a guide to what amount of axial averaging suffices for a significant amount of smoothing. This gives a factor-of-0.5 reduction in the rms speckle modulation for oblique displacements q_0/R in the approximate range from 4 to 2. As was mentioned above, this range corresponds to very modest angles of incidence, about 16° at most for *f*/7 irradiance. For multiple-beam experiments, angles of incidence of this order cannot be avoided. The absolute minimum oblique offset of $q_0/R = 1$ is obtained for the case of two beams whose focus lenses are touching. For a closely packed cluster of six beams in a hexagonal array, $q_0/R = 2$ is the absolute minimum. Allowing the beam edges to come no closer than one beam diameter doubles this to $q_0/R = 4$.

Thus far, all calculations and results have been expressed in terms of the oblique offset q_0/R and the Rayleigh range z_R because these are the parameters most characteristic of the speckle structure and the smoothing requirements. In describing an experimental configuration, the angle of incidence is more meaningful than q_0/R. The Rayleigh range given by Eq. (35a) written in terms of fundamental units is

$$z_R = 22\,\mu\text{m}\left(\frac{\lambda_v}{0.351\,\mu\text{m}}\right)\left(\frac{f}{7}\right)^2. \tag{35b}$$

The potential of an atmosphere for smoothing speckle is in large part a function of its scale length in units of z_R. One is reminded by Eq. (35b) that this figure of merit is a function of the laser wavelength λ_v and the focal ratio f. Equations (35b) and (36b) inserted into Eq. (37a) give

$$r^2 \approx 2.5\frac{\left(\frac{\lambda_v}{0.351\,\mu\text{m}}\right)\left(\frac{f}{7}\right)}{\left(\frac{\psi}{4.1^\circ}\right)\left(\frac{\Delta\zeta}{22\,\mu\text{m}}\right)} \tag{37b}$$

as an estimate of the speckle-reduction factor r expected from an angle of incidence ψ and an axial-averaging interval $\Delta\zeta$. This expression has been simplified by assuming that $q_0/R > 1.0$ is amply satisfied as if the speckle smoothing were in the $(q_0/R)^{-1/2}$ scaling regime, as seen in Fig. 68.21. An important conclusion to be drawn from Eq. (37b) is that the axial-averaging length $\Delta\zeta$ required to produce a given smoothing is proportional to the focal ratio f when the angle of incidence is within its scaling regime. This is a more-favorable focal-ratio scaling than is obtained near normal incidence when the smoothing is a function of $\Delta\zeta/z_R$ alone. In that case, Eqs. (35b) and (37a) show that the required $\Delta\zeta$ scales as the square of the focal ratio f for a specified value of r.

The smoothing of speckle by axial averaging and by SSD or ISI ought to have similar asymptotic time dependence since both work by the uniform averaging in time of the same random quantity. As long as $\Delta\zeta$ increases uniformly in time, the $\Delta\zeta^{-1/2}$ scaling of the axial smoothing factor corresponds to $(\Delta v\, t)^{-1/2}$, which is the reduction factor due to SSD and ISI at late times, where Δv is the bandwidth of the laser output.[20] These identical time dependences allow the axial-averaging reduction factor to be written in terms of an effective bandwidth as well. The effectiveness of smoothing by axial averaging can thus be readily compared with that of SSD and ISI by comparing bandwidths.

The next two sections consider circumstances under which laser ablation of a target can produce an adequate axial-averaging interval and how fast this averaging can occur.

The Plasma Effect

In this section the plasma effect alone is considered. The time average of the speckle is calculated at an absorption plane that is kept fixed in space, relative to the laser, while the plasma profile in the beam path changes in time. The magnitude of this effect is evaluated below for the case of an expanding plane-parallel atmosphere. The case of a spherically diverging plasma is also considered briefly because even in an experiment using a planar target, the plasma atmosphere does approach a spherically diverging profile beyond a distance comparable to the diameter of the illumination spot. This comparison of the plasma shift of the speckle for both a spherical and a plane-

parallel case clarifies this limitation of the plane-parallel assumption applied to the irradiation of a planar target. A more complete analysis of speckle averaging due to both the plasma and hydrodynamic effects is done in the following section entirely in terms of the plane-parallel, isothermally expanding atmosphere model.

An example of an expanding plane-parallel plasma profile is the exponential density profile that is obtained for the case of isothermal rarefaction,[6,21] which is considered in more detail in the **Discussion** section. For the simplest case of full, constant ionization, where the electron and mass densities are in a fixed ratio, the electron density can be written as

$$\frac{n_e(z)}{n_{\text{abs}}} = e^{-(z-z_{\text{abs}})/L}, \tag{38}$$

where n_{abs} is the electron density at the absorption surface, a constant-density surface fixed for now at $z = z_{\text{abs}}$. The laser enters the plasma from the $+z$ direction, and the scale length L grows in time as ablation fills the atmosphere with plasma. The on-target intensity uniformity is to be determined at the absorption surface. An expression for ζ_p, the plasma contribution to the axial distance parameter obtained from Eq. (9), is

$$\frac{\zeta_p(z_{\text{abs}})}{z_R} = \frac{k_v}{8f^2}\int_{z_{\text{abs}}}^{\infty}\left(\frac{1}{\sqrt{1-n_e/n_c}}-1\right)dz'. \tag{39}$$

Using Eq. (38), this gives

$$\frac{\zeta_p(z_{\text{abs}})}{z_R} = \frac{k_v L}{4f^2}\ln\left[\frac{2}{1+\left(1-n_{\text{abs}}/n_c\right)^{1/2}}\right], \tag{40}$$

which gives $\Delta\zeta_p$, the change in ζ_p due to the growth of the atmosphere by an increment ΔL,

$$\frac{\Delta\zeta_p}{z_R} = \frac{k_v \Delta L}{4f^2}\ln\left[\frac{2}{1+\left(1-n_{\text{abs}}/n_c\right)^{1/2}}\right]. \tag{41}$$

The quantity $\Delta\zeta_p$ is the averaging interval to be used to calculate the time averaging that occurs over the interval of time that the atmosphere grows by an increment ΔL.

The averaging effect described by Eq. (41) grows with increasing n_{abs}/n_c. The limit $n_{\text{abs}} \to n_c$ gives an indication of the maximum effect obtainable, although the restriction imposed on n_{abs}/n_c by Eqs. (14) must be applied case-by-case to ensure consistency with the paraxial approximation. Using parameter values typical of ICF, this limit is

$$\frac{\Delta\zeta_{p\max}}{z_R} = 6.33\frac{(\Delta L/100\,\mu\text{m})}{(\lambda_v/0.351\,\mu\text{m})(f/7)^2}, \tag{42a}$$

for the axial-averaging parameter applicable to the time interval during which the atmosphere expands by ΔL. In this idealized plasma model, a given increase in L is equivalent to an increase in the mass per unit area of the atmosphere exterior to the absorption surface. This mass per unit area is equivalent to a certain thickness of target material at its original density. For a solid CH polymer with a solid density of 1 g/cm^3, the averaging interval resulting from turning a thickness Δr_{CH} of target material into fully ionized atmospheric plasma is

$$\frac{\Delta\zeta_{p\max}}{z_R} = 4.72\frac{(\Delta r_{\text{CH}}/2\,\mu\text{m})}{(\lambda_v/0.351\,\mu\text{m})(f/7)^2}. \tag{42b}$$

This shows that an ICF plasma can shift the speckle intensity distribution by a significant amount, but that a substantial thickness of material, roughly the equivalent of a few microns of polymer, must be ablated. Even though an ICF plasma introduces enough phase dispersion and refraction to shift the speckle pattern by amounts needed for significant reduction by averaging, whether or not this provides a useful averaging rate depends on how fast the atmosphere grows and on whether or not a useful degree of averaging occurs before an irreversible imprint of the instantaneous nonuniformity has had time to develop. The likelihood of this being achieved in planar ablation experiments is the subject of the following section.

The most important consequence of spherical divergence is that the plasma effect is limited by the flow geometry. The plasma effect due to a planar atmosphere, on the other hand, is limited only by the supply of ablated plasma, or from the point of view of Eq. (40), ζ_p grows as long as L continues to grow. In the case of a finite illumination spot on a planar target, the atmosphere approaches spherical divergence with increasing distance from the target, and the upper limit on ζ_p depends on many things, including how quickly the transition from planar to spherical expansion occurs with increasing distance from the illumination spot, but a finite limit does exist. To show that spherical divergence results in a finite limit, even for an infinite atmosphere, it suffices to consider the density profile given by

Eq. (38), modified for late times by taking the limit $L \to \infty$ and modified for spherical divergence at all radii with appropriate radial scaling. The result is

$$n_e = n_{\text{abs}} \left(\frac{r_{\text{abs}}}{r} \right)^2 , \tag{43}$$

where the absorption surface is located at the radius $r = r_{\text{abs}}$. The maximum plasma contribution to the axial distance parameter for this case, $\zeta_{p\,\max}$, is obtained by evaluating Eq. (9), which gives

$$\frac{\zeta_{p\max}(r_{\text{abs}})}{z_R} = \frac{k_v\, r_{\text{abs}}}{8 f^2} \left[1 - \left(1 - n_{\text{abs}}/n_c \right)^{1/2} \right]. \tag{44}$$

This expression resembles Eq. (40) closely, except that the radius of the absorption surface r_{abs} has replaced the scale length L as the characteristic length of the problem. The dependences on n_{abs}/n_c are qualitatively similar. Equation (44) can be written in practical units as

$$\frac{\zeta_{p\max}(r_{\text{abs}})}{z_R} = 22.8 \frac{\left(\dfrac{r_{\text{abs}}}{500\,\mu\text{m}} \right)}{\left(\dfrac{\lambda_v}{0.351\,\mu\text{m}} \right) \left(\dfrac{f}{7} \right)^2} \left[1 - \left(1 - n_{\text{abs}}/n_c \right)^{1/2} \right]. \tag{45}$$

The maximum axial-averaging interval that can occur, given these nominal parameter values and absorption at the critical surface $\left(n_{\text{abs}} = n_c \right)$, is 22.8 z_R. As before, Eqs. (14) restrict n_{abs} to values consistent with the paraxial approximation, and smaller intervals are obtained for absorption at less than critical density. Equation (44) describes a case where the ablative flow is completely spherical from the absorption surface outward. It does not apply directly to the case where the ablative flow makes a transition from planar flow near the absorption surface to spherical flow at large distances from the target, but it does show that spherical divergence does prevent the axial-averaging interval from growing without limit. This means that a planar model must be applied with caution to cases where a significant contribution to $\zeta_p(z)$ is due to plasma that is diverging from plane-parallel flow.

The Combined Plasma and Hydrodynamic Effects

The motion of the absorption surface relative to the irradiation-intensity distribution is due to both the hydrodynamic motion of the absorption surface and the accumulation of plasma in the propagation path. The essential behavior of these effects and their relative importance can be described and understood by applying Eq. (9) to a planar 1-D isothermal rarefaction model for steady-state ablation of a planar target. At the beginning of the irradiation, when the target is vulnerable to being irreversibly imprinted with the laser nonuniformity, the solid target surface is at rest, and the absorption surface is being convected away from the solid target surface by the expanding atmosphere. At this time, the plasma effect is moving the intensity distribution toward the laser, in the same direction as the motion of the absorption surface, so the hydrodynamic and plasma effects tend to cancel each other. The hydrodynamic effect starts out roughly a factor of 2 faster than the plasma effect. As the target accelerates away from the laser, the hydrodynamic effect begins to reverse, and the plasma and hydrodynamic effects eventually reinforce each other.

In the planar 1-D isothermal rarefaction model, the mass-density profile is of the form of Eq. (38).[21] The growth rate of scale length L is the fluid velocity at the ablation source point at the target's surface, which will be identified below as the isothermal sound speed c_T. Assuming a constant, fixed ionization state, this gives

$$\frac{n_e(z)}{n_s} = \exp\left\{ -\left[\frac{z - z_s(t)}{c_T t} \right] \right\}, \tag{46}$$

where the substitution

$$L = c_T\, t \tag{47}$$

has been made, where n_s is the electron density of the ablated plasma at the source point, and where $z_s(t)$ is the position of the source point at the solid surface. It is assumed that the target motion remains much slower than c_T so that Eq. (46) remains an adequate description of the plasma atmosphere between the target surface and the absorption region, independent of the target's motion.

Given a mass-density profile of the form of Eq. (46), conservation of mass

$$\frac{\partial \rho}{\partial t} + \frac{\partial}{\partial z}(\rho v) = 0 \tag{48}$$

dictates

$$v(z,t) = c_T + \frac{z - z_s(t)}{t}, \tag{49}$$

and the momentum equation

$$\frac{\partial v}{\partial t} + v\frac{\partial v}{\partial z} + \frac{1}{\rho}\frac{\partial P}{\partial z} = 0 \tag{50}$$

is satisfied by the isothermal equation of state

$$P = c_T^2 \rho, \tag{51}$$

where the identification of c_T with the isothermal sound speed is now clear.

The motion of the solid target is obtained by treating it as a planar rocket accelerated by the ablating plasma. Its mass per unit area, M, decreases at a rate determined by the plasma density ρ_s and plasma velocity $v(z_s,t) = c_T$ at the ablation source point,

$$M = M_0 - \rho_s c_T t. \tag{52}$$

The force accelerating the remaining solid target is equal to the rate at which momentum is imparted to the ablation exhaust, which gives

$$M\frac{dV}{dt} = -\rho_s c_T^2, \tag{53}$$

and the solution

$$V = c_T \ln\left(1 - \frac{\rho_s c_T t}{M_0}\right) \tag{54}$$

for velocity V of the remaining solid target. This solution gives a velocity that accelerates smoothly from rest, so the motion of the solid target does not contribute to the motion of the absorption surface at the very beginning of the ablation, $t << M_0/\rho_s c_T$, when the most significant imprinting of the laser nonuniformity occurs.

In estimating the effects of ablation on uniformity, it is assumed here that the absorption of laser energy occurs over a sufficiently short range that one can speak of an absorption surface at a point of fixed density where the irradiation nonuniformity has its effect on the plasma. The absorption surface is identified by the local mass density ρ_{abs}. According to Eq. (46), this absorption surface is positioned ahead of the ablation source by a distance z_{abs} given by

$$z_{abs} = c_T t \ln\left(\frac{\rho_s}{\rho_{abs}}\right). \tag{55}$$

This contribution to the motion of the absorption surface is a constant velocity with respect to the target surface and is the main contribution to the averaging rate at early times. The total motion of the absorption surface, written as the hydrodynamic contribution to the rate of increase of the smoothing distance, $\Delta\zeta$, is

$$\frac{1}{c_T}\frac{d\Delta\zeta_h}{dt} = -\ln\left(1 - \frac{\rho_s c_T t}{M_0}\right) - \ln\left(\frac{\rho_s}{\rho_{abs}}\right). \tag{56}$$

The total effect is obtained by adding to this the plasma contribution to $\Delta\zeta_p$ given by Eq. (41), which gives

$$\frac{1}{c_T}\frac{d\Delta\zeta}{dt} = -\ln\left(1 - \frac{\rho_s c_T t}{M_0}\right) - \ln\left(\frac{\rho_s}{\rho_{abs}}\right) + 2\ln\left[\frac{2}{1+\left(1-n_{abs}/n_c\right)^{1/2}}\right]. \tag{57}$$

This expression can be written entirely in terms of the absorption density as a fraction of the critical density by relating the critical electron density to the solid density of the target ρ_{solid},

$$\frac{\rho_s}{\rho_{abs}} = 38.8\left(\frac{\rho_{solid}}{1\,\mathrm{g\cdot cm^{-3}}}\right)\left(\frac{\lambda_v}{0.351\,\mu\mathrm{m}}\right)^2\left(\frac{Z}{3.5}\right)\frac{\rho_s}{\rho_{solid}}\frac{n_c}{n_{abs}}. \tag{58}$$

The quantities in parentheses are chosen to be unity, which represents fully ionized CH polymer. Equation (57) can now be written as

$$\frac{1}{c_T}\frac{d\Delta\zeta}{dt} = -3.66 - \ln\left[\left(\frac{\rho_{solid}}{1\,\mathrm{g\cdot cm^{-3}}}\right)\left(\frac{\lambda_v}{0.351\,\mu\mathrm{m}}\right)^2\left(\frac{Z}{3.5}\right)\right] - \ln\left(1 - \frac{\rho_s c_T t}{M_0}\right) - \ln\left(\frac{\rho_s}{\rho_{solid}}\right) + 2\ln\left[\frac{2\left(n_{abs}/n_c\right)^{1/2}}{1+\left(1-n_{abs}/n_c\right)^{1/2}}\right]. \tag{59}$$

The first two terms contain only parameters that are fixed by the choice of target and laser, including the density of the cold target material, ρ_{solid}, the laser wavelength λ_v, and a fixed ionization state Z. The third term represents the acceleration part of the hydrodynamic effect, which depends on the initial areal mass of the target M_0 and vanishes in the early-time, $L = 0$ limit. The remaining terms depend only on ρ_s as a fraction of the solid density and n_{abs} as a fraction of the critical density.

Hydrodynamic simulations of the ablation and acceleration of a CH polymer slab by a constant irradiance have been performed using the 1-D hydrocode *LILAC*. The hydrodynamic and plasma contributions to $\Delta\zeta/z_R$ and the total effect are evaluated from these results and plotted as functions of time in Fig. 68.22. The absorption surface is taken to be the centroid of the energy-absorption rate distribution. The hydrodynamic and plasma effects are obtained from the geometric and plasma contributions to the integral in Eq. (9), respectively, which is evaluated from the position of the absorption surface and from the electron-density profile given by the simulation. The solid curves in Figs. 68.22(a), 68.22(b), and 68.22(c) are results obtained from simulations of the ablation of a planar target irradiated by 10^{13}, 10^{14}, and 10^{15} W/cm^2 UV ($\lambda_v = 0.351$ μm), respectively. The target is a CH polymer foil 10 μm thick and 1.0 g/cm^3 in density.

The isothermal-expansion rocket model described above and given by Eq. (59) is fit to the results of the hydrodynamic simulations, including those in Fig. 68.22. The fitted model results are shown in Fig. 68.22 as dashed curves, which accomplishes two things: First, it is seen that the fit is reasonably good over the entire range of intensities, which validates the isothermal expansion model as a basis for describing and deriving preliminary general statements about the effects that lead to axial averaging of speckle over time. Second, the isothermal rocket model serves as a template that can be fit to the simulation results to obtain appropriate values of model parameters and average smoothing rates from the simulations. The separate plasma and hydrodynamic contributions to the total smoothing rate at the very beginning of the irradiation pulse, and the total smoothing rate at that time, were obtained from these fits and plotted as functions of intensity in Fig. 68.23.

The results shown in Figs. 68.22 and 68.23 clearly show that the initial smoothing effect is greatly diminished by the fact that the hydrodynamic and plasma effects counteract each other. These results show that the total initial smoothing rate varies between about 1.5 and 3 Rayleigh lengths per nanosecond over the range of intensities from 10^{13} W/cm^2 to 10^{15} W/cm^2, where the Rayleigh length is the 22-μm value obtained for the nominal parameter values from Eq. (35b).

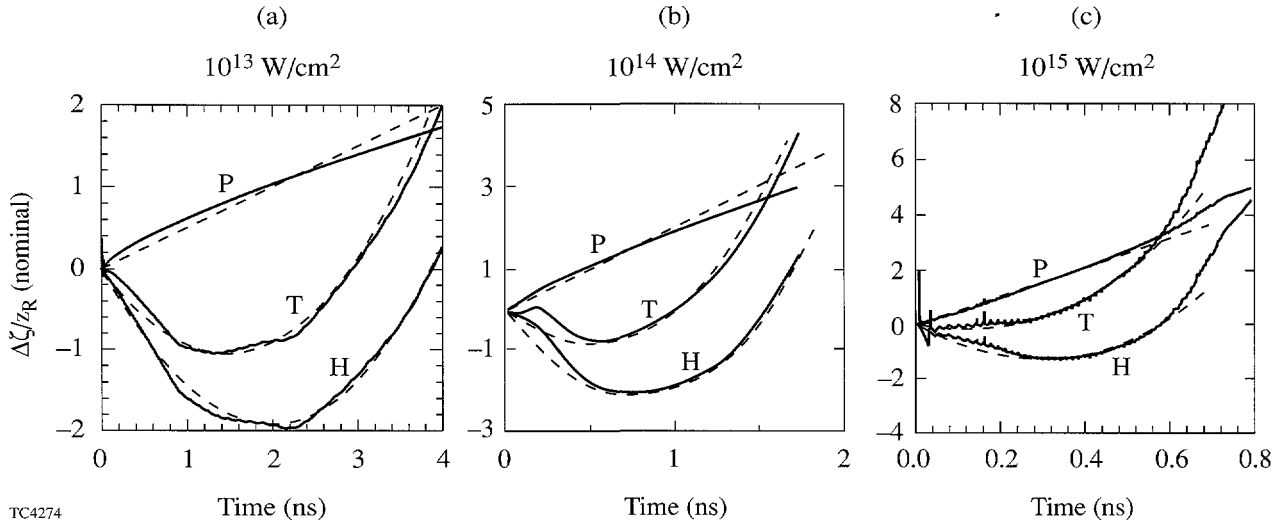

Figure 68.22
The hydrodynamic and plasma contributions to $\Delta\zeta/z_R$ and the total effect are plotted as functions of time. Solid curves are results obtained from numerical simulations of the ablation of a planar target irradiated by 10^{13}, 10^{14}, and 10^{15} W/cm^2 UV ($\lambda_v = 0.351$ μm) in (a), (b), and (c), respectively. The dashed curves are fits of a simple rocket model of planar ablation based on the isothermal expansion of the atmosphere. The value of z_R here is 22 μm, which is obtained from Eq. (35b) for the nominal parameter values.

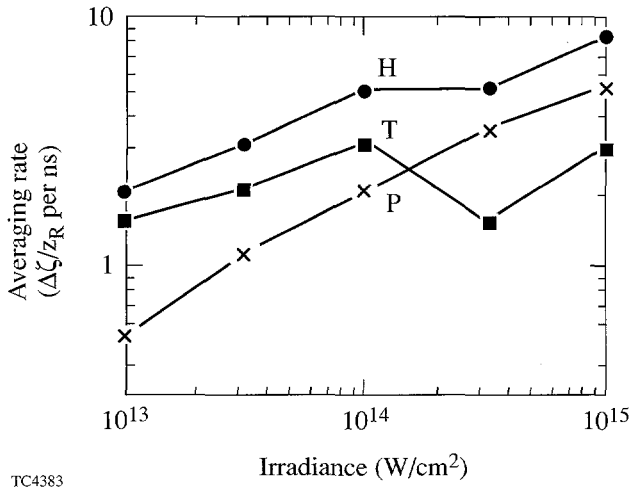

Figure 68.23
The plasma (P) and hydrodynamic (H) contributions to the smoothing rate $1/z_R\ d\Delta\zeta/dt$ and total effect (T) are plotted versus intensity.

Given that the range of required $\Delta\zeta/z_R$ values varies from 2 to 4, as was stated earlier, the range of smoothing times varies from 0.67 ns to 2.67 ns. These smoothing times are comparable to hydrodynamic time scales typical of ICF experiments, but they are longer than other important scale times, such as the time during which the initial nonuniformity of the laser beam is irreversibly imprinted onto the target and the time scale of self-focusing. Averaging as slow as this clearly would not suffice as the sole smoothing mechanism in ICF, but this is not a negligible effect, and it could have an important quantitative significance on certain experimental results where DPP's are used without SSD, such as when measuring the effects of SSD on the outcome of ICF experiments. Of course, variations in focus, wavelength, laser configuration, target geometry, target composition, etc., can give averaging times that vary significantly from these estimates.

To create a situation where the hydrodynamic and plasma effects reinforce each other, a set of numerical simulations was done with a target identical to the 10-μm foil used in the simulations in Figs. 68.22 and 68.23, except that the outermost 2.5 μm of solid CH polymer has been changed to an equal areal mass of 50-μm-thick foam. The hydrodynamic and plasma contributions to $\Delta\zeta/z_R$ and the total effect are plotted in Fig. 68.24(a) as functions of time for the ablation of this target under an irradiation intensity of 10^{14} W/cm^2 UV (λ_v = 0.351 μm), to compare with Fig. 68.22(b). With the foam layer in place, the absorption surface moves away from the laser initially, and the plasma and hydrodynamic effects reinforce each other. The plasma and hydrodynamic contributions to the initial smoothing rate $1/z_R\ d\Delta\zeta/dt$ and the total initial effect are plotted as functions of intensity in Fig. 68.24(b). The isothermal rocket model applied to the homogeneous slab targets is not applicable to this more complicated target, so these rates are estimates obtained by eye. The total smoothing rate is now between about 2.0 and 20.0 Rayleigh lengths per nanosecond over the range of intensities from 10^{13} W/cm^2 to 10^{15} W/cm^2, which corresponds to smoothing times of from

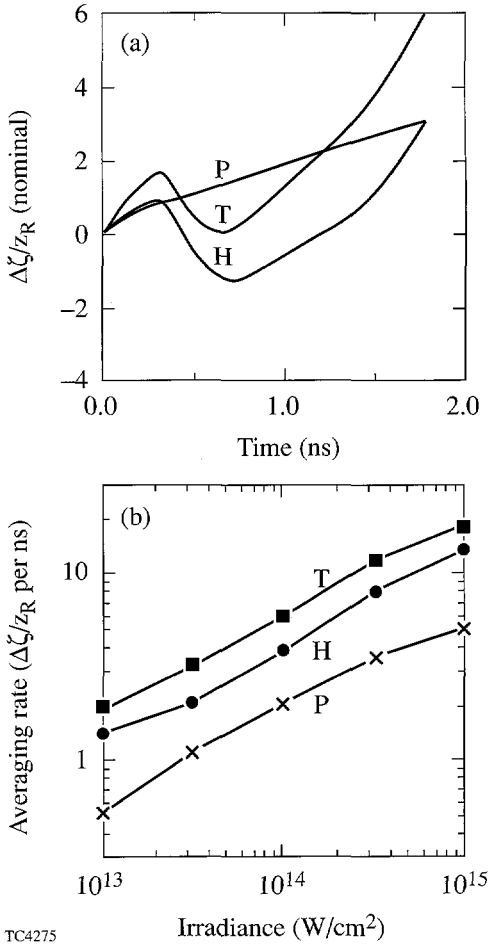

Figure 68.24
The hydrodynamic (H) and plasma (P) contributions to $\Delta\zeta/z_R$ and the total effect (T) obtained from a numerical simulation are plotted in Fig. 68.24(a) as functions of time for the case of the ablation of a planar target irradiated by 10^{14} W/cm^2 UV (λ_v=0.351 μm). The target is identical to the 10-μm foil used in the simulations shown in Fig. 68.22, except that the outermost 2.5 μm of solid CH polymer has been changed to an equal mass of foam 50 μm thick. In this case, the absorption surface moves away from the laser, and the plasma and hydrodynamic effects reinforce each other. The plasma and hydrodynamic contributions to the initial smoothing rate $1/z_R\ d\Delta\zeta/dt$ and the total effect are plotted versus intensity in Fig. 68.24(b). The value of z_R is 22 μm, which is obtained from Eq. (35b) for the nominal parameter values.

100 ps to 2.0 ns, up to more than an order of magnitude faster than is obtained with a solid target.

As stated above, the $(\Delta\nu\, t)^{-1/2}$ asymptotic time dependence of the smoothing effect of SSD and ISI corresponds identically to the $\Delta\zeta^{-1/2}$ asymptotic dependence of the speckle reduction on the averaging interval. When the axial-averaging rate $d\Delta\zeta/dt$ is a constant, an effective bandwidth $\Delta\nu_{\text{axial}}$ can be written for axial averaging and compared with the bandwidth $\Delta\nu_{\text{SSD}}$ specified for an SSD system. Recalling Eq. (37a) and making the identification $r^{-2} = \Delta\nu_{\text{axial}}\, t$, one obtains

$$\Delta\nu_{\text{axial}} = 0.4\,\text{GHz}\left(\frac{\mathbf{q}_0}{R} + 0.5\right)\left(\frac{1}{z_R}\frac{d\Delta\zeta}{dt}\right). \qquad (60)$$

Recalling the $1/z_R\ d\Delta\zeta/dt$ values ranging from 2 to 20 ns^{-1} that were obtained for the foam-coated targets, this corresponds to a range in $\Delta\nu_{\text{axial}}$ from 0.4 to 4.0 GHz for near-normal incidence to 3.2 to 32.0 GHz for $q_0/R = 4.0$ incidence. The upper end of this range is about a factor of 10 below the bandwidth of state-of-the-art SSD systems now being implemented, which gives an asymptotic speckle-reduction effect that is about one third of that obtained with these SSD systems.

Discussion and Conclusions

The main conclusion of this article is that the optical and hydrodynamic effects of uniformly ablating plasma atmospheres in ICF experiments are capable of moving the speckled intensity distributions of phase-converted laser beams over distances that allow significant speckle reduction by time averaging. The rate at which this smoothing occurs varies widely, depending on the composition of the target and the focal convergence, incident angle, wavelength, and intensity of the irradiation. As has been shown above, smoothing times down to 100 ps and smoothing rates well within an order of magnitude of what is currently attained with SSD and ISI are possible under some circumstances. This is enough to warrant consideration of ablation-induced speckle averaging in all experiments, past and future, whose interpretations require a quantitative understanding of the effects of irradiation nonuniformity due to speckle.

For values of target and beam parameters near the nominal values considered above, the time averaging of the speckle nonuniformity due to ablation can be effective over time intervals comparable to and less than the hydrodynamic time scales typical of ICF experiments. As a practical matter, however, speckle-averaging times must be compared with the time scales of competing effects, such as the time needed to imprint the initial nonuniformity of the laser beam irreversibly into the target and the time scale of self-focusing of laser light in the atmosphere. The best generalization that can be made at this time is that ablation-induced time averaging of speckle nonuniformity is unlikely to be decisive as a means of avoiding these effects, but it is potentially significant over the time intervals during which they occur. Understanding ablation-induced speckle smoothing is essential to a complete quantitative understanding of laser-irradiation nonuniformity and its effects in ICF experiments.

An incidental conclusion to be drawn from this work is the interesting point of principle that an ablating plasma does act in some ways to avoid the detrimental effects of irradiation nonuniformity. Ablation-induced time averaging is, in fact, an unavoidable consequence of ablation. This is contrary to the more familiar tendency of ICF plasmas to exacerbate irradiation nonuniformities through the self-focusing of irradiation at intensity peaks and to misdirect the laser energy through laser-driven parametric instabilities.

A logical continuation of this work would be to repeat the calculations without the paraxial approximation. As was pointed out earlier, the paraxial approximation becomes invalid as the irradiation approaches its turning point because the refractive effects become too large. The paraxial approximation also precludes calculating the irradiation of a spherical target because the curvature of the target surface creates large angles of incidence near the limb of the irradiated hemisphere. It has been shown here that the reduction of speckle by axial averaging scales favorably with small incident angles in planar geometry, suggesting that relatively strong averaging effects might be obtained as a result of the broad range of incident angles occurring with a single beam in spherical geometry.

ACKNOWLEDGMENT

This work was supported by the U.S. Department of Energy Office of Inertial Confinement Fusion under Cooperative Agreement No. DE-FC03-92SF19460, the University of Rochester, and the New York State Energy Research and Development Authority. The support of DOE does not constitute an endorsement by DOE of the views expressed in this article.

REFERENCES

1. J. Nuckolls *et al.*, Nature **239**, 139 (1972).

2. R. L. McCrory, J. M. Soures, J. P. Knauer, S. A. Letzring, F. J. Marshall, S. Skupsky, W. Seka, C. P. Verdon, D. K. Bradley, R. S. Craxton, J. A. Delettrez, R. Epstein, P. Jaanimagi, R. Keck, T. Kessler, H. Kim, R. L. Kremens, P. W. McKenty, R. W. Short, and B. Yaakobi, Laser Part. Beams **11**, 299 (1993).

3. C. B. Burckhardt, Appl. Opt. **9**, 695 (1970); Y. Kato and K. Mima, Appl. Phys. B **29**, 186 (1982); Laboratory for Laser Energetics LLE Review **33**, NTIS document No. DOE/DP/40200-65, 1987 (unpublished), p. 1; and Laboratory for Laser Energetics LLE Review **63**, NTIS document No. DOE/SF/19460-91, 1995 (unpublished), p. 1.

4. Y. Kato *et al.*, Phys. Rev. Lett. **53**, 1057 (1984).

5. Laboratory for Laser Energetics LLE Review **64**, NTIS document No. DOE/SF/19460-99, 1995 (unpublished), p. 170.

6. R. H. Lehmberg and S. P. Obenschain, Opt. Commun. **46**, 27 (1983).

7. S. Skupsky, R. W. Short, T. Kessler, R. S. Craxton, S. Letzring, and J. M. Soures, J. Appl. Phys. **66**, 3456 (1989).

8. S. P. Obenschain *et al.*, Phys. Rev. Lett. **56**, 2807 (1986); A. N. Mostovych *et al.*, Phys. Rev. Lett. **59**, 1193 (1987); and S. P. Obenschain *et al.*, Phys. Rev. Lett. **62**, 768 (1989).

9. D. K. Bradley, J. A. Delettrez, and C. P. Verdon, Phys. Rev. Lett. **68**, 2774 (1992); H. A. Baldis *et al.*, Lawrence Livermore National Laboratory Inertial Confinement Fusion ICF Quarterly Report UCRL-LR-105821-93-3 (1993), p. 137; J. Delettrez, D. K. Bradley, and C. P. Verdon, Phys. Plasmas **1**, 2342 (1994); and D. S. Montgomery *et al.*, Phys. Plasmas **3**, 1728 (1996).

10. D. H. Kalantar, M. H. Key, L. B. DaSilva, S. G. Glendinning, J. P. Knauer, B. A. Remington, F. Weber, and S. V. Weber, Phys. Rev. Lett. **76**, 3574 (1996).

11. M. Desselberger *et al.*, Phys. Rev. Lett. **68**, 1539 (1992).

12. T. Dewandre, J. R. Albritton, and E. A. Williams, Phys. Fluids **24**, 528 (1981).

13. R. E. Kidder, Nucl. Fusion **16**, 3 (1976).

14. S. Skupsky and K. Lee, J. Appl. Phys. **54**, 3662 (1983).

15. S. E. Coe, T. Afshar-rad, and O. Willi, Opt. Commun. **73**, 299 (1989).

16. K. Okada *et al.*, Appl. Phys. Lett. **42**, 231 (1983); T. Afshar-rad *et al.*, Phys. Rev. Lett. **73**, 74 (1994); M. Desselberger *et al.*, Phys. Rev. Lett. **74**, 2961 (1995); and M. Dunne *et al.*, Phys. Rev. Lett. **75**, 3858 (1995).

17. Y. Takeda, Y. Oshida, and Y. Miyamura, Appl. Opt. **11**, 818 (1972).

18. R. Epstein and S. Skupsky, J. Appl. Phys. **68**, 924 (1990).

19. P. W. Milonni and J. H. Eberly, *Lasers* (Wiley, New York, 1988), p. 486.

20. S. Skupsky, private communication (1996).

21. K. A. Brueckner and S. Jorna, Rev. Mod. Phys. **46**, 325 (1974).

Microwave Phase Modulators for Smoothing by Spectral Dispersion

A principal component of smoothing by spectral dispersion (SSD) is an electro-optic phase modulator that produces a cyclic wavelength modulation on nanosecond laser pulses. This article addresses the theory, design, manufacture, testing, and implementation of microwave phase modulators operating in the gigahertz-frequency range with particular application to both one- and two-dimensional SSD on the OMEGA laser system.

The first references in the literature to electro-optic modulators in the microwave-frequency range were in the early 1960s in applications of both amplitude and phase modulators to the recently invented laser. Most of these devices were wideband devices operating over the band from dc to some upper cutoff frequency for analog modulation[1] or over some narrow radio-frequency RF band for digital communications.[2] Early work concentrated on frequency-shifting laser beams for spectroscopic applications, especially FM heterodyne spectroscopy, but was usually confined to continuous-wave (cw) gas lasers, as well as some applications to temporal compression of short pulses generated by cw mode-locked gas laser oscillators.[3]

No work appears to have been done on modulators of the type needed for SSD that must impress relatively large bandwidths (several Å) in a single pass through an electro-optic crystal of relatively large cross section. Commercially available, guided-wave phase modulators can achieve large modulation bandwidths; however, the small cross section of these devices and the relatively low damage threshold of electro-optic materials are incompatible with the relatively high-power laser pulses typical in driver lines of large glass lasers used for inertial confinement fusion (ICF) applications. Furthermore, bulk electro-optic modulators enable the technique of "color cycling," which is critical to the successful implementation of SSD.[4]

SSD phase modulators have been employed on the OMEGA laser in several configurations. Originally, resonant modulators in the 2- to 3-GHz regime were employed in a scheme now identified as one-dimensional smoothing by spectral dispersion (1-D SSD).[5] In this scheme, a bandwidth is generated by a single modulator, and dispersion is applied along a single direction. Bandwidths of up to 2 Å were achieved with these original modulators. A higher-frequency modulator operating around 9 GHz was also operated in this configuration that achieved bandwidths in excess of 8.5 Å.

Two-dimensional SSD (2-D SSD) is currently implemented on OMEGA. This configuration involves two separate stages of gratings and modulators that apply dispersion in two orthogonal directions. Incommensurate modulation frequencies (3.0 and 3.3 GHz) are chosen for the two modulators to maximize the spectral content of the phase-modulated laser beam.

In the following sections, we present (1) the basic theory involved in microwave phase modulators; (2) computer simulations that used *SUPERFISH* to design the SSD modulators; (3) a review of the technical design criteria leading to the current modulator designs; and finally, (4) the testing results for these devices.

Theory

Phase modulation of laser pulses increases the bandwidth of laser pulses without introducing intensity modulation to the laser pulse that could be destructive to the glass laser system. The electric field of a phase-modulated pulse takes the form[6]

$$E(t) = E_0(t)\, e^{i\omega_0 t}\, e^{i\Phi(t)},$$

where $E_0(t)$ represents the pulse shape before phase modulation, ω_0 is the fundamental angular frequency of the laser, and $\Phi(t)$ is the time-varying phase. Since the laser intensity varies as $|E(t)|^2 = |E_0(t)|^2$, intensity modulation is avoided. The time-varying phase is achieved by passing the laser beam through an electro-optic crystal with an oscillating voltage applied across it. The resulting electric field of the laser beam is of the form

$$E(t) = E_0(t)e^{i\omega_0 t + i\eta\sin(\omega_m t)}$$
$$= E_0(t)e^{i\omega_0 t}\sum_{n=-\infty}^{\infty} J_n(\eta)e^{i(\omega_0 + n\omega_m t)}, \quad (1)$$

where η is the phase-modulation amplitude and ω_m is the angular frequency of the modulation. The added bandwidth can be expressed as a Bessel-series expansion of the sinusoidal phase term, or frequency sidebands separated by the modulation frequency. The frequency bandwidth impressed by the phase modulation is conveniently characterized by $\Delta f = 2\eta f_m$, at which point the mode amplitudes $J_n(\eta)$ rapidly approach zero. For light near 1-μm wavelength, a bandwidth of 30 GHz corresponds to approximately $\Delta\lambda = 1$ Å.

The modulation amplitude η for a transverse-field, $LiNbO_3$ phase modulator shown in Fig. 68.25 is given by[6]

$$\eta = \frac{\pi \cdot \beta \cdot n_3^3 r_{33}(V/T)L}{\lambda}, \quad (2)$$

where L is the length of the $LiNbO_3$ crystal in the direction of laser propagation, T is the thickness in the direction of the oscillating voltage, and W is the width. The reduction factor β accounts for phase mismatch between the propagating optical and microwave fields in the crystal, n_3 is the index of refraction for the optical field polarized parallel to the c-axis of $LiNbO_3$, r_{33} is the electro-optic coefficient, $V_{applied}$ is the microwave voltage applied along the crystalline axis of the crystal, and λ is the wavelength of the laser light.

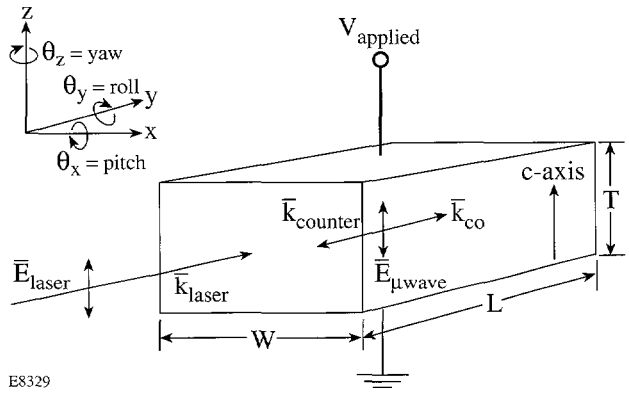

Figure 68.25
Geometry of $LiNbO_3$ crystal used in phase modulator.

The phase-mismatch reduction factor β is the usual term characteristic of nonlinear optical processes. In the resonant microwave cavities used for SSD phase modulators, microwave standing waves are impressed across the electro-optic crystal that can be decomposed into fields co-propagating $(\bar{k}_{co})$ and counter-propagating $(\bar{k}_{counter})$ with the laser beam. The phase-mismatch reduction factor is given by[7]

$$\beta = \frac{1}{2}\left|\frac{\sin(u_+)}{u_+} + \frac{\sin(u_-)}{u_-}\right|, \quad (3a)$$

and

$$u_\pm = \left(\frac{\pi f_m L}{c}\right)\left(\sqrt{\varepsilon_3} \mp n_3\right), \quad (3b)$$

where ε_3 is the relative dielectric constant of the electro-optic crystal for the polarization of the applied microwave field at the modulation frequency f_m, and c is the speed of light in vacuum. The first term of Eq. (3a) accounts for the contribution of the interaction with the co-propagating microwave, while the second term is associated with the counter-propagating microwave field.

Figure 68.26 shows a block diagram of the SSD modulator subsystem. Microwave pulses with peak powers in the kilowatt range and pulse lengths of several microseconds are generated by a mechanically tuned, triode microwave power oscillator. A ferrite circulator isolates the power oscillator from microwave drive power reflected from the SSD modulator, while a directional coupler is used to sample the incident and reflected power to the SSD modulator for system diagnostic purposes. A variable attenuator is included in the microwave circuit to control the drive-power level without changing the power oscillator operating point that can affect its operating frequency. A double-stub tuner is used to match the impedance of the modulator cavity to the 50-Ω coaxial cable that transmits the microwave drive power to the modulator.

Large phase amplitudes ($\eta \sim 3\pi$) are required to achieve the infrared laser bandwidths (~1.5 Å) from a single modulator required for successful implementation of 2-D SSD in laser-fusion experiments. To achieve these large phase amplitudes, thousands of volts must be applied across the electro-optic crystal at microwave frequencies. The microwave drive powers required to achieve these voltages in traveling-wave phase-modulator geometries are impractical, so resonant cavities are used to reduce the microwave drive-power requirements.

Two basic resonant cavity designs have been used for SSD phase modulators: radial-mode and reentrant coaxial-mode

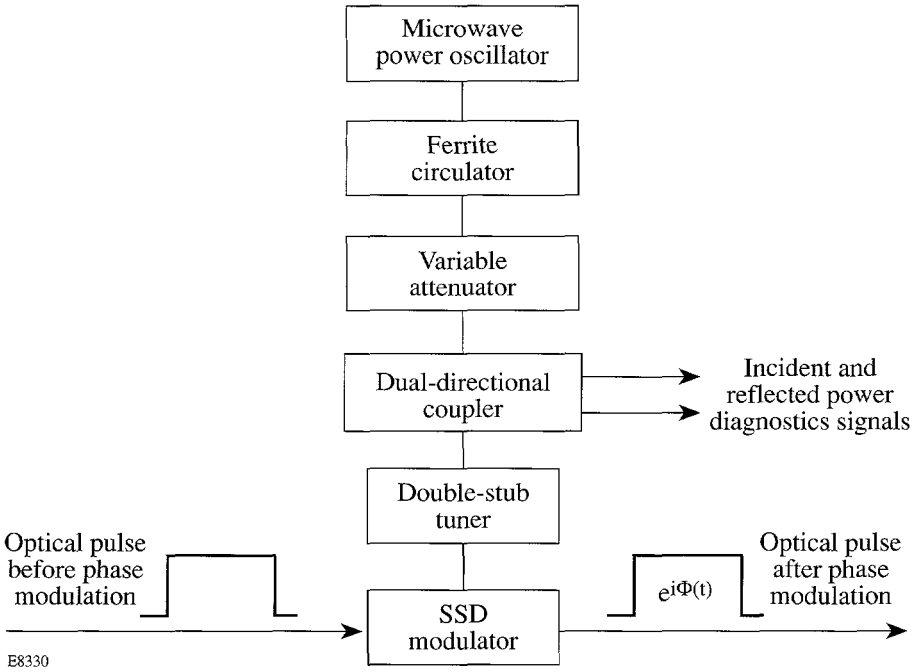

Figure 68.26
Block diagram of SSD modulator subsystem.

resonators. Early work at LLE was modeled after Kaminow's work[8] using radial-mode cavities with large crystals. In these designs, the diameter of the cavity is much larger than its overall height, and the electromagnetic wave inside the cavity propagates in the radial direction. Figure 68.27(a) shows a cutaway drawing of such a radial-mode cavity. Figure 68.27(b) illustrates a cross section of this modulator cavity along with the electric field distribution for a typical radial mode. The electric fields of this mode align with the symmetry axis of the cylindrical cavity, while the magnetic field lines are circular in horizontal planes. Microwave energy is coupled into the cavity using a magnetic loop antenna located on the outer wall of the cavity where the magnetic-flux density is a maximum.

As discussed later in **Computer Simulations Using *SUPERFISH***, spurious resonant modes can arise with resonance frequencies near the desired operating frequency. Additional difficulties with this design arise when the crystal dimensions approach the modulator cavity dimensions. Specifically, separate crystal resonance modes can exist above cutoff when the crystal thickness is nearly equal to the height of the cavity. Difficulties in efficiently coupling cavity-mode energy into the crystal mode prompted the use of highly reentrant coaxial cavities that proved to be significantly simpler to analyze and engineer.

A typical reentrant coaxial resonator is depicted in Fig. 68.28(a), which is essentially a section of coaxial transmission line that is short circuited at one end and capacitively loaded by the electro-optic crystal at the other end. The theory of reentrant coaxial resonators is discussed in many microwave references.[9–13] In this cavity geometry, predominantly transverse electromagnetic (TEM) waves propagate in the transmission-line section of the cavity, as shown in Fig. 68.28(b), while the fields at the capacitively loaded end conform to the end geometry. The electrode structures are made as large as possible, compared to the crystal size, to maximize the axial electric field uniformity in the electro-optic crystal. A magnetic loop antenna that couples microwave energy into the cavity is located near the center conductor at the short-circuited end of the transmission line.

The reentrant coaxial resonator design offers several advantages over the radial-mode designs. First, cavity-mode resonance frequencies are well separated, which simplifies excitation of only the desired cavity mode. Setting the resonance frequency is accomplished by machining the cavity length using analytical models that have been developed for this cavity design.

The dimensions of a reentrant coaxial resonator are determined by the properties of a coaxial transmission line. The impedance at a reference plane of a lossless, air-dielectric coaxial line of length L, with a characteristic impedance of Z_0 that is short circuited at its end, is given by[10]

$$Z_i = j Z_0 \tan\left(\frac{2\pi f_m L}{c}\right) (\text{ohms}), \tag{4}$$

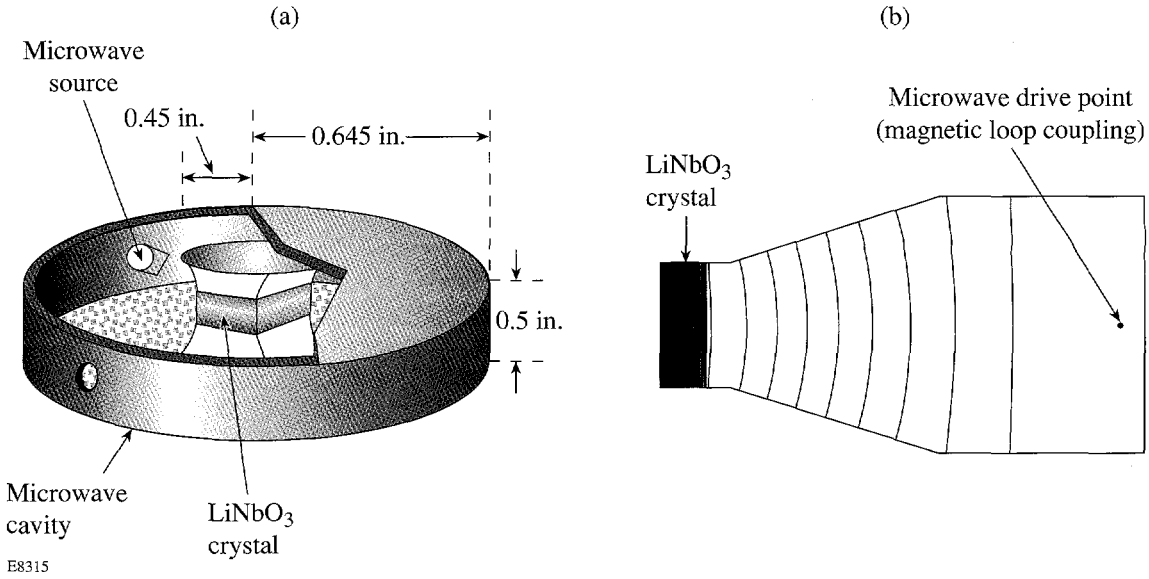

Figure 68.27
(a) Radial-mode cavity; (b) *SUPERFISH* field distribution.

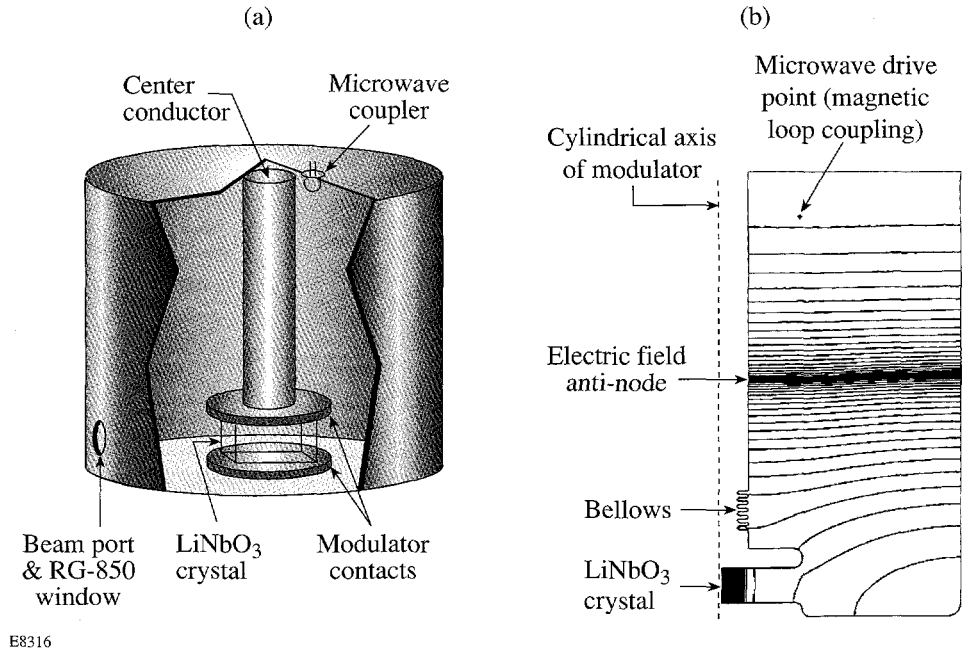

Figure 68.28
(a) Reentrant coaxial-mode cavity; (b) *SUPERFISH* field distribution.

where f_m is the microwave frequency and c is the speed of light. The characteristic impedance Z_0 can be calculated by the usual formula[11]

$$Z_0 = \frac{1}{2\pi}\sqrt{\mu/\varepsilon}\,\ln(b/a) \cong 60\ln\frac{b}{a}\ \text{(ohms)}, \qquad (5)$$

where b is the inner radius of the outer conductor and a is the outer radius of the inner conductor.

By definition, resonance in a transmission-line cavity occurs when an external shunt reactance is connected to the transmission line that is equal to and opposite in sign to Z_i. For an open-circuited line, resonance occurs for values of f_m, which make the right-hand side of Eq. (4) infinite. This condition is satisfied when[10]

$$L = \left(\frac{2k-1}{4}\right)\lambda_m, \qquad (6)$$

where k is any positive integer and $\lambda_m = c/f_m$ is the free-space wavelength of the microwave field. Equation (6) is the familiar odd-quarter-wave cavity length condition. Capacitively loaded lines can be treated with the same analysis to yield a "universal tuning curve." Since the reactance of the capacitor terminating the length of transmission line is given by

$$X_c = \frac{j}{2\pi f_m C}, \qquad (7)$$

resonance occurs when Eqs. (4) and (7) are equal and opposite, leading to the analytic expression[10]

$$\tan\left(\frac{2\pi L}{\lambda_m}\right) = \frac{\lambda_m}{2\pi c\, C_{\text{total}}\, Z_0}. \qquad (8)$$

The transmission line length normalized to the desired microwave wavelength λ_m is plotted in Fig. 68.29 versus this microwave wavelength normalized to the loaded transmission line characteristics. Equation (8) is a multivalued transcendental resonance condition with solutions for L, which are separated by $\lambda_m/2$.

This "universal tuning curve" determines the cavity length, given a known terminating capacitance, longitudinal mode number, and desired resonant frequency. Since the left-hand side of Eq. (8) repeats every half-wavelength, a resonance condition analogous to the odd-quarter-wavelength condition in Eq. (6) exists. Inspection of this curve shows that as the terminating capacitance approaches zero, the length of the resonator approaches one quarter of the free-space wavelength corresponding to the resonant frequency. As the capacitance becomes larger and larger, the length of the resonant cavity gets shorter. The 3/4 λ resonator mode is depicted in Fig. 68.28(b). It should be noted that the simplified analysis leading to Fig. 68.29 is not exact since stray capacitance due to fringing effects is difficult to quantify exactly.

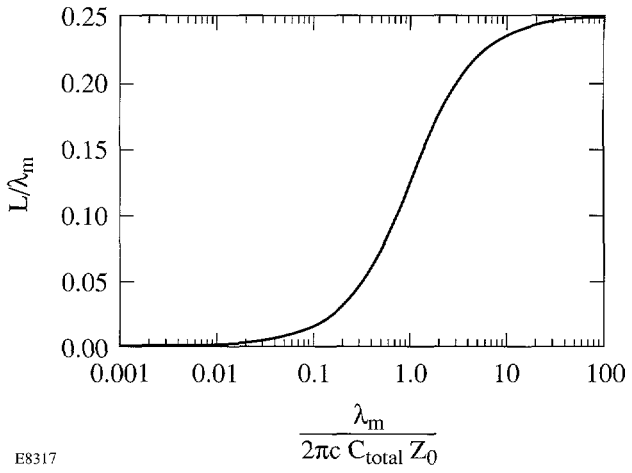

Figure 68.29
The "universal tuning curve" for reentrant coaxial resonators from Eq. (8) determines the cavity length of the $\lambda/4$ TEM mode of the modulator resonator. The cavity length of higher-order longitudinal modes is found by adding integer half-wavelengths.

Near resonance, a microwave cavity may be modeled as the parallel RLC resonant circuit shown in Fig. 68.30, where the shunt resistance R_s represents all of the losses in the cavity. Unfortunately, the appropriate definitions for R_s, L, and C are

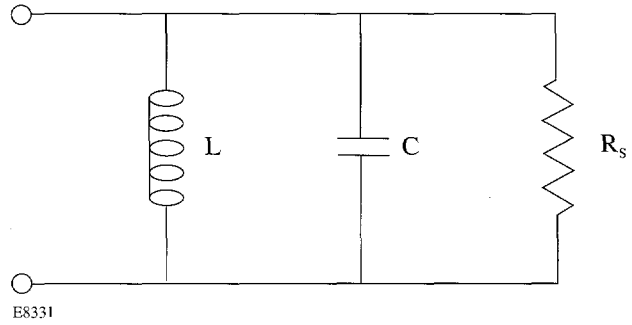

Figure 68.30
Near resonance, a resonant microwave cavity can be represented by an equivalent RLC circuit with a characteristic shunt impedance R_s.

somewhat ambiguous and arbitrary for a cavity resonator.[9] A more convenient set of parameters that totally describes the resonance is the cavity resonance frequency f_0, the "Q factor," and the shunt resistance R_s. For a given cavity mode, f_0 and the Q factor, or simply Q, are well-defined and can be calculated based on the size and shape of the cavity, as well as the materials and fabrication techniques employed in constructing the cavity. The definition of shunt resistance depends on the location where the voltage is defined, but it is conventional to define the path along which the electric field will be integrated to give the maximum voltage.[9] For SSD modulators, this corresponds to the voltage across the electro-optic crystal.

The Q of a resonant circuit or cavity is defined by[9]

$$Q = 2\pi\left(\frac{E_{\text{stored}}}{E_{\text{loss}}}\right), \tag{9}$$

where E_{stored} is the energy stored in the resonant cavity per cycle, and E_{loss} is the energy lost per cycle to conduction in the cavity walls and lossy dielectric materials inside the cavity. At a resonance frequency, the stored energy oscillates between the magnetic and electric fields. Since the electro-optic crystal in SSD modulators represents a capacitive load, a definition of stored energy in terms of the total capacitance of the modulator cavity is appropriate, and the stored energy is given by

$$E_{\text{stored}} = 1/2\, C_{\text{total}} V_{\text{peak}}^2, \tag{10}$$

where V_{peak} is the peak voltage achieved across the electro-optic crystal. The total cavity capacitance,

$$C_{\text{total}} = C_{\text{crystal}} + C_{\text{cavity}} + C_{\text{stray}},$$

is the sum of the capacitance due to the crystal, the cavity geometry, and stray capacitance due to fringing effects. Calculating the capacitances of the crystal and the cavity geometry is relatively straightforward, but estimating the stray capacitance can be quite difficult.

In the steady state, the energy lost per cycle is exactly balanced by the energy per cycle flowing into the cavity, so $E_{\text{loss}} = P_{\text{in}}/f$. Combining Eqs. (9) and (10) yields

$$V_{\text{peak}} = \sqrt{\frac{QP_{\text{in}}}{C_{\text{total}}\,\pi f}}, \tag{11}$$

which shows that minimizing the modulator capacitance is advantageous for generating the highest peak voltage across the crystal. In a general sense, a large-cavity Q factor also maximizes the voltage developed, although the effective shunt resistance of the cavity described below also plays an important role.

Assuming the crystal capacitance dominates the total modulator capacitance ($C_{\text{total}} \approx C_{\text{crystal}}$), the expression for a parallel plate capacitor ($C = \varepsilon WL/T$) can be combined with Eqs. (2) and (11) to yield

$$\eta^2 = \frac{\pi Q P_{\text{in}}}{\lambda^2 \varepsilon_0 f_m}\left(\frac{\beta^2}{WLT}\right)\left(\frac{n_3^6 r_{33}^2}{\varepsilon_r}\right), \tag{12}$$

where $\varepsilon = \varepsilon_r \bullet \varepsilon_0$, ε_r is the relative dielectric constant, ε_0 is the dielectric constant of vacuum, and $W \cdot L \cdot T$ is the volume of the crystal, as depicted in Fig. 68.25. The first term is a constant for a given cavity design, modulation frequency, laser wavelength, and operating power. The second term depends only on the electro-optic crystal dimensions, although the phase-mismatch reduction factor β also depends on the material properties of the electro-optic crystal. It can easily be seen from Eq. (12) that small volume crystals are advantageous to achieving large phase-modulation amplitudes. The last term is a conventional figure-of-merit for electro-optic materials.

Assuming a sinusoidal voltage variation and steady-state conditions where the input power matches the average losses, or

$$P_{\text{in}} = V_{\text{peak}}^2/2R_s, \tag{13}$$

the peak voltage developed in the cavity, V_{peak}, can be expressed as

$$V_{\text{peak}} = \sqrt{2\,P_{\text{in}} R_s}. \tag{14}$$

Equation (14) reveals the same square-root dependence on input power observed in Eq. (11); however, the coefficient now depends on the effective shunt impedance that is a function of cavity design. In some circumstances, maximizing the effective shunt resistance is more important than maximizing the Q factor when trying to achieve the highest voltages across the electro-optic material.

An important quantity in evaluating Q and R_s for a resonant cavity is the skin depth δ. At high frequencies, electromagnetic waves cannot penetrate deeply into conducting material.

The skin depth δ is defined as the depth at which the current density has fallen to 1/*e* of its value at the surface, and it can be calculated from[14]

$$\delta = \sqrt{\frac{2}{\mu \omega_m \sigma}}, \tag{15}$$

where ω_m is the microwave angular frequency, σ is the conductivity of the material, and μ is the magnetic permeability of the material. For gold, the skin depth at 3.0 GHz is approximately 1.5 μm.

If dielectric losses in the electro-optic material can be neglected, then conduction losses in the metallic walls of the resonator represent the only losses in Eqs. (9) and (13), and both Q and R_s can be analytically evaluated by straightforward means for a capacitively loaded, reentrant coaxial cavity resonator to yield[9]

$$Q = \left(\frac{2z}{\delta}\right) \frac{\ln k}{2\ln k + z\left(\frac{k+1}{ka}\right)}, \tag{16}$$

and

$$R_s = 240\pi z^2 \frac{1}{\lambda_m \delta} \frac{[\ln(k)]^2}{2\ln(k) + z\left(\frac{k+1}{ka}\right)}, \tag{17}$$

where z is the inside height of the cavity, a is the radius of the center post, $k = b/a$ is the ratio of the inner cavity radius to the center post radius, λ_m is the free-space wavelength, and δ is the skin depth of the cavity material at the resonant frequency. Figure 68.31 shows Eqs. (16) and (17) plotted using dimensions for 3-GHz, gold-plated SSD modulators built for OMEGA. It can be seen that the shunt resistance calculated using this simplified model actually peaks for larger values of b/a than the Q factor. More exact calculations show that a maximum for the shunt resistance occurs when $z \approx (b-a)$, which corresponds to a square toroidal cross section.[9]

The utility of increasing the outer radial dimension of a cavity to maximize the shunt resistance is limited by the emergence of cavity modes with higher-order azimuthal variations. Figure 68.32 reproduces tuning curves for several of the TEM and TE_{11} modes of a reentrant-coaxial-cavity[10] to illustrate the difficulties created by degenerate cavity modes. The cavity resonance wavelength λ normalized to the cutoff wavelength λ_c for TE_{11} modes is plotted versus the normalized length of the coaxial section of the cavity, L/λ_c. For wavelengths shorter than the TE_{11} cutoff wavelength λ_c, numerous degenerate points exist between various TEM and TE_{11} modes, as indicated by the intersections marked with dots. For example, a common resonance wavelength is found for both the $\lambda_g/2$ TE_{11} mode and the $3\lambda/4$ TEM mode for one cavity length value. Degenerate modes, or nearly degenerate modes, degrade modulator performance since drive power may be coupled into another mode that does not exhibit a voltage maximum across the electro-optic crystal. Consequently, care must be taken in the cavity and coupling designs to excite only the desired cavity mode. A rule of thumb to identify the cavity dimensions at cutoff for these higher-order modes is that the mean circumference of the cavity, $L_{avg} = \pi(a+b)$, should be smaller than the desired free-space wavelength λ.[12]

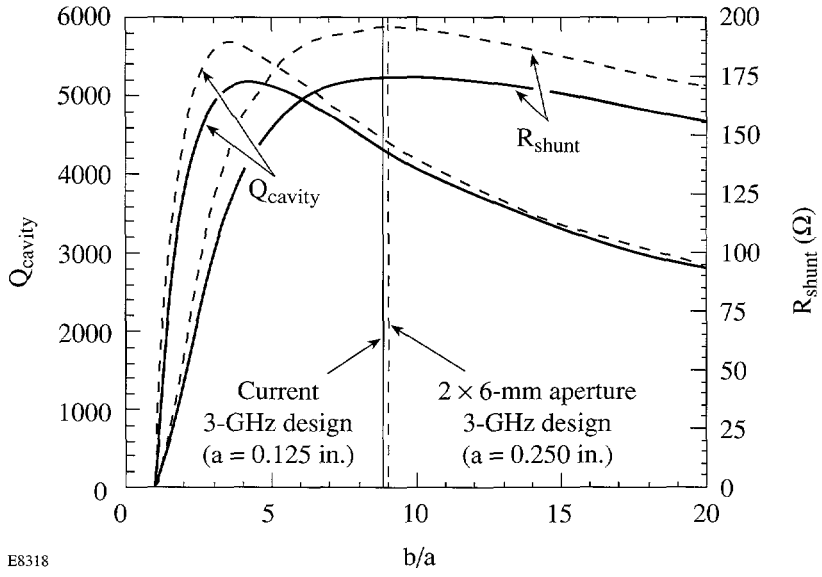

Figure 68.31
The approximate expressions for the cavity Q and shunt resistance for a reentrant coaxial-mode cavity exhibit peaks at different values for the ratio of the outer and inner radius, b/a. The solid lines represent the calculated values for the current, small-cavity 3.0-GHz modulator design (a = 0.125 in., b = 1.100 in., z = 2.000 in.), while the dashed lines are for the 2 × 6-mm aperture, large-cavity modulator (a = 0.250 in., b = 2.250 in., z = 2.170 in.). In both cases, the shunt resistance R_s is optimized.

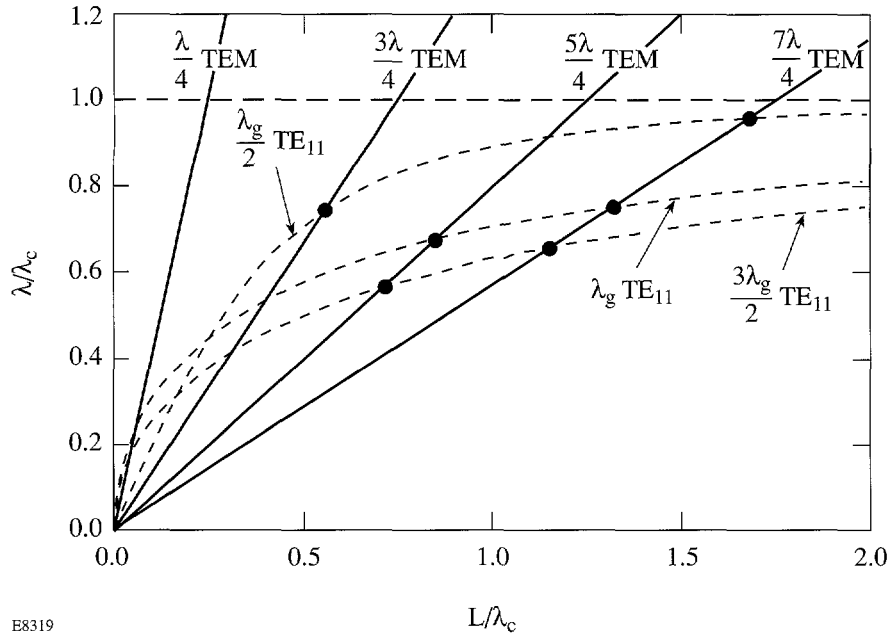

Figure 68.32
The tuning curves for several TEM and TE_{11} modes of a reentrant-coaxial-cavity illustrate the difficulties created by degenerate cavity modes (from Reich *et al.*[10]). The dots indicate degenerate points where two cavity modes have the same resonance wavelength for a given cavity length.

Computer Simulations Using *SUPERFISH*

Design and modeling of SSD modulators has been accomplished using the personal computer version of the *SUPERFISH* collection of programs developed at the Los Alamos National Laboratory.[15] The *SUPERFISH* package solves Maxwell's equations in two dimensions for both static magnetic and electric fields, as well as radio-frequency electromagnetic fields using finite element analysis. The codes analyze a user-defined cavity geometry to generate a triangular mesh that is subsequently used in the finite element analysis of the wave equation. Radio-frequency solvers iterate on the frequency and field calculation until finding a resonant mode of the cavity.

SUPERFISH numerical simulations of SSD modulators are limited to axially symmetric geometries. Given the rectangular geometry of the electro-optic crystal, SSD modulators are not strictly axially symmetric, but reasonably accurate results suitable for design purposes are achieved by modeling the crystal as a cylindrical crystal with an equivalent capacitance. The anisotropy of the $LiNbO_3$ crystals used in SSD modulators also cannot be modeled in *SUPERFISH*, but anisotropic effects should be minimal since the crystals are centered on the symmetry axis of the cavity where transverse fields should be very small.

Analyzing the field distributions of various cavity modes calculated by *SUPERFISH* is useful in identifying the optimal cavity design and drive frequency. Figure 68.33(a) displays a half cross section of the current-design OMEGA SSD modulator. Lines of constant electric field for the excited cavity mode are also shown, where the density of lines indicates the strength of the electric field. The electric fields of the standing wave in the transmission-line section of the cavity are essentially transverse, and a strong, axial electric field is observed in the electro-optic crystal between the electrodes, as expected from the analysis above.

Figure 68.33(b) shows the calculated radial dependence of the axial electric field component, E_z, in the equivalent cylindrical crystal at the three different horizontal positions shown in Fig. 68.33(a). Little variation is observed in the axial direction. Almost a 25% variation is calculated across the full radius of the equivalent cylindrical $LiNbO_3$ crystal, but smaller transverse variations are expected across the aperture of the actual rectangular $LiNbO_3$ crystal since the actual transverse dimensions are smaller. Of course, the exact field distribution is actually somewhat more complicated than calculated using this model since the $LiNbO_3$ crystal is actually a rectangular prism located in the center of an otherwise axially symmetric cavity. The calculated radial component of the electric field, E_r, is approximately 1000 times smaller than the axial electric field component, as expected from the symmetry of the modulator.

Figure 68.34(a) illustrates the electric field distribution of a new SSD modulator design currently being developed for the second stage of the two-dimensional SSD scheme implemented in OMEGA. A clear aperture with a larger dimension in the axial direction is required to accommodate a sweep of the laser beam at the second SSD modulator caused by the band-

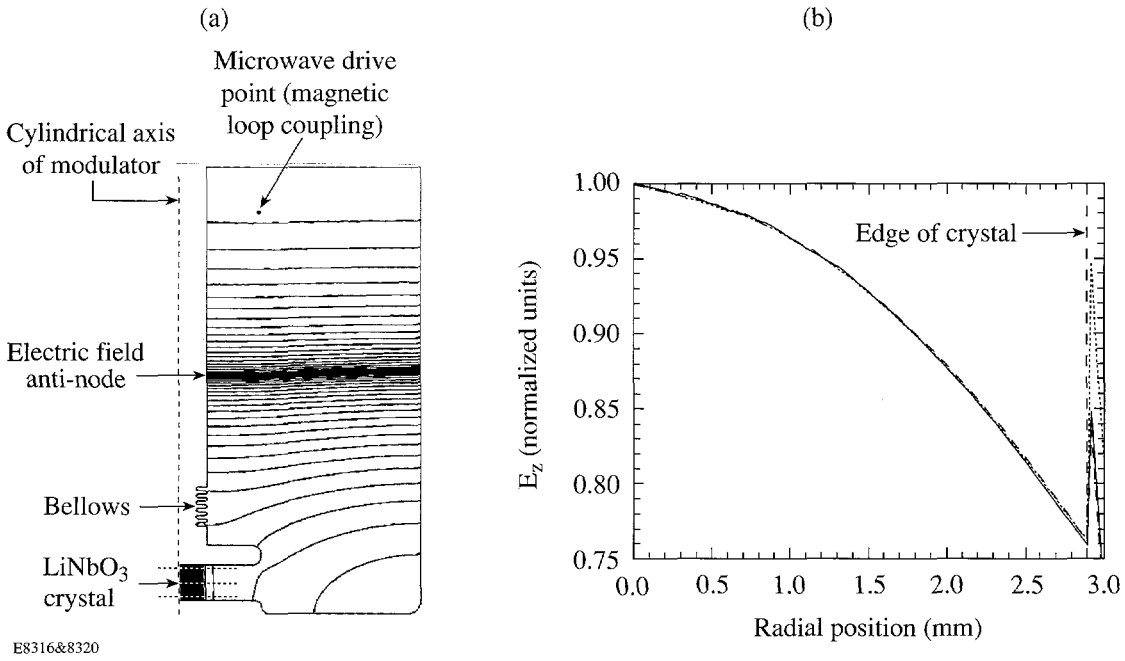

Figure 68.33
The electric field distribution for the small-cavity SSD modulator design. (a) A nearly TEM field distribution is observed in the "coaxial" section of the cavity. In this representation, the plotted field lines are parallel to lines of constant electric field and the electric field strength is related to the density of lines. (b) The radial dependence of the calculated electric field distribution is plotted for the three horizontal positions noted in Fig. 68.33(a). Little variation is observed among the three plots, but almost a 25% variation is predicted across the full radius of the equivalent cylindrical $LiNbO_3$ crystal. Smaller transverse variations are expected across the aperture of the actual rectangular $LiNbO_3$ crystal since the actual transverse dimensions are smaller.

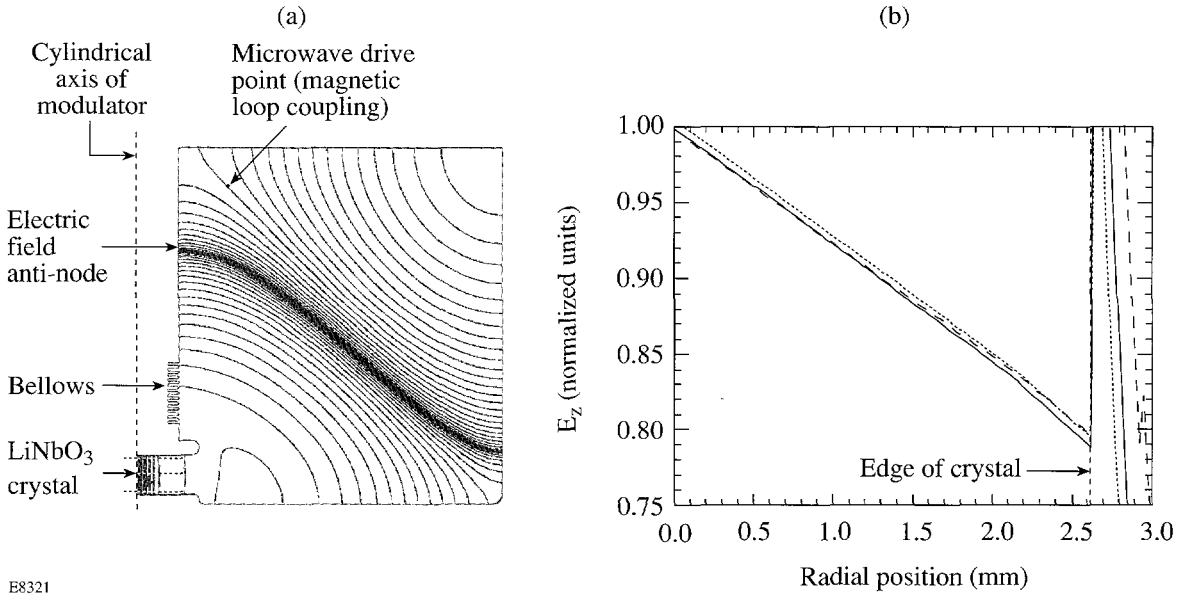

Figure 68.34
Electric field distribution for large-cavity SSD modulator. (a) The cavity mode is clearly not a TEM distribution in the "coaxial" section of the cavity; however, strong electric fields in the $LiNbO_3$ crystal are calculated, as represented by the high density of field lines. (b) The radial dependence of the calculated electric field distribution are plotted for the three horizontal positions noted in Fig. 68.34(a). Little variation is observed among the three plots, but approximately a 20% variation is predicted across the full radius of the equivalent cylindrical $LiNbO_3$ crystal.

width and dispersion introduced in the first stage of SSD. The aspect ratio b/a for this modulator is similar to the current design depicted in Fig. 68.33(a), but the larger radial dimensions lead to somewhat higher values for Q and R_s, as shown in Fig. 68.31. This new design was pursued with the goal of generating larger voltages across the electro-optic crystal required to achieve the same electric field strengths as in the current design.

The electric field distribution of the cavity mode displaying the strongest fields in the $LiNbO_3$ crystal is shown in Fig. 68.34(a). It differs remarkably from the current SSD modulator design in that the electric fields clearly are not transverse in the "transmission line" section of the cavity. Strong, relatively uniform axial components of the electric field in the crystal are calculated, as shown in Fig. 68.34(b), indicating that this design should be suitable for SSD operation. Compared to the small-cavity modulator design, the smaller transverse dimension of the $LiNbO_3$ crystal aperture should produce even smaller radial variations. Again, the calculated radial component E_r was found to be negligible compared to the axial component.

Experimental tuning curves for cavity modes of the large-cavity SSD modulator were measured by adjusting the cavity length of the resonator with aluminum shim plates between the cover assembly and cavity body. These measured resonance frequencies are compared in Fig. 68.35 with resonance frequencies numerically calculated by *SUPERFISH*. The numerical and measured tuning curves for this design agree remarkably well, but they depart substantially from the analytical form given by Eq. (8). This departure confirms that the actual modes of this modulator cavity are not consistent with the TEM mode analysis used to derive Eq. (8).

The lowest-frequency cavity mode tracked as a function of cavity length corresponds to a nearly radial mode, while the next higher frequency matches the calculated tuning curve for the nearly axial mode shown in Fig. 68.34(a). Both of these modes were reproduced by the *SUPERFISH* simulations, which predict the tuning variations with reasonable accuracy; however, three additional, higher-frequency cavity modes are experimentally observed that cannot be reproduced by any axially symmetric *SUPERFISH* solutions. Two nearly degenerate resonance modes appear that are most likely two similarly shaped modes that are slightly perturbed by the rectangular symmetry introduced by either the $LiNbO_3$ crystal or the magnetic coupling loop. The measured tuning curves for these modes actually cross the tuning curve for the nearly axial mode in two places, effectively preventing efficient operation near the desired 3.3-GHz SSD modulator frequency since each of these cavity modes would be excited by the drive power. The desired mode can be excited at the 3.0-GHz SSD modulator frequency since the resonance frequencies for these nearly degenerate modes are well separated by about 100 MHz. The highest-frequency mode most likely represents a first-order azimuthal mode of the cavity since it is relatively insensitive to cavity length until it approaches cutoff at the shortest cavity lengths investigated.

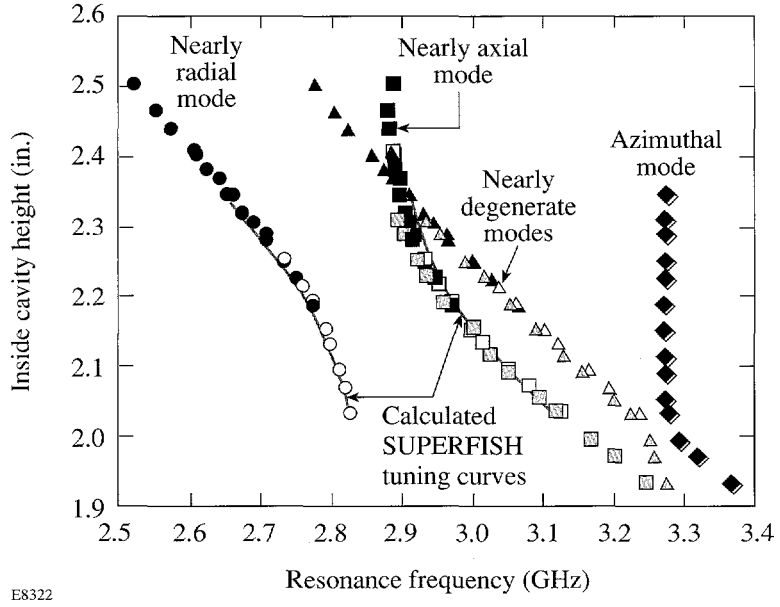

E8322

Figure 68.35
Measured and numerically simulated (*SUPERFISH*) tuning curves are plotted as a function of cavity length for large-aperture SSD #2 cavity.

Design Criteria

Numerous considerations impact the design and construction of SSD phase modulators, including laser-irradiation uniformity and OMEGA laser system damage considerations, as well as optical, electrical, and mechanical considerations. Each of these items is discussed in more detail below.

1. Uniformity and Laser System Considerations

The required SSD bandwidth is dictated by fusion target physics that have been addressed in previous SSD publications[16] and will not be treated in detail here. In general, large bandwidths are desirable, but laser system considerations, such as efficient frequency conversion to the third harmonic[17] and avoiding pinhole closure in the vacuum spatial filters, currently limit the useful bandwidth requirements to approximately 3 Å, given the current SSD grating dispersion.

Modulator frequency is determined by several irradiation uniformity issues. First, the microwave modulation period should be of the order of the effective smoothing time required to minimize imprinting of instantaneous laser speckle patterns on laser-fusion targets.[16] For two-dimensional SSD, a second constraint is that the modulator frequencies should be incommensurate (3.0 and 3.3 GHz) to maximize the number of individual lines within the SSD spectrum. Lastly, achievable phase-modulation amplitudes also impose a practical constraint on modulator frequency since the required SSD bandwidth is related to the modulation frequency by $\Delta\nu = 2\eta f_m$.

2. Optical Considerations

Lithium niobate ($LiNbO_3$) and potassium titanyl phosphate (KTP) are two commercially available electro-optic materials suitable for SSD modulators. Values for the relevant optical parameters of these materials are reported in Table 68.III. Both crystals possess large electro-optic coefficients suitable for transverse modulator geometries. KTP boasts higher r_{33} values and laser damage thresholds than $LiNbO_3$, but the electro-optic figure-of-merit in Eq. (12) is higher for $LiNbO_3$. All of the SSD modulators designed and built at LLE to date are based on $LiNbO_3$.

Damage threshold values reported in the literature vary quite widely depending on the purity and cleanliness of the material and antireflection coatings applied to the crystals. Most of these damage thresholds are reported for long pulses typically greater than 10 ns and must be scaled to the pulse lengths appropriate for laser-fusion experiments that are between 800 ps and several nanoseconds using an $I_{\text{damage}} \propto \sqrt{t_{\text{pulse}}}$ scaling law. Independent damage testing of $LiNbO_3$ at LLE has demonstrated damage thresholds greater than 1 GW/cm^2.

$LiNbO_3$ exhibits a photorefractive damage mechanism when exposed to visible and ultraviolet light. The scattering and absorption associated with this mechanism reduce the transmission of the crystal and may alter phase-modulation efficiency. To avoid this problem, room lights and flash lamps are blocked from the SSD modulators by windows made from

Table 68.III: Material parameters for $LiNbO_3$ and KTP.

	$LiNbO_3$	KTP
Electro-optic coefficient (pm/V)	r_{33} = 28.8–30.8 (at 633 nm)[18]	35.0
Index of refraction	n_3 = 2.1561 (extraordinary)	1.80
Relative dielectric constant	ε_{33} = 23.7–27.9[18]	15.4
$\frac{n_3^6 r_{33}^2}{\varepsilon_r}$ (pm/V) (using average values)	3304	2705
Laser damage threshold (1-ns pulse, λ = 1.06 μm)	1.2 GW/cm^2	>1 GW/cm^2

long-pass optical filter glass (RG-850), although two-photon absorption of intense infrared laser pulses may still pose a problem.[18] MgO-doped $LiNbO_3$ has been shown to prevent accumulation of photorefractive damage[19] and may be pursued for SSD modulators if this nonlinear mechanism proves active in the current design.

Electro-optic crystal dimensions are critically related to both the optical and microwave performance of SSD modulators. The cross-sectional area, or clear aperture of the modulator, is principally determined by laser-damage considerations. In OMEGA, SSD modulators are located in the driver line where 1- to 5-ns pulses with energies of approximately 10 to 100 mJ per pulse are typical. Designing for the worst case (1 ns, 100 μJ), a minimum beam diameter of approximately 110 μm corresponds to the damage threshold of 1 GW/cm^2. For conservatism, the actual beam diameter in the OMEGA driver line is set to approximately 400 μm. The minimum clear aperture of the crystal is chosen to be about five times larger than the beam diameter to account for misalignment and fabrication tolerances, as well as chamfers on the edges of the crystal to avoid breakage during grinding and polishing, which leads to a minimum clear aperture of 2 mm. A rectangular cross section (3 mm wide and 4 mm high) is used in SSD modulators currently in operation in OMEGA since experience learned over several years of developing and testing modulators empirically shows that square cross sections seem to lead to dielectric resonance modes that can interfere with the desired mode of a cavity.

Another factor that determines the cross-sectional size of the crystal in the second SSD modulator used in two-dimensional SSD is the bandwidth and dispersion impressed on the laser beam by the first stage of SSD. The restoration grating of the first SSD stage and the delay grating of the second SSD stage introduce 440 μrad/Å of dispersion in the horizontal and vertical directions, respectively. Since the second SSD modulator is located at the focal plane of a long-focal-length lens (f = 3062 mm), the beam sweeps through a distance of approximately ±2 mm at the second modulator when the first modulator operates at the design bandwidth of Δf_1 = 1.5 Å. Due to the two orthogonal gratings in series, the sweep of the focal spot is oriented at 45° with respect to the horizontal, as shown in Fig. 68.36. To account for this sweep, a new SSD #2 modulator is currently being developed with a clear aperture of 2 × 6 mm.

The maximum crystal length is determined by phase-mismatching between the laser and microwave fields in the

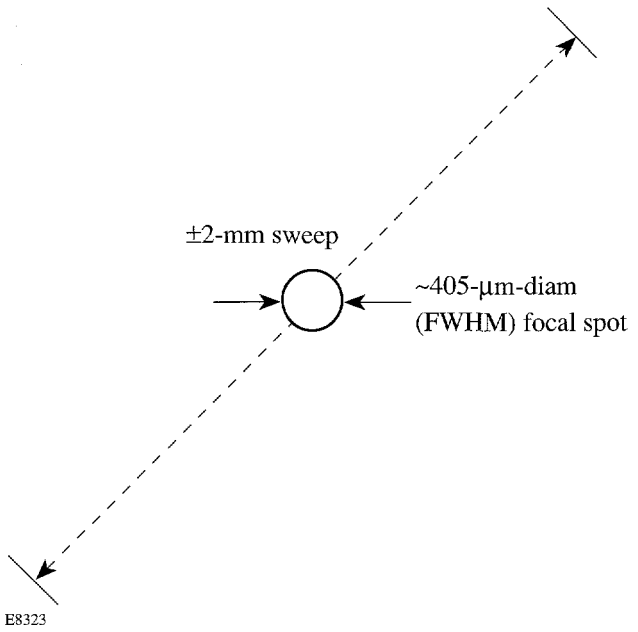

Figure 68.36
Clear-aperture requirements for SSD modulators are based on damage thresholds and beam sweep at focal plane of second SSD modulator in 2-D SSD.

$LiNbO_3$ crystal as determined by Eq. (3). The product of the phase-matching reduction factor and the $LiNbO_3$ crystal length β_L appearing in Eq. (2) is plotted in Fig. 68.37 versus crystal length for SSD modulators operating at both 3.0 and 3.3 GHz. The optimal length for these frequencies is observed to be approximately 10 and 9 mm, respectively. For simplicity, a 9-mm-long crystal is used in both the 3.0- and 3.3-GHz small-cavity modulators, while the 3.0-GHz large-cavity modulator uses an 11-mm-long crystal.

Another constraint is the maximum force that can be exerted on the crystal. Tests in interferometers and polarimeters show that the maximum allowable pressure on the crystal is about 750 g/cm^2 for $LiNbO_3$ before any noticeable changes take place in transmitted wavefront or residual retardance.

Proper crystal alignment with respect to the laser-beam polarization and propagation is critical since the tensor electro-optic properties of $LiNbO_3$ lead to a time-varying birefringence in the geometry used for SSD modulators that can generate amplitude modulation in polarization elements in the laser system. Proper alignment is also important in eliminating second-harmonic generation in the crystal since $LiNbO_3$ also possesses a strong $\chi^{(2)}$ coefficient. The laser polarization angle θ_y in the plane perpendicular to propagation, shown in

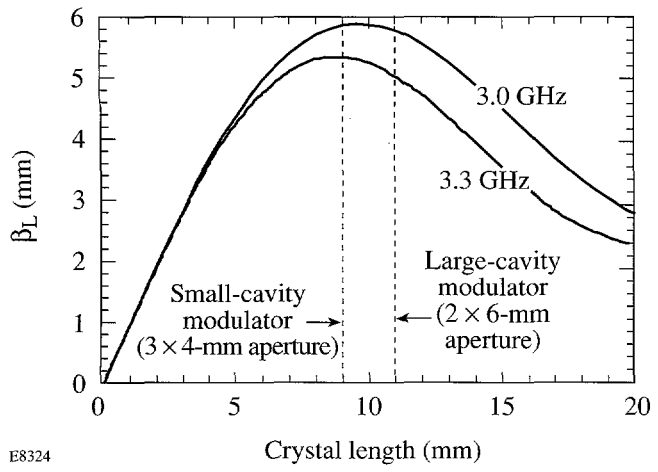

Figure 68.37
The product of the phase-matching reduction factor and the $LiNbO_3$ crystal length β_L appearing in Eq. (2) is plotted for both the 3.0- and 3.3-GHz SSD modulator frequencies. A maximum for these two frequencies appears between 9 and 10 mm. The small-cavity 3.0- and 3.3-GHz modulators utilize a 9-mm-long crystal, while the large-cavity 3.0-GHz modulator uses an 11-mm-long crystal.

Fig. 68.25, is easily controlled with a half-wave plate, while the pitch and yaw angles θ_x and θ_z, respectively, are controlled by mounting the modulator on goniometer stages with the center of rotation located at the center of the $LiNbO_3$ crystal.

3. Electrical Considerations

High-power, tunable microwave oscillators and transmission components are commercially available in the standard microwave bands of interest for SSD modulators listed in Table 68.IV. Surplus radar equipment is particularly attractive since high-power equipment is often available at reasonable prices. Given a cavity Q factor of approximately 1000, input powers of the order of several kilowatts are required to achieve the phase-modulation amplitudes required for SSD applications in inertial confinement fusion.

The coupling loop design is important for efficiently exciting the desired resonant cavity mode. To minimize the perturbation on the cavity mode caused by the coupling loop, its dimensions should be small compared to the microwave wavelength, which is approximately 10 cm at frequencies near 3 GHz. The loop is oriented perpendicular to the magnetic fields of the cavity to efficiently couple the microwave energy from the coaxial transmission line to the cavity mode. A low-resistance loop fabricated from gold-plated wire minimizes resistive losses.

Table 68.IV: U.S. military microwave bands.[20]

Microwave Band	Frequency (GHz)
S	1.550–3.900
X	6.200–10.900
K	10.900–36.000

The size of the coupling loop is determined empirically by approximately matching the complex impedance of the loop in the cavity to the characteristic impedance of the 50-Ω coaxial transmission line. Final impedance matching is accomplished using a standard double-stub tuner to minimize the power reflected from the modulator. Reflected power signals more than 30 dB below the incident power are easily achievable with careful coupling loop design and impedance matching.

The modulator cavity bodies are normally machined from solid stock to minimize the number of joints that would otherwise increase losses. The cavities built at LLE have usually been machined from high-purity copper in order to attain the highest conductivity possible. Several skin depths of gold are electroplated on the cavity to avoid oxidation of the surface that would increase conduction losses and reduce cavity performance. Gold-plated brass and silver-plated stainless steel have also been used. Machining tolerances are not stringent, but surface finish is very important. To minimize microwave losses, the surface finish must be an order of magnitude better than the skin depth. A skin depth of 1.5 μm is calculated from Eq. (15) at 3 GHz for gold, which indicates that sub-micron surface finishes are desirable. Single-point diamond machining of copper cavities followed by mechanical polishing yields a near-mirror finish.

Center posts are soldered to the covers, and numerous bolts are used to join this assembly to the resonator cavity body to insure a low-loss connection. An indium "o-ring" has also been employed in some modulators to ensure excellent electrical contact between the cover and the resonator cavity body. An adjustable, spring-loaded bellows is used to provide a controllable clamping force on the electro-optic crystal. A bellows is used, rather than a sliding joint, to maximize the conductance through the clamping assembly.

The most important electro-mechanical constraint in the cavity design is the electrical connection between the resonator and the electro-optic crystal. A low-loss connection is critical since very large microwave currents are delivered to the crystal. Gold-on-chromium electrodes are vapor deposited on the

$LiNbO_3$ crystal. A long-lasting, high-conductance contact to the crystal electrodes is accomplished using an gallium/indium alloy near the eutectic point for this material system (~85.8% Ga, 14.2% In) that has a liquid-solid transition temperature just above room temperature. After the cavity components, the crystal, and a crucible of the GaIn alloy are all heated above this temperature, the molten alloy is spread on the crystal electrodes and on the contact surfaces of the cavity. Great care is taken to ensure continuous coverage and complete wetting of the metallic surfaces. The modulator is assembled at this elevated temperature, and the spring pressure is adjusted to provide the correct clamping force on the crystal. Plastic alignment jigs are used to center the crystal in the cavity. The modulator is slowly returned to room temperature to allow the residual stress due to differential thermal contraction between the metal of the cavity and the $LiNbO_3$ to be taken up by the GaIn alloy. It can take several days for the alloy to completely harden, so mechanical shock must be avoided.

Arcing can occur between the modulator contacts at high microwave drive powers since strong electric fields can be developed in the modulator cavity. When this arcing limits the achievable bandwidth from the modulators, the cavities have been designed to operate in vacuum. Indium o-ring seals provide a good electrical contact between the cover and the body.

Testing

Modulator electrical performance can be accurately evaluated using a modern, vector network analyzer, such as the HP 8720B. The reflected power coefficient S_{11} for a modulator can be measured across a range of excitation frequencies and plotted in several convenient formats. Figure 68.38(a) shows S_{11} for a 3-GHz modulator. Optimizing the coupling loop dimensions and impedance matching minimize the reflected power at the resonance frequency. This corresponds to matching the resistive part of the modulator's complex impedance as close as possible to the 50-Ω coaxial line used to transmit drive power to the modulator, and minimizing the reactive part. The complex impedance $Z = R + jX$ of the modulator at the different excitation frequencies can also be represented in the format shown in Fig. 68.38(b). Careful coupling loop design can nearly achieve this condition, but final impedance matching is accomplished with a double-stub tuner.

The unloaded "Q" of the modulator can be estimated by

$$Q_{\text{unloaded}} \approx \frac{f_m}{\Delta f} = \frac{f_m}{f_2 - f_1}, \qquad (18)$$

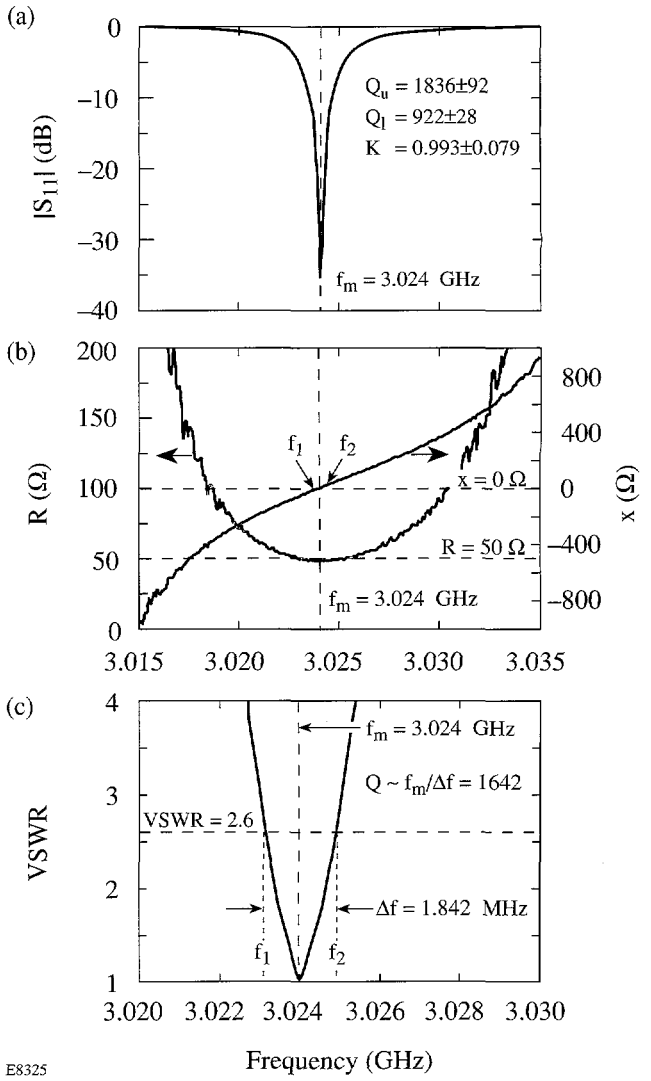

Figure 68.38
Electrical performance of large-cavity 2 × 6-mm aperture, 3.0-GHz modulator measured using the HP 8720B vector network analyzer. (a) The reflection coefficient $|S_{11}|$ plotted versus the excitation frequency demonstrates the narrow resonance of the modulator cavity. (b) The frequency difference between the points where the resistive and reactive parts have equal magnitude can be used in Eq. (18) to estimate the Q-factor of the resonant cavity. (c) The VSWR dependence on excitation frequency can also be analyzed to yield an estimate of the Q-factor by finding the frequency difference between the points where the VSWR is 2.6 times the value at f_m.

where f_m is the resonance frequency and Δf is the difference between the two frequencies that correspond to the point where the complex impedance is equally resistive and reactive. These two frequencies are denoted in Fig. 68.38(b) by points 1 and 2.

Another graphical approach using Eq. (18), which is equivalent to the method described above, estimates the unloaded Q of the modulator cavity using the voltage-standing-wave-ratio (VSWR) plotted versus excitation frequency, as shown in Fig. 68.38(c). In this method, the denominator in Eq. (18) is the difference between the two frequencies, f_1 and f_2, at which the VSWR is a factor of 2.6 times the value at f_m.

More exact values for Q_{unloaded} can be developed by numerically curve fitting Fig. 68.38(a) or 68.38(b) to the corresponding analytic expression using an algorithm such as implemented in the program QZERO.[21] QZERO also determines Q_{loaded}, the coupling coefficient K, and the uncertainty in each parameter, which are noted in Fig. 68.38(a).

High-power bench-top testing is useful to confirm proper coupling of the microwave drive power into the modulator cavity, as well as to identify potential low-resistance paths that might shunt power away from the electro-optic crystal, or "cat whiskers," formed by the GaIn solder that might cause premature arcing between the cavity electrodes.

Final optical testing is performed by passing prototypical laser pulses through the modulator to measure the bandwidth added by the modulators. A Fabry-Perot spectrometer is employed to measure the optical bandwidth of the laser pulse. Figure 68.39(a) shows the Fabry-Perot fringes captured by a video camera. Three fringes are observed that correspond to different transmission orders of the Fabry-Perot etalon. The width of each fringe corresponds to the optical bandwidth of the laser pulse, which can be calculated using the parameters of the etalon. Figure 68.39(b) depicts this optical bandwidth from which the full-width-at-half-maximum (FWHM) instrumental resolution is estimated to be approximately 0.2 Å.

Figure 68.40 presents the optical bandwidth measurements for the small-cavity 3.3-GHz modulator. Figure 68.40(a) shows the Fabry-Perot fringes that can be analyzed to yield the optical bandwidth shown in Fig. 68.40(b). For this modulator, 3.5 kW of microwave drive power yield approximately 1.49 Å of bandwidth. A convenient rule-of-thumb for estimating the SSD bandwidth in this experimental setup is given by the full width at 70% of the maximum, which very closely corresponds to the SSD bandwidth defined by $\Delta\lambda = \pm\eta f_m$. The dashed line in Fig. 68.40(b) represents the calculated Fabry-Perot spectrum for this estimated SSD bandwidth. Using this bandwidth measurement and the material properties in Table 68.III in Eqs. (2), (3), and (13) for this modulator, a value for the shunt impedance $R_s \approx 10\,\text{k}\Omega$ is calculated. Figure 68.41 shows the Fabry-Perot fringes and calculated spectra for the large-cavity 3.0-GHz SSD modulator.

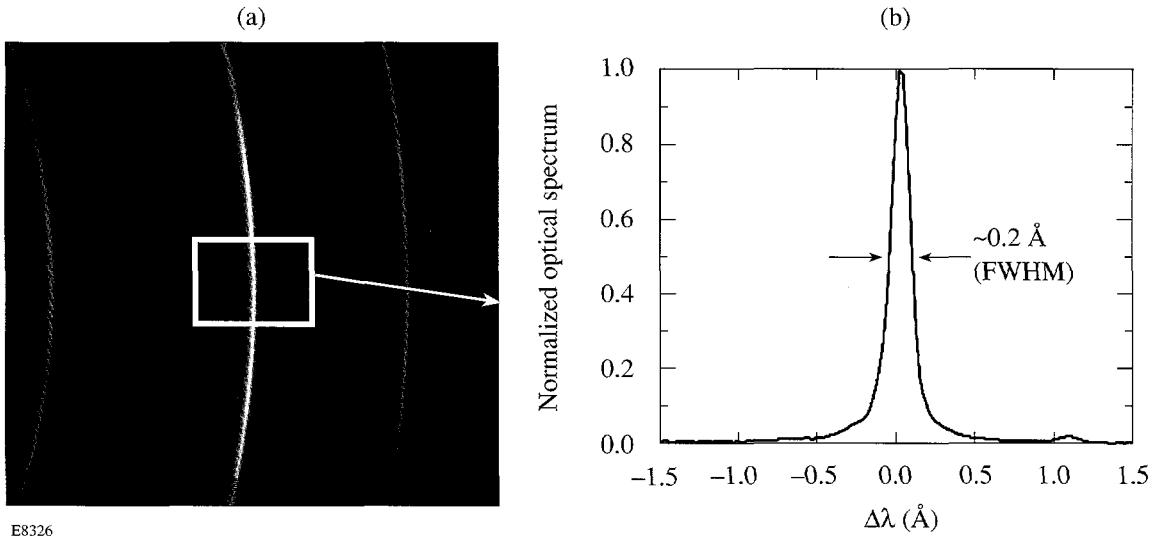

Figure 68.39
(a) Video image of Fabry-Perot fringes for laser pulse without SSD modulator energized. (b) Fabry-Perot fringes converted to a wavelength scale show that the instrumental response is approximately 0.2 Å.

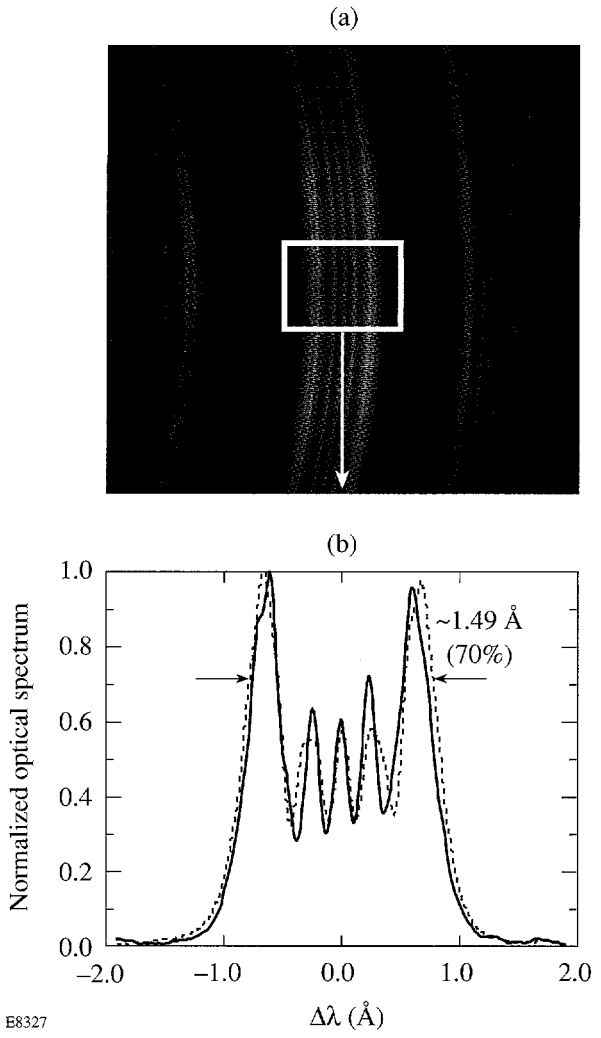

Figure 68.40
(a) Spectral measurements for the small-cavity 3.3-GHz SSD modulator depicted in Fig. 68.33 are made with a Fabry-Perot interferometer. The width of the fringes corresponds to the bandwidth of the laser beam, while the spacing between the fringes represents the free spectral range of the interferometer. (b) The Fabry-Perot fringes converted to a wavelength scale shows that approximately 1.49 Å of bandwidth was added to the laser beam with 3 kW of microwave drive power. The simulated spectrum for this phase modulation amplitude is shown as a dashed line.

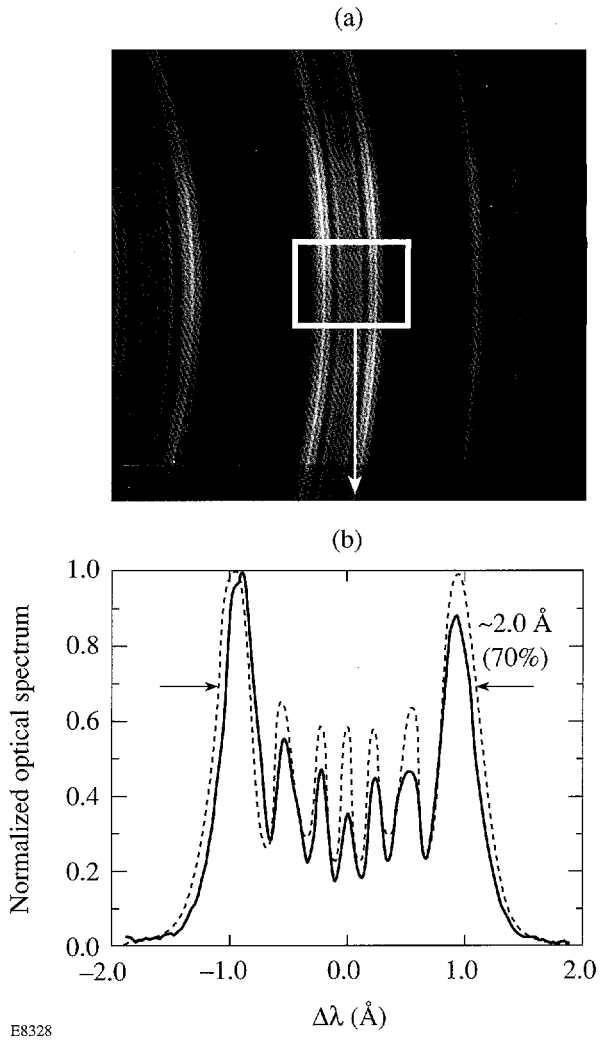

Figure 68.41
Pulsed Fabry-Perot spectra for large-aperture 3.0-GHz, large-cavity SSD modulator shown in Fig. 68.34. (a) Fabry-Perot interferometer fringes. (b) The Fabry-Perot fringes converted to a wavelength scale shows that approximately 2.0 Å of bandwidth was added to the laser beam with 5 kW of microwave drive power. The simulated spectrum for this level of phase modulation is shown as a dashed line.

Conclusions

Microwave phase modulators have been employed in various SSD configurations on OMEGA. The current modulator designs are $LiNbO_3$-based devices with microwave drive powers enhanced by resonant cavities. Large single-pass bandwidths are achieved in these modulators that provide substantial improvements in laser-irradiation uniformity.

Further improvements in uniformity are possible with higher-frequency SSD modulators that can generate significantly larger bandwidths. Advanced generations of modulator designs are presently under investigation, including multipass modulators, quasi-phase-matched modulator structures to compensate for the phase mismatching between the optical and microwave fields, and alternate electro-optic materials.

ACKNOWLEDGMENT

This work was supported by the U.S. Department of Energy Office of Inertial Confinement Fusion under Cooperative Agreement No. DE-FC03-92SF19460, the University of Rochester, and the New York State Energy Research and Development Authority. The support of DOE does not constitute an endorsement by DOE of the views expressed in this article.

REFERENCES

1. R. T. Denton, F. S. Chen, and A. A. Ballman, J. Appl. Phys. **38**, 1611 (1967).
2. M. A. Duguay and J. W. Hansen, IEEE J. Quantum Electron. **QE-4**, 477 (1968).
3. M. A. Duguay and J. W. Hansen, Appl. Phys. Lett. **14**, 14 (1969).
4. Laboratory for Laser Energetics LLE Review **37**, NTIS document No. DOE/DP/40200-83, 1988 (unpublished), p. 29.
5. Laboratory for Laser Energetics LLE Review **37**, NTIS document No. DOE/DP/40200-83, 1988 (unpublished), p. 40.
6. A. Yariv, *Quantum Electronics* (Wiley, New York, 1975), Sec. 14.4.
7. I. P. Kaminow and J. Liu, Proc. IEEE **51**, 132 (1963).
8. I. P. Kaminow and W. M. Sharpless, Appl. Opt. **6**, 351 (1967).
9. T. Moreno, *Microwave Transmission Design Data* (Dover Publications, New York, 1948).
10. H. J. Reich, J. G. Skalnik, P. F. Ordung, and H. L. Krauss, *Microwave Principles* (D. Van Nostrand Company, Princeton, NJ, 1957).
11. F. E. Gardiol, *Introduction to Microwaves* (Artech House, Dedham, MA, 1984).
12. G. J. Wheeler, *Introduction to Microwaves* (Prentice-Hall, Englewood Cliffs, NJ, 1963).
13. J. C. Slater, *Microwave Electronics* (D. Van Nostrand Company, New York, 1950).
14. J. D. Jackson, *Classical Electrodynamics*, 2nd ed. (Wiley, New York, 1975).
15. L. M. Young and J. H. Billen, computer code *SUPERFISH* (Los Alamos National Laboratory, Los Alamos, NM, 1996). (The *SUPERFISH* computer code is located on the Internet at http://www-laacg.atdiv.lanl.gov/c-on-line/descriptions/superfpc.html)
16. S. Skupsky, R. W. Short, T. Kessler, R. S. Craxton, S. Letzring, and J. M. Soures, J. Appl. Phys. **66**, 3456 (1989).
17. M. D. Skeldon, R. S. Craxton, T. J. Kessler, W. Seka, R. W. Short, S. Skupsky, and J. M. Soures, IEEE J. Quantum Electron. **28**, 1389 (1992).
18. R. S. Weis and T. K. Gaylord, Appl. Phys. A **37**, 191 (1985).
19. D. A. Bryan *et al.*, Opt. Eng. **24**, 138 (1985).
20. S. Y. Liao, *Microwave Devices and Circuits* (Prentice-Hall, Englewood Cliffs, NJ, 1980).
21. D. Kajfez, *Q Factor* (Vector Fields, Oxford, MS, 1994).

Design and Testing of a Large-Aperture, High-Gain, Brewster's-Angle, Zig-Zag Nd:Glass Slab Amplifier

The slab-geometry amplifier was invented in 1969 by Chernoch and Martin.[1] The advantages of the slab geometry have been enumerated by many authors[2] and will not be repeated here. A resurgence of interest occurred in 1982 as a result of work at Stanford University[3] on sources for remote sensing. Improvements in actual devices and theoretical understanding continued there[4,5] and elsewhere.[6,7]

The University of Rochester's Laboratory for Laser Energetics (LLE) began design and construction of a slab-geometry system specifically for use as a source for materials testing. This device incorporates, in one unit, many of the incremental improvements reported previously, including improved cooling, uniform pumping, high stored-energy density, simplified amplified spontaneous emission (ASE) suppression, and improved wavefront. One goal in the design was to avoid, wherever possible, the use of complex propagation codes, relying instead on careful design choices guided by physical insight obtained from analytic calculations and previous work. This article presents the resulting design and describes its measured performance.

The amplifier is made of Nd-doped LHG-5 phosphate laser glass[8] with physical dimensions of $31.0 \times 8.0 \times 1.1$ cm and a doping of 3.3 wt% Nd_2O_3. The ends of the slab are parallel cut at Brewster's angle. The clear aperture, defined as the unobstructed part of the aperture, is 1.0×6.6 cm and has a single-pass, small-signal gain of 8 and a 2-Hz maximum repetition rate.

Design

The amplifier is used in a facility where optical materials are tested for use in fusion-driver Nd lasers. The wavelengths of interest are the fundamental and the first two harmonics. The pulse widths of interest are 0.1- to 1.1-ns FWHM. The energy required is 4 J at 1 ns decreasing to ~1.3 J at 0.1 ns, limited by downstream optical coatings. The slab driver is capable of producing ~10 mJ of energy at 1 ns, thus requiring a slab-stage gain of ~400. The data acquisition in this facility requires the processing of images and is consequently limited to <2 Hz. The maximum design repetition rate of the slab was therefore set to 2 Hz.

1. Optical Design

The terminology for the various slab surfaces is shown in Fig. 68.42. In addition to these surfaces and the edges, three regions of the slab are referred to specifically. The side regions of the slab are the two pumped areas of the slab within one-half slab thickness of the sides, where propagation is disturbed by strain relief from the sides. The transition regions are the two areas of the slab near the ends, where a transition from pumped to unpumped glass is made. Finally, the central region of the slab is where the glass is uniformly pumped and the surface displacements are essentially uniform. Each of these regions is handled separately in the optical design to ensure wavefront quality.

High stored-energy densities are desirable in high-peak-power systems to avoid deleterious nonlinear effects such as self-focusing.[9] Typical thickness-averaged stored-energy densities (E_s) achieved in other large phosphate-glass, plate-geometry lasers were in the range of 0.3 to 0.33 J/cm^3.[10] These were achieved with single-sided pumping at a flash-lamp explosion fraction (f_x) of 0.34. Slab amplifiers can be double sided pumped with flash lamps derated to $f_x = 0.20$ for average-power handling. A simple scaling (ignoring ASE and thickness effects) suggested a stored-energy density near 0.50 J/cm^3. An E_s of 0.45 J/cm^3 was chosen as a conservative goal.

Over the pulse-width range of interest (~1 ns), the aperture required for one pass of the amplified beam—the beam clear aperture—is determined by the most-damage-threatened component after the slab. This is a graded-index[11] antireflection coating on the input lens to a spatial filter with a damage fluence approximated by[12]

$$\text{damage fluence}\left(\text{J/cm}^2\right) = 12\ \tau^{0.5}, \qquad (1)$$

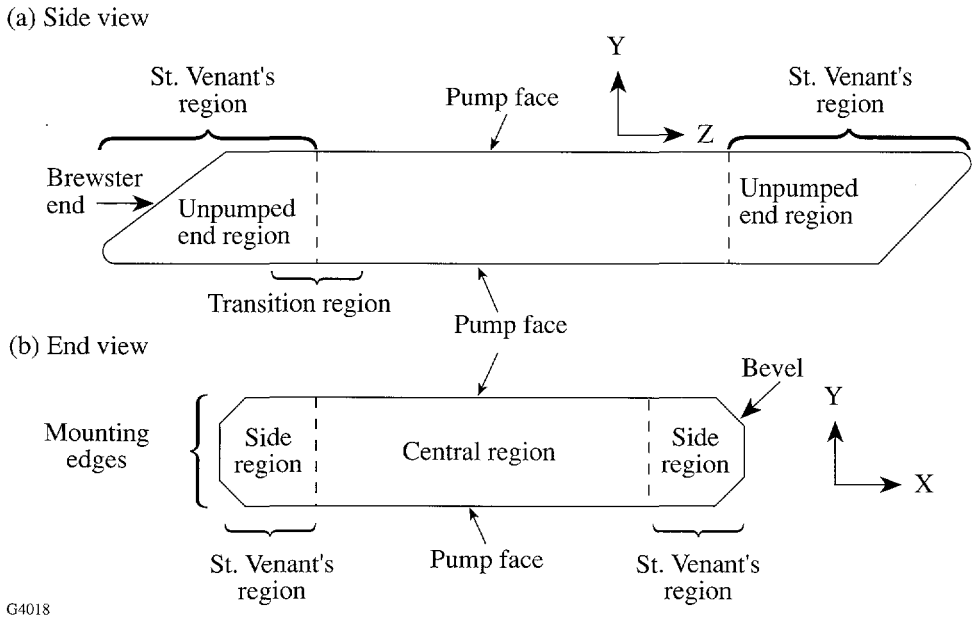

Figure 68.42
Orthogonal cross-sectional views of a face-pumped slab showing key features.

where τ is the pulse FWHM in nanoseconds. A TEM_{00} beam drives the slab with 1% intensity points assumed to be at the edge of the clear aperture. The on-axis fluence of this beam is six times the average fluence calculated by the energy divided by the clear aperture. A further safety factor of 1.8 is assumed[13] to allow for modulation (due to diffraction from surface scratches, etc.) on the beam. The beam clear aperture (C.A.) at the exit face is thus

$$\text{C.A.} = \frac{4\,\text{J} \times 6 \times 1.8}{\left(12\ \text{J/cm}^2\right)} \geq 3.6\ \text{cm}^2. \tag{2}$$

Since it is desirable to multiplex more than one pass through the slab, the *total* clear aperture is twice this or 6.5 cm^2.

Assuming a uniform[14] deposition of the pump light through the thickness (see Fig. 68.42) of the slab and equal cooling on both faces, the maximum stress σ_s in a slab of infinite extent occurs on the surface and is given by[4]

$$\sigma_s = \frac{Q}{12\ M_s} t^2, \tag{3}$$

where Q is the heat power per unit volume, t is the thickness, and M_s is the material figure of merit. The material figure of merit is defined as

$$M_s = \left[\frac{(1-\nu)k}{\alpha E}\right], \tag{4}$$

where ν is Poisson's ratio, α is the coefficient of linear expansion, k is the thermal conductivity, and E is Young's modulus. Because the size of defects at which fracture initiates is unknown, it is desirable to operate at some fraction b of the reported fracture stress σ_f for long slab life. Typical b values are ~0.2.[2] Equating and rearrangement yield

$$t^2 = \sigma_f M_s \frac{2.4}{Q}. \tag{5}$$

The quantity $\sigma_f M_s$ is known as the thermal shock parameter R_s of the material and is tabulated.[15] Q is given by

$$Q = E_s\, \chi f, \tag{6}$$

where f is the repetition rate and χ is the normalized heating parameter[16] defined as the ratio of heat energy to peak stored-energy density (E_s). Substituting and solving for t:

$$t = \left[R_s \frac{2.4}{E_s \chi f}\right]^{1/2}. \tag{7}$$

For a stored energy of 0.45 J/cm^3, an R_s = 1 W/cm,[15] and χ of 2.2,[16] the maximum slab thickness is 1.10 cm. The clear aperture in the thickness direction is slightly smaller to allow for the fact that the slab tip must be radiused slightly (~0.25 mm) to avoid damage during manufacture and handling. The actual clear aperture in this dimension is 0.92 cm. The extracting beam is therefore elliptical, with an aspect ratio (width to thickness) of 3.6:1.

The width of the clear aperture is 6.6 cm, and the physical width of the slab may now be calculated since the slab thickness is also known. The physical width of the slab must be wider by at least one slab thickness (one-half St. Venant's region at each side) to avoid the distorted major faces and depolarized region caused by stress relief[5] at the free sides. The physical width of this slab is 8.0 cm.

The pumped length of the slab is determined approximately by the gain requirement. Assuming a propagation angle θ of 20° (see Fig. 68.43), the z-direction length required for a small-signal gain of 8 is given by

$$L = \frac{\ln(8)\cos(\theta)}{\alpha_0 E_s} = 20.0 \text{ cm}, \tag{8}$$

where α_0 is the specific gain coefficient of the glass. The exact length of the pumped region is adjusted to align the pumped-to-unpumped transition regions to minimize wavefront errors across the narrow dimension of the beam. The physical length of the slab is longer than the pumped length to reduce stress-induced deformation of the entrance and exit ends of the slab. It is desirable to locate the center of each end at least one-half St. Venant's distance from the pumped region. The St. Venant's distance may be defined as the slab thickness (see Fig. 68.42), which is relevant for bending the end in the y-direction, or as the slab width that is relevant for bending the end in the x-direction. An additional 4 cm was added at each end.

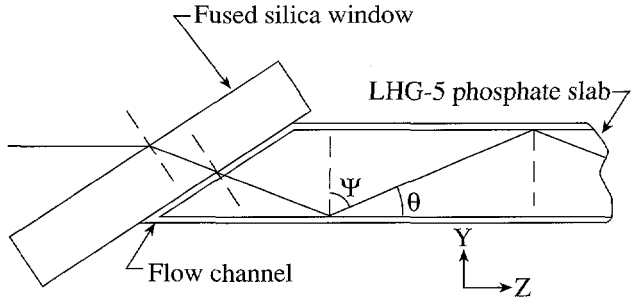

Figure 68.43
Entering or exiting ray for a Brewster's-angle slab with Brewster face cooling.

The exact physical length of the slab is set to ensure an even number of total-internal-reflection (TIR) bounces in the slab. To calculate the number of bounces N, the exact propagation angle θ must be known. The angle θ is the complement of Ψ, which was chosen for entrance to the slab near Brewster's angle for low loss and high internal fill. For this slab, Ψ = 66.91°, the slightly larger value chosen to allow for coolant mixtures with greater than 50% ethylene glycol (n = 1.424 at λ = 1054 nm)[17] and/or the future addition of evanescent-wave coatings.[18] The minimum slab length is the 20.0-cm pumped length plus both of the 4.0-cm runout regions at the ends. This corresponds to 10.85 bounces, so the next largest even number of bounces is chosen (12) for a slab length of 30.966 cm.

The entire slab, including the Brewster ends, is immersed in coolant. This strategy further reduces end-deformation effects on the beam. The optical power ϕ of the deformed end is proportional to

$$\phi = \frac{-c}{(n/n')}, \tag{9}$$

where c is the local curvature of the interface and n/n' is the ratio of the initial to final refractive indices. Immersing the end in coolant ($n_{1054\text{ nm}}$ = 1.375) reduces the optical power by a factor of the refractive index of the coolant. This strategy also eliminates the need for liquid seals to the slab, which must simultaneously withstand flash-lamp radiation, not distort the slab, and not leak. Enclosing the ends also protects them mechanically. Coolant flow over the entire unpumped region of the slab's faces maintains good thermal control in that region. Finally, it has been our experience that the liquid flow continuously cleans the Brewster ends, thereby removing the maximum damage threat from the expensive slab to the less-expensive entrance/exit windows. Figure 68.43 is a detail of the end treatment. The coolant thickness must be chosen to ensure sufficient flow to guarantee a complete coolant replacement between shots and simultaneously minimize absorption (α_c = 0.188 cm^{-1} at 1054 nm).[17] There is less than 1.64% absorption in the 1-mm coolant channel shown in Fig. 68.43.

The pumped length of the slab is adjusted to ensure that the ray-integrated optical path through both pumped-to-unpumped

transition regions does not vary with ray position in the extracting beam.[19] This ensures that piston-like phase defects along any ray sum to a constant value. The major concern here is OPD variation in the narrow dimension of the beam. These variations can arise from three sources: reflection from a displaced pump face, the variation of refractive index with stress (stress-optic effect), and the variation of refractive index with temperature. The last effect is of no concern since $dn/dT \sim 0.0$[20] for LHG-5 glass used here.

Displacements of the face over the area of the beam imprint occur in the transition regions from pumped-to-unpumped glass and may be calculated by integrating the strain field perpendicular to the pump face. The strain field is calculated from the thermal-source function $Q(x,y,z)$ using a finite-element code and the thermal boundary conditions. A Monte Carlo code[21] tracing ~1/2 million rays at 200 wavelengths from the flash lamps into the glass volume calculates the thermal source function. Temperature contours plotted within a longitudinal cross section of the slab are shown in Fig. 68.44. Not shown in Fig. 68.44 is the central region of the slab where the surface displacements are uniform across a beam footprint. The pumped length has been adjusted to 22.3 cm so that a ray at the entrance transition region TIRing from a portion of the face with a large displacement, TIR's from a portion of the face in the exit transition region that suffers only a small displacement. The length of the pumped region has been adjusted such that the sum of the pump face displacements sampled by the beam in the entrance and exit transition regions approximates a constant.

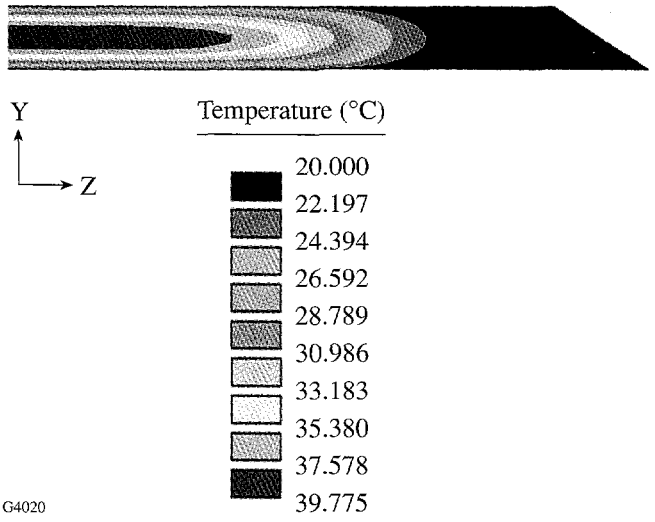

Figure 68.44
Longitudinal cross-sectional view showing the thermal distribution in the transition region.

The total change in pump face displacement over the length of a single beam footprint is minimized by making the transition region gradual. In this device the transition region is made less abrupt by locating the long-direction (end) reflectors well behind the electrodes of the flash lamps, thus rolling off the illumination in the z-direction before the slab goes under the end reflector.

The final aspect of the optical design is ensuring the uniformity of the central pumped region of the slab. Both the pumping and the cooling in this region must be as uniform as possible. The cooling is described in the following thermal design section. Early in the design, the transverse orientation [lamp axis parallel to width (x-axis shown in Fig. 68.42) of the slab] of the flash lamps was rejected because it could guarantee neither transverse nor longitudinal uniformity of pumping. Transverse uniformity requires that the lightly loaded (low-f_x) flash lamps be long compared to the width of the slab. To ensure adequate plasma opacity at the side of the slab, each electrode should be located at least two lamp diameters beyond the side of the slab. Any nonuniformities in the longitudinal direction due to the transverse lamps cannot be ameliorated by the compensation technique described previously because it is extremely unlikely that the lamp spacing for maximum uniformity will be the same as one bounce length.

Longitudinal orientation of the lamps guarantees z-direction uniformity as long as the arc fills the bore of the lamp and the aspect ratio (length to bore) of the lamps is sufficiently large. Filling the bore may be improved by prepulsing[22] the lamps. The reduced efficiency of emission from the lamp near the electrodes may be used to advantage to grade the pumped-to-unpumped transition region. The design goal reduces then to delivering sufficient energy, uniformly in the transverse direction.

The total stored energy in the slab at 0.45 J/cm^3 is 85 J. At a nominal storage efficiency (stored energy divided by energy stored in flash-lamp capacitors) of 1.5%, 5.7 kJ must be delivered to the flash lamps. A pump pulse width measured at 1/3 current max points of 350 μs is used, 25% longer than the ~280-μs fluorescent lifetime of the slab. At an explosion fraction f_x of 20% the minimum required arc length may be calculated from[23]

$$L = \frac{E_0}{17000\ f_x d(T/3)^{1/2}} = 80.25\ \text{cm}, \qquad (10)$$

where $d = 1.9$ cm is the lamp bore, E_0 is the energy delivered to the lamps, and T is the pump pulse width measured at the 1/3 current max points. The calculated total flash-lamp arc length required in this case is just under 32 in. Since flash lamps are conventionally ordered in integer inch lengths, the arc length was chosen to be 8 in. with two lamps pumping each side of the slab. One pulse-forming network drives a series-connected pair of lamps. Size-*E* ignitrons are used as switches instead of SCR's due to the high peak currents and large coulomb transfer.

Figure 68.45 shows a basic schematic of the pump cavity with all components listed. Within the pump cavity are several components that can be optimized for size, position, or type of reflective surface. To evaluate the uniformity of this cavity, the Monte Carlo ray-trace code ZAP[21] was used. Average *S*- and *P*-polarization properties were used. Measured or calculated reflection/refraction properties were assigned to surfaces in the cavity. Similarly, measured or calculated absorption/emission properties were assigned to volumes within the model. ZAP had been previously normalized to two other slab amplifiers. The approach to optimizing the pump geometry had two goals: (1) keep the cavity as simple as possible for fabrication reasons, and (2) keep the number of components in the cavity to a minimum. Reflector optimizations were performed for both a specular and a diffuse pump cavity. All simulations were time instantaneous at the peak of the flash-lamp pulse. Simulations done at other times during the flash-lamp pulse showed negligible change in the deposition profile. Reabsorption by the flash-lamp plasma was accounted for but none of the reabsorbed energy was reemitted. This was an excellent approximation because even at peak current density in the lamps, only 17% of the flash lamp's emitted light was reabsorbed.

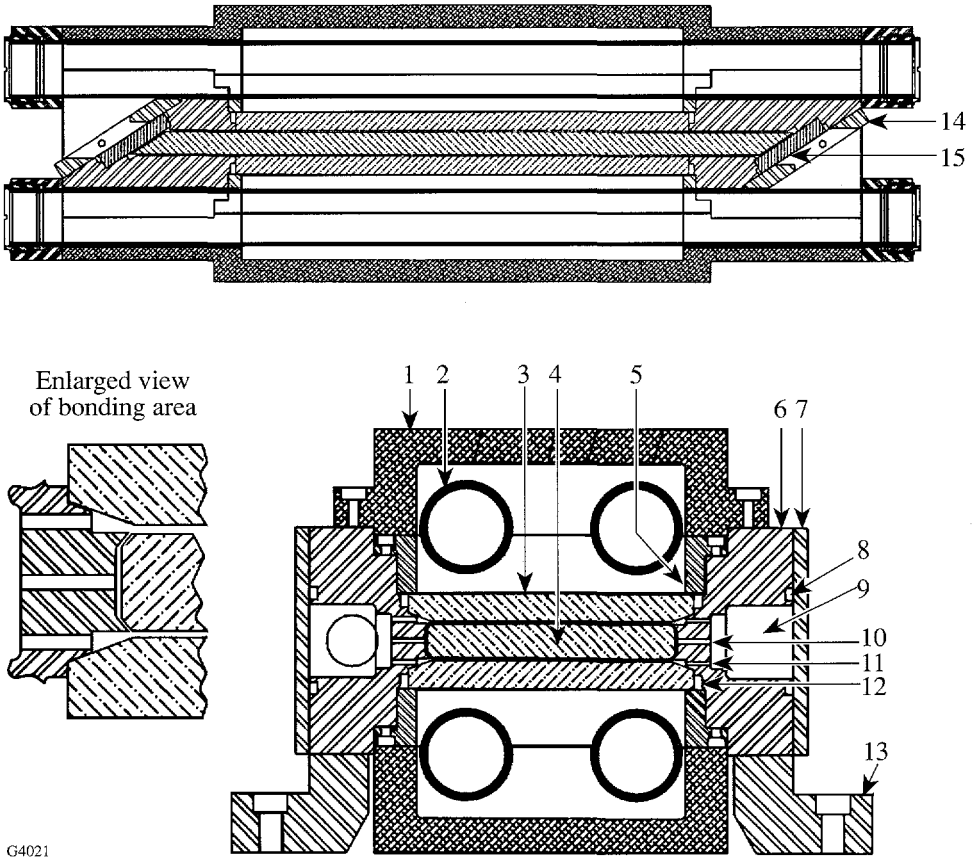

1. Reflector
2. Water jacket
3. Pump window
4. LHG-5 slab
5. Retainer
6. Frame
7. Side plate
8. Side plate o-ring groove
9. Plenum
10. Glue injection hole
11. Flow hole
12. Pump window o-ring groove
13. Support leg
14. Endcap
15. Brewster window

Figure 68.45
Orthogonal cross sections of the slab amplifier detailing all components.

After numerous simulations, some general statements regarding rectangular pump cavities could be made. The uniformity was fairly insensitive to changes in the shape of the pump cavity. In particular, angling the side of the reflector cavity up to 20° showed little or no improvement in uniformity or efficiency. Changing the roof of the cavity or adding a center reflector also showed little or no improvement in pump uniformity. The pump window retainer, however, showed substantial improvement in transfer and uniformity when specular and not diffuse. This is intuitively obvious since a diffuse surface would tend to send a fraction of the light back toward the lamps. Uniformity improvements were seen at the edges of the slab, which allowed the lamps to be moved toward the center of the slab.

The reflector materials were chosen simply on a cost basis. The specular reflectors are 6061-T6 aluminum polished to a 0.10-μm finish and then plated with 0.0127 to 0.0152 mm of electroless nickel. The nickel was then coated with *e*-beam-deposited silver. To prevent the silver from tarnishing, a silicon dioxide overcoat was applied.

Two sets of diffuse reflectors were designed: one metallic, the other ceramic. The metallic reflectors are the same as the specular except, instead of a polished surface, the surface is beadblasted with a fine bead size until all machining marks are removed. The reflectors are then plated in the same manner as the specular reflectors. The ceramic reflectors were fabricated from Macor®.[24,25]

2. Cooling

The cooling design of the slab requires uniform heat removal from the pump faces as well as tolerance to variations in the cooling-channel height. The temperature rise across the pump face is also minimized to reduce dn/dT effects across the aperture. With the pump volume, stored-energy density (E_s), and maximum repetition rate (f) known, the maximum average power loading P_a is given as

$$P_a = f V_p E_s \chi . \tag{11}$$

For steady-state conditions, all of the deposited thermal power is removed by the coolant. The thermal power deposited in the slab results in a temperature rise in the coolant. The energy balance equation can be written as

$$Q = \dot{m} c_p (T_o - T_i) , \tag{12}$$

where Q is deposited thermal power, $\dot{m}$ is the coolant mass flow rate, T_o is exiting coolant temperature, and T_i is the entering coolant temperature. A coolant temperature rise of 0.1°C is the design point. From this, the required mass-flow rate over the pump region is calculated as a function of power loading and ΔT. $\dot{m}$ is the minimum mass-flow rate required to remove the deposited heat from the slab. This mass-flow rate may be sufficient to remove the heat load; however, it may be insufficient to establish turbulent flow in the coolant channel. To maximize the heat-transfer capabilities of the coolant it is desirable to operate in the turbulent regime. If this condition exists, then the minimum mass-flow rate to establish turbulent flow is calculated.

The slab is completely submersed in coolant. For now, only the portion of the coolant channel in the pump regions is considered. To account for the total coolant requirements, simply multiply by the ratio of total slab perimeter divided by twice the pumped length. The coolant channels are 20.65 × 0.076 cm. The two coolant channels flow in parallel, which must be accounted for in all calculations. From Eq. (12), the minimum mass-flow rate $(\dot{m})$ is 1088 gm/s.

We now calculate the Reynolds number (Re) to verify that the flow rate is in the turbulent regime. Turbulent flow is typically achieved for $Re > 2300$ although laminar flow for $Re = 10^5$ has been demonstrated for special cases. The Reynolds number, which is the ratio of the inertia and viscous forces, is defined as

$$Re = \frac{\rho D u}{\mu} , \tag{13}$$

where ρ is the coolant density, u is the fluid flow velocity, D is the hydraulic diameter, and μ is the dynamic viscosity of the coolant.

The hydraulic diameter D for a square channel can be written as

$$D = \frac{4A_c}{P} , \tag{14}$$

where A_c is the cross-sectional area of the coolant channel and P is the wetted perimeter of the coolant channel, which is $P = 2(l_p + t)$.

The fluid flow velocity u is defined as

$$u = \frac{4V}{PD}. \tag{15}$$

Substituting Eqs. (14) and (15) into Eq. (13) yields an expression for the Reynolds number as a function of mass-flow rate and wetted perimeter P:

$$Re = \frac{4\dot{m}}{\mu P}. \tag{16}$$

Since half of the previously calculated mass flow goes to each coolant channel, $\dot{m}/2$ is used. Equation (16) yields a Reynolds number of 1400, which is clearly laminar. Solving Eq. (16) with Re = 2300 yields a minimum $\dot{m}$ = 1792 gm/s for turbulent flow.

The local convective film coefficient h in the coolant channel is required for thermal modeling of the slab. The film coefficient may be determined from the Nusselt number (Nu):

$$h = \frac{k\ Nu}{D}, \tag{17}$$

where k is the thermal conductivity. The Nusselt number may be calculated using empirically determined correlations. For this calculation, the Petukhov[26] correlation was used:

$$Nu = \frac{RePrc_f/2}{1.07 + 12.7\left(Pr^{2/3} - 1\right)\left(c_f/2\right)^{1/2}}, \tag{18}$$

where c_f is the friction coefficient and is empirically[26] determined to be

$$\frac{c_f}{2} = \left[2.236\ln(Re) - 4.639\right]^{-2}, \tag{19}$$

the Prandtl number Pr is defined to be

$$Pr = \frac{c_p\mu}{k}, \tag{20}$$

and c_p is the specific heat of the coolant.

The height of the coolant channel is an important parameter for a number of reasons. Since the channel height directly affects the hydraulic diameter, it also directly affects the flow velocity and the Reynolds and Nusselt numbers. The hydrodynamic entry length $x_{fd,h}$, which is the distance required to obtain a fully developed flow profile, is also affected. This is of importance since the convective film coefficient varies with the flow profile. Since no general expression for the entry length in turbulent flow exists, a first approximation is found using[27]

$$10 \le \frac{x_{fd,h}}{D} \le 60. \tag{21}$$

It can then be concluded that either the hydraulic diameter must be minimized or a suitable entry length must be designed into the amplifier.

The effect of the channel height on the flow velocity can be readily seen in Eqs. (14) and (15). The net effect is simply an increase in the flow velocity with decreasing height. This may not seem to have any significant impact on the cooling dynamics of the amplifier; however, there is a significant impact in the area of pressure drops Δp. This is readily seen from

$$\Delta p = f\left(\frac{L}{D}\right)\frac{1}{2}\rho u^2, \tag{22}$$

where the pressure drop is proportional to the flow velocity squared, f is the friction factor, and L is the distance traversed. Pressure drops will be discussed later.

The effects on the Reynolds number are negligible at best. Since the coolant channel has a high aspect ratio $l_p >> t$, the effects of the channel height are negligible. From this, it is also obvious that the Reynolds number is also insensitive to variations of the channel height. From this and Eq. (14), it is shown that the effects on the Nusselt number are also negligible.

From Eq. (17), the importance of reducing the hydraulic diameter to increase the convective film coefficient is established. It is desirable to have a low hydraulic diameter; however, we are bounded by the pressure required to move the coolant through the channel. Equation (22) can be reduced to

$$\Delta p = \frac{f}{4} L\rho V^2 \frac{\left(l_p + t\right)}{\left(l_p t\right)^3}, \tag{23}$$

which shows the pressure dependence on the channel height where V is the volumetric flow rate. Equation (23) neglects any effects on the friction coefficient because it was previously stated that the effects on the Reynolds number were

negligible. The friction factor is defined in Table 68.V for various Reynolds numbers.

As a design goal we wanted to keep the pressure drop of the amplifier below 5 psi to prevent pressure-induced deformation of the input and output Brewster windows.

3. Linear Optical Effects in the Coolant Channel

In propagating through the coolant channel, dn/dT effects can cause significant wavefront errors. As a design point, we chose to keep this error less than $\lambda/10$. This error can be directly controlled by varying the propagation distance through the coolant channel. For a first-order approximation of the wavefront error, we assume instantaneous and uniform heating through the coolant channel. Assuming a peak fluence F_p of 10 J/cm^2 over a unit area of 1 cm^2 and using the linear absorption coefficient α of ethylene glycol and water, we calculate a temperature rise of 0.52°C using

$$\Delta T = \frac{Q}{mc_p}, \tag{24}$$

where $Q = a_c F_p$.

From this the optical-path-length difference is found using

$$\Delta d = \frac{dn}{dt}\,\Delta T d, \tag{25}$$

where d is the path length through the coolant channel. The value dn/dT was the average of water (-1.2×10^{-6}/°C)[17] and ethylene glycol (-2.7×10^{-6}/°C).[17] The resultant path-length difference was $\lambda/12$ at 1054 nm.

4. Nonlinear Optical Effects in the Coolant Channel

High-peak-power laser systems can be limited by a variety of nonlinear effects. The limitations imposed by these effects, which include self-focusing and stimulated scattering, are well understood for conventional materials such as fused silica and laser glass.[28] In this slab design, the high-peak-power beam propagates through the thin (0.088 cm, corrected for Brewster's angle) cooling channel's 50%/50% (by volume) mixture of flowing ethylene glycol and water.

The thinness of the channel (0.088 cm) would require a nonlinear index of the coolant to be two orders of magnitude greater than that of typical solids before self-focusing would be a problem, which is not likely. Similarly, the thinness reduces the gain-length product for forward and backward stimulated scattering to very small values. However, transverse stimulated scattering could experience significant gains. Since Raman gain coefficients are typically an order of magnitude lower than those for stimulated Brillioun scattering (SBS), the case of SBS is examined.

The Brillouin gain can be characterized as transient or steady state, depending on how the pump pulse compares to the phonon lifetime. Transient gains are much lower than steady-state gains. The steady-state case will be examined first. The steady-state gain coefficient at 1064 nm for backward SBS in pure water is measured to be 3.8 cm/GW.[29] Correcting the gain coefficient by $\cos(\pi/4)$ to the transverse scattering gain yields a transverse SBS gain coefficient at 1064 nm of 2.7 cm/GW. The maximum output-beam intensity is taken to be 4 GW/cm^2 external to the amplifier. In the amplifier the intensity is reduced by the factor of the refractive index due to the Brewster's angle input. Accounting for the average 1.38 refractive index of the cooling mixture, the pump intensity I_p is 2.8 GW/cm^2. Assuming a perfectly spatially flat output profile, the maximum transverse dimension L is then equal to the maximum width of the beam or 3.6 cm. The gI_pL product is then

$$gI_pL = 27. \tag{26}$$

A gI_pL product of 30 or more is generally accepted as being required for significant Stokes wave growth from noise. Note that this is a very conservative estimate because the pulse widths of interest here (~ few nanoseconds) are of the same order as the phonon lifetime for water, placing this problem clearly in the transient regime, where the SBS gains are much lower.

Table 68.V: The friction factor for various Reynolds numbers.

$f = \frac{64}{Re}$		Fully developed laminar flow
$f = 0.316\,Re^{-0.25}$; $Re < 2 \times 10^4$	}	Fully developed turbulent flow
$f = 0.184\,Re^{-0.25}$; $Re > 2 \times 10^4$		

Since the coolant is a mixture of ethylene glycol and water, the case of pure ethylene glycol is examined next. The measured transverse SBS gain coefficient for ethylene glycol at 532 nm is 0.60 cm/GW.[30] The measured transverse SBS gain coefficient for water at 532 nm is 2.1 cm/GW.[31] The gain coefficients for ethylene glycol at 532 nm is therefore ~0.3 that of water and, assuming similar wavelength scalings to 1054 nm, will be no worse a threat than SBS from water.

5. Mounting

The slab was mounted in the configuration shown in Fig. 68.45, which is a departure from the square edge used in numerous experimental test beds.[10,32] This geometry has mechanical, thermal, and optical advantages that combined provide significant performance improvements. The edges of the slab are pitch polished to an inspection finish with the glass and metal bonded by an air-cured silicone adhesive.[33]

The philosophy of the mounting configuration is to ensure minimum risk to the slab, should a debond in the silicone bonding layer occur. If a debonding in the silicon layer were to occur, the slab could move only in the z-direction. This configuration also removes the bulk of the adhesive from direct pump-light radiation.

The thermal benefits of the beveled slab are quite significant. The finite element program ANSYS[34] was used to solve both the thermal and stress distributions in the slab. Figure 68.46 shows the temperature distribution of a uniformly loaded, square-edged slab with the edge of the slab as a perfect insulator. As one would expect, the temperature distribution is uniform. Figure 68.47 shows a slab with bevels added. Notice the isotherms turn up so that they terminate normal to the slab boundary, once again as expected. This implies that a perfect insulator is not required at the slab boundary. Figure 68.48 shows the uniformly loaded slab with the silicon adhesive and metal frame added. Notice the change in the isotherms due to conduction at the edge. Figure 68.49 shows the resultant temperature distribution when the slab is loaded with the pump profile predicted by ZAP. As can be seen in Fig. 68.49, the thermal gradients occur in less than the St. Venant's region (one slab thickness).

Experimental

1. Gain and Gain Uniformity

Small-signal-gain experiments were performed in the center of the clear aperture using the ratio-of-ratios technique. This technique accounts for transmission losses; therefore, the gain values are gross gain. Figure 68.50 shows the con-

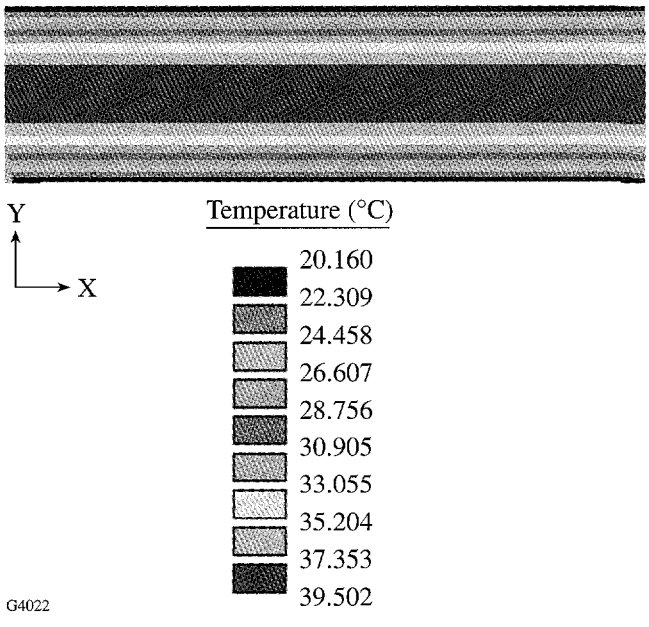

Figure 68.46
Steady-state isotherm plot of a uniformly loaded slab with square edges. The edges are treated as an adiabatic boundary.

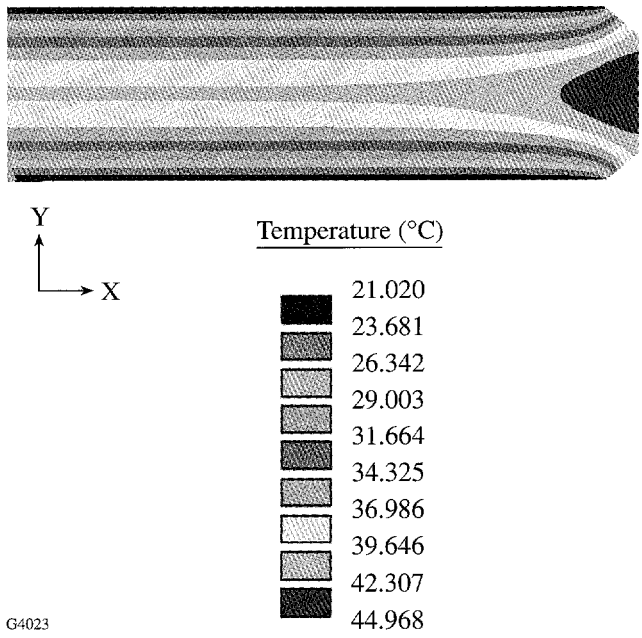

Figure 68.47
Steady-state isotherm plot of a uniformly loaded slab with beveled edges. The edges are treated as an adiabatic boundary.

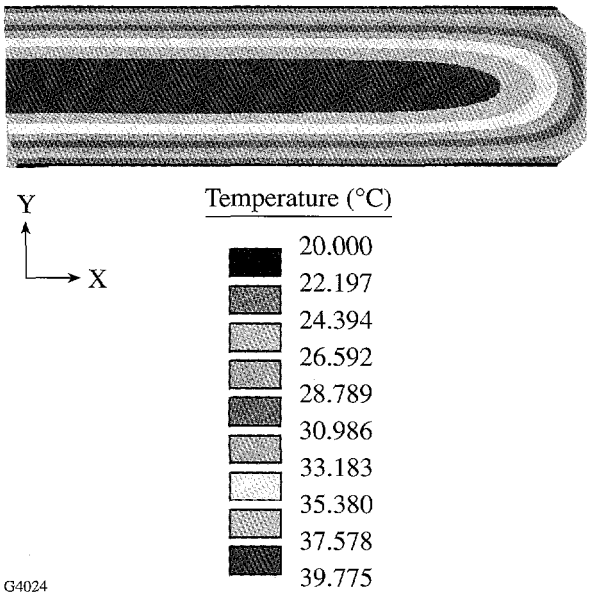

Figure 68.48
Steady-state isotherm plot of a uniformly loaded slab with beveled edges. The silicon bonding layer and stainless steel frame have been added as detailed in Fig. 68.43.

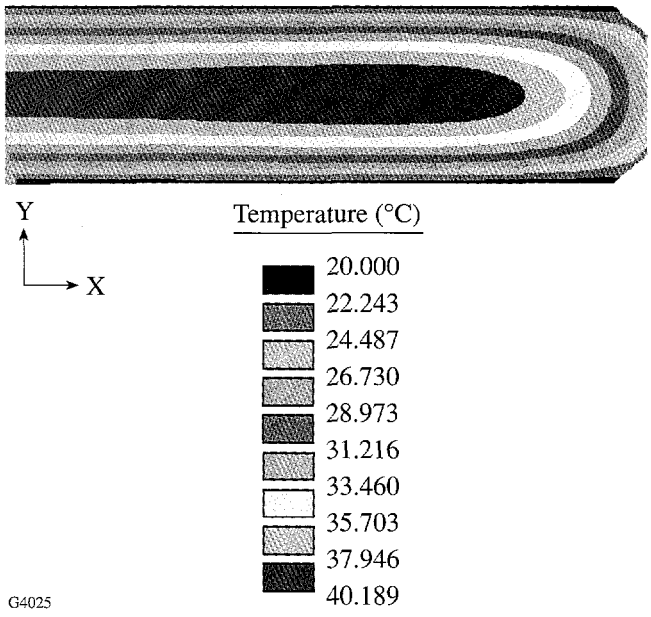

Figure 68.49
Steady-state isotherm plot of a slab loaded with a predicted pump profile. The silicon bonding layer and stainless steel frame have been added as detailed in Fig. 68.43.

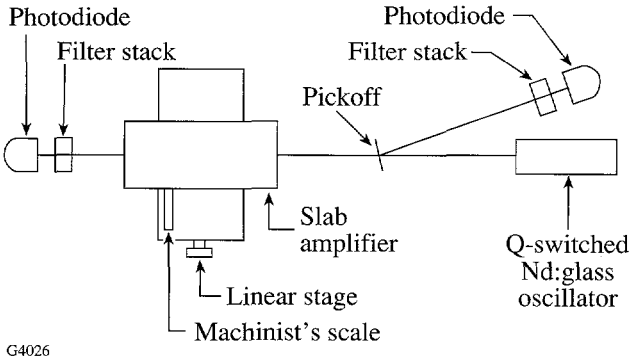

Figure 68.50
Experimental setup used for small-signal-gain and gain-mapping experiments.

figuration of the gain setup. The probe oscillator is a Q-switched Nd:glass oscillator that produces 100-ns FWHM pulses at 1054 nm. The reference and gain signals are detected using large-area photodiodes[35] to ensure that the entire probe beam is detected. Three sets of gain data were obtained, each of which corresponds to a different reflector type. The reflector types will be denoted as specular, metal diffuse, and ceramic diffuse.

The initial data runs were done as a function of bank energy. This data is shown in Fig. 68.51 for the two reflector types. As can be seen from the data, there is no parasitic clamping or ASE roll-off. Also from Fig. 68.51, it is observed that there is no performance penalty for using diffuse reflectors. The storage efficiency is plotted in Fig. 68.52 as a function of stored energy in the slab. This clearly shows characteristic roll-off in efficiency with increasing stored energy.

Mounting the amplifier on a linear stage allows gain mapping across the aperture. For all reflector types, the gain map was obtained with the probe beam (2-mm diameter) centered vertically in the clear aperture. Data points were obtained every 0.1 in. across the physical aperture. For the specular reflectors, the gain mapping was performed at three different bank energies. The three bank energies cover the anticipated operating range of the amplifier. Figure 68.53 shows the resultant normalized data compared to a predicted pumping profile. From Fig. 68.53, a pump uniformity of ±6% is observed. Two conclusions can be drawn from this data: (1) the pump profile was independent of the 4- to 7-kJ bank-energy range, and (2) agreement between predicted and experimental values was within the error bars of the code.

Normalized data for the diffuse reflectors is shown in Fig. 68.54 along with the corresponding predicted profile. Data for the diffuse reflectors was obtained at only the bank energy for which the slab was designed. The data was normalized to

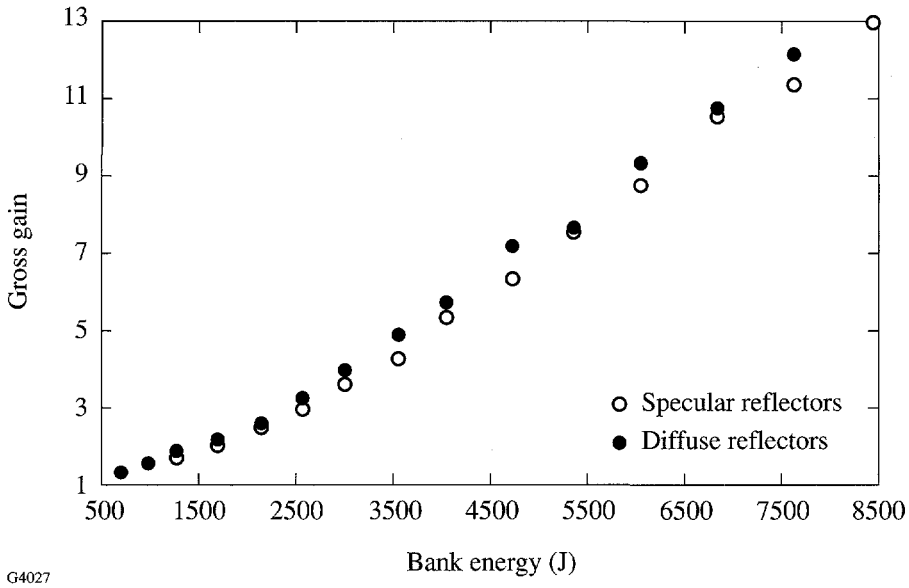

Figure 68.51
Plot of gross gain as a function of bank energy for both specular and diffuse reflectors.

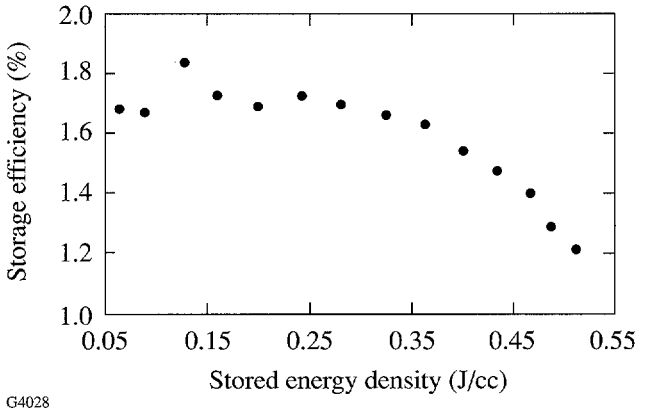

Figure 68.52
Storage efficiency as a function of stored energy in the slab.

the average stored energy across the slab aperture. There is virtually no difference between the two sets of reflectors. From Fig. 68.54, a pump uniformity of ±3% is observed. This is important since it gives us a method of producing inexpensive and effective reflectors.

2. Birefringence Mapping

Birefringence maps for all reflector types were obtained using the setup shown in Fig. 68.55. The laser source was a diode-pumped Nd:YAG.[36] Due to the stability of the laser, no reference signal was needed. The polarizer analyzer pair was chosen such that a contrast ratio of 2500:1 could be obtained. The intensity of the probe laser was then measured with the polarizers both crossed and uncrossed. For data with uncrossed polarizers, a set of calibrated optical density filters[37] were

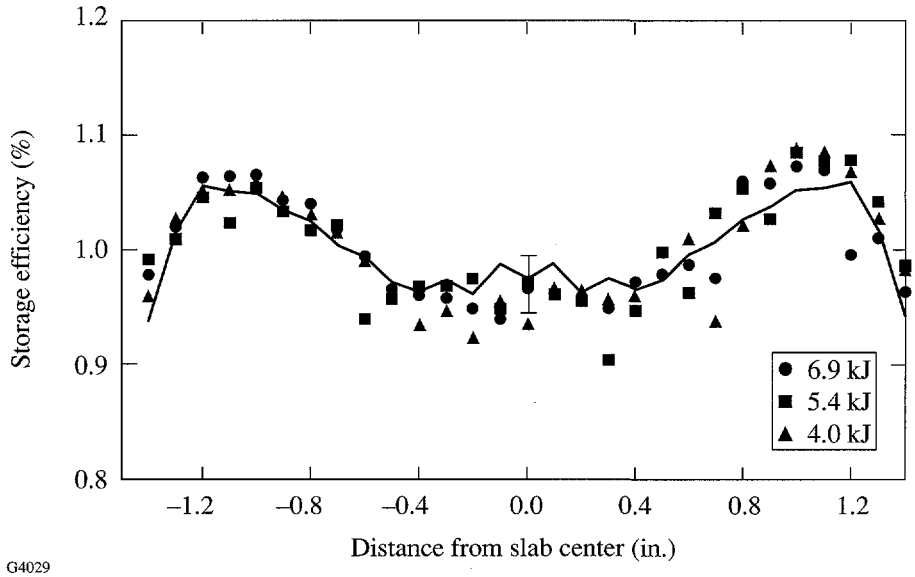

Figure 68.53
Normalized-stored-energy map for specular reflectors at three discrete bank energies. Also shown is the predicted pump profile with 3σ error bars.

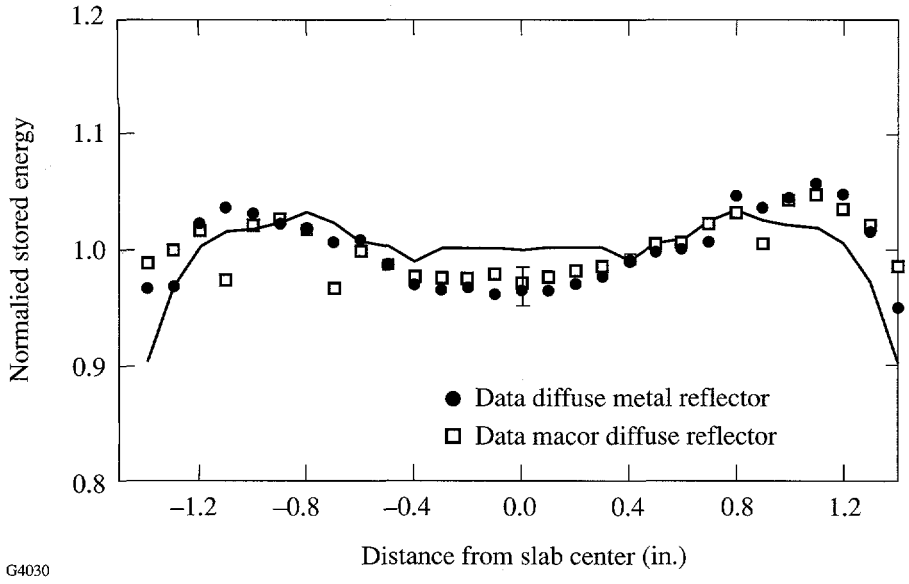

Figure 68.54
Normalized-stored-energy map for two different diffuse reflectors at the design bank energy. Also shown is the predicted pump profile with 3σ error bars.

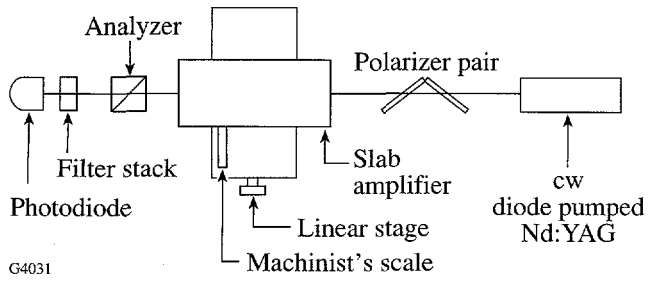

Figure 68.55
Experimental setup used for birefringence mapping.

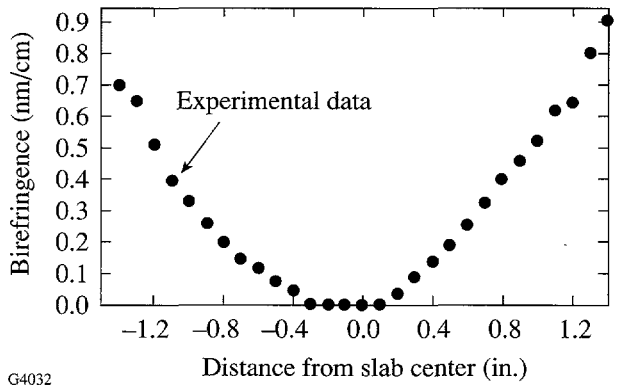

Figure 68.56
Steady-state birefringence map.

used to keep the signal on the diode below 1 V. This was done to maintain operation of the diode well within the linear range. Measurements with the polarizer analyzer pair crossed and uncrossed were obtained at 0.1-in. increments across the physical aperture.

The first depolarization data was obtained with the amplifier unpumped to measure any residual stress depolarization due to mounting and the glass itself. The remaining data was taken at 1 Hz at the designed bank energy. Figure 68.56 shows depolarization as a function of aperture for both reflector types.

3. Wavefront Evaluation

The wavefront of the slab was evaluated with the amplifier in one leg of a Mach-Zehnder interferometer (Fig. 68.57). The interferometric data was evaluated using spatial synchronous phase detection (SSPD).[38] This technique was developed by Takeda *et al.* with acquisition and analysis developed at LLE.[39] The probe source was a 1064-nm, Q-switched, cw source. The amplifier was run at 1 Hz at the design bank energy with the diffuse reflectors for at least 1 min prior to data acquisition to ensure that steady state had been achieved. This was verified to be a sufficient length of time by acquiring a second interferogram after 5 min of operation. Since we are interested in the steady-state effects and not the transient effects, data was collected between amplifier shots. Three sets of interferometric data were taken. The initial data was taken with the amplifier static; this served as the reference wavefront for which all subsequent data will be used. Next the coolant was turned on, which allowed us to measure directly the pressure-induced deformation of the Brewster windows. Finally the slab was pumped, which allowed us to measure the thermally induced wavefront deformation.

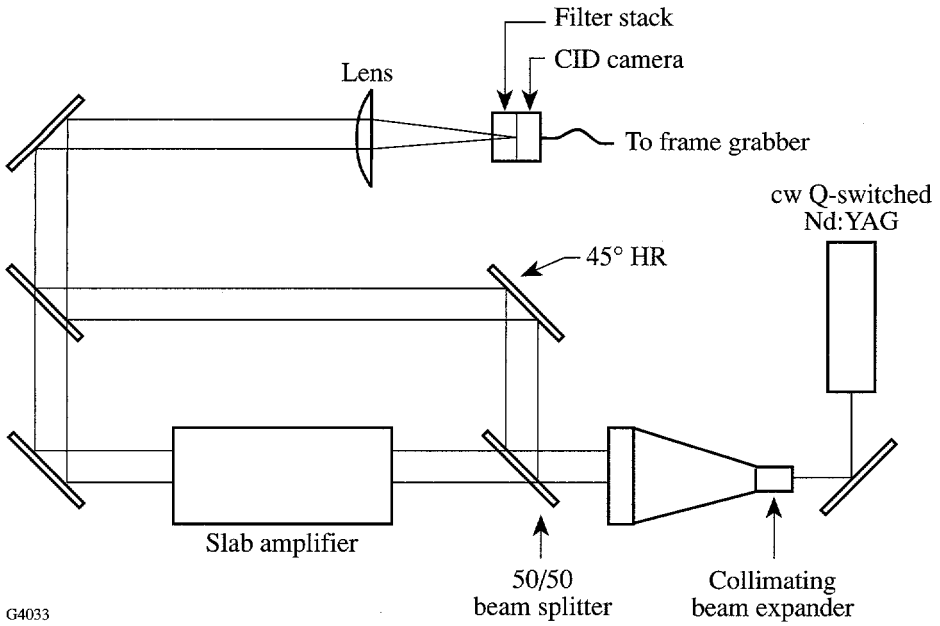

Figure 68.57
Mach-Zehnder interferometer setup for wavefront evaluation.

Figure 68.58 shows the pressure-induced wavefront with the static wavefront subtracted out. This compares with the previously predicted error. This effect can be reduced by (1) increasing the thickness of the Brewster windows, and (2) reducing the internal pressure in the slab by increasing the size of the coolant return lines.

Figure 68.59 shows the thermally induced wavefront error with the pressure-induced wavefront error subtracted out. Due to the very high fringe frequency at the edges of the physical aperture, data could not be extracted; however, data within the clear aperture was undisturbed. This effect is directly attributed to SSPD, which is primarily used for high-resolution

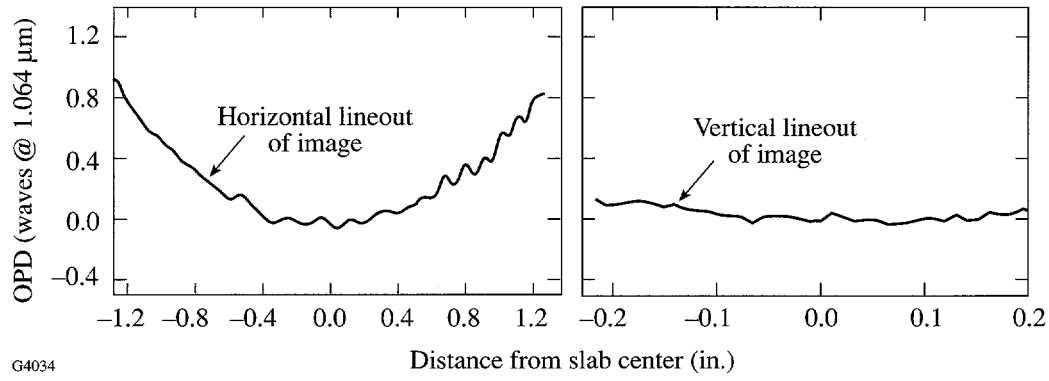

Figure 68.58
Pressure-induced wavefront error within the clear aperture.

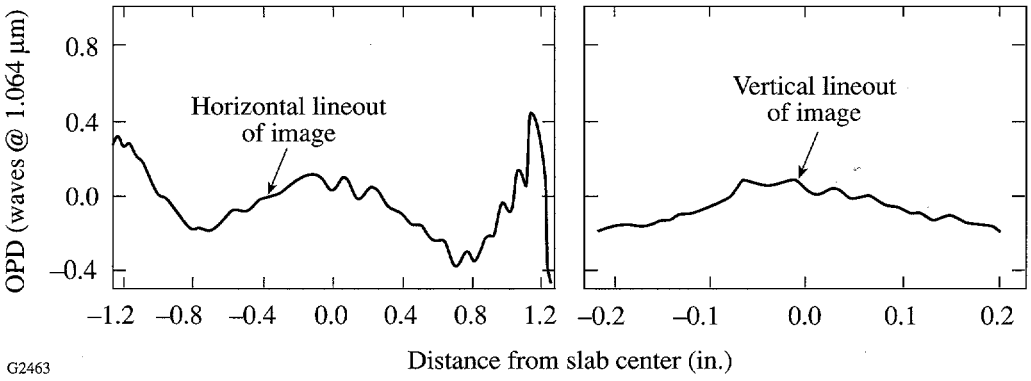

Figure 68.59
Thermally induced wavefront error within the clear aperture.

(λ/400) and is not well suited for multiple waves of deformation. The wavefront error bears a strong resemblance to the pumping profile, and it is natural to ask how much of the wavefront error is due to deformations of the pump faces of the slab. Using the measured pump profile, ANSYS was rerun to determine if indeed there is a connection.

4. System Performance

The slab was installed in LLE's damage test laser (DTL) (Fig. 68.60). This system has been used for materials testing and nonlinear optics experiments. The front end of the system consists of a 3-m, Q-switched, mode-locked Nd:phosphate glass oscillator running between 0.1 and 1.1 ns. Nominal operation of the system is at 0.8 ns. A single, 1-mJ pulse is amplified by a 1/4-in. × 6-in. Nd:glass rod capable of delivering up to 100 mJ of drive to the slab. The beam undergoes one-dimensional expansion in a Littrow prism anamorphic beam expander. The beam then passes through a 2× Galilean telescope before being injected into the slab. The pulse is then amplified with three passes through the slab. The output pulse is then spatially filtered before being converted to 527 nm or 351 nm. The frequency-conversion cell consists of KD*P, set up in a Type-II polarization mismatch scheme.[40]

Conversion-efficiency measurements were performed at the second and third harmonics. The results are shown in Table 68.VI; note that the peak conversion efficiency may not coincide with the peak energy due to conversion crystals of less than optimum thickness. The high conversion efficiency will allow for large-area materials testing at 351 nm.

Table 68.VI: System Performance

Wavelength	Conversion Efficiency	Energy
1054 nm	--	2.1 J
532 nm	68%	1.4 J
351 nm	55%	0.88 J

Summary

We successfully designed, constructed, and tested a large-aperture, high-gain, Nd:glass slab amplifier with a 2-Hz repetition rate. The slab was designed for a gross small-signal, single-pass gain of 8, although a maximum gross small-signal gain of 13 was obtained. These stored-energy densities were obtained without special ASE (amplified spontaneous emission) suppressors and with a pump uniformity of ±3%. This pump uniformity was achieved with a simple box reflector with diffusely reflecting surfaces. Two methods of producing this diffuse surface were found to give comparable pump profiles. This high degree of pump uniformity helped to minimize thermally induced wavefront errors that were less than 0.5 waves at 1054 nm in the clear aperture.

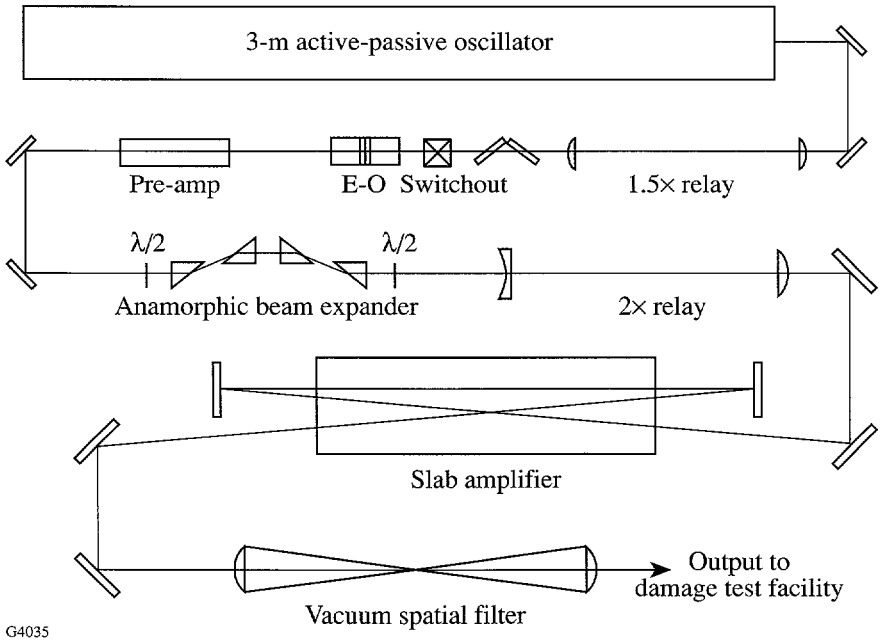

Figure 68.60
Damage test laser schematic.

When installed in LLE's damage test laser, the slab amplifier brought the system performance to the multijoule level with as little as 10 mJ of drive. This system has sufficient beam quality to permit high conversion efficiencies at the second and third harmonics.

ACKNOWLEDGMENT

The authors wish to thank the tool makers at JASCO Precision for the excellent fabrication of this amplifier. Thanks also to Steve Swales of LLE's Wavefront Analysis Laboratory for reducing the interferometric data. This work was supported by the U.S. Department of Energy Office of Inertial Confinement Fusion under Cooperative Agreement No. DE-FC03-92SF19460, the University of Rochester, and the New York State Energy Research and Development Authority. The support of DOE does not constitute an endorsement by DOE of the views expressed in this article.

REFERENCES

1. J. P. Chernoch and S. W. Martin, U. S. Patent No. 3,633,126 (17 April 1969).
2. R. L. Byer, presented at the International Lasers and Electro-Optic Exhibition, Tokyo, Japan, 26 January 1985.
3. R. L. Byer, Lawrence Livermore National Laboratory Report UCRL-15561 (1982).
4. J. M. Eggleston *et al.*, IEEE J. Quantum Electron. **QE-20**, 289 (1984).
5. T. J. Kane, J. M. Eggleston, and R. L. Byer, IEEE J. Quantum Electron. **QE-21**, 1195 (1985).
6. J. M. Eggleston *et al.*, IEEE J. Quantum Electron. **22**, 2092 (1986).
7. The largest body of work was described at the LLNL Medium-Average Power Conferences. Compendia of that work appear in the Lawrence Livermore National Laboratory Laser Program Annual Reports 1985–1987.
8. Product of Hoya Optics, Inc., 3400 Edison Way, Fremont, CA 94538. Use of a particular product does indicate endorsement by the University of Rochester.
9. D. C. Brown, in *High-Peak-Power Nd:Glass Laser Systems*, Springer Series in Optical Sciences, edited by D. L. MacAdam (Springer-Verlag, Berlin, 1981), Vol. 25, p. 45.
10. J. H. Kelly, D. C. Brown, J. A. Abate, and K. Teegarden, Appl. Opt. **20**, 1595 (1981).
11. M. J. Minot, J. Opt. Soc. Am. **66**, 515 (1976).
12. L. M. Cook *et al.*, Appl. Opt. **21**, 1482 (1982).
13. W. W. Simmons and W. E. Warren, in *Modeling and Simulation of Optoelectronic Systems*, edited by J. D. O'Keefe (SPIE, Bellingham, WA, 1986), Vol. 642, p. 166. Available as a Lawrence Livermore National Laboratory Report UCRL-94380 (1986).
14. This is conservative. Preferential deposition of energy near the slab faces due to Beer's law absorption helps the thermal loading problem. See J. B. Trenholme, Lawrence Livermore National Laboratory Laser Program Annual Report 1982, UCRL-50021-82 (1983), p. 7-112.
15. W. F. Krupke *et al.*, J. Opt. Soc. Am. B **3**, 102 (1986).
16. M. S. Mangir and D. A. Rockwell, IEEE J. Quantum Electron. **QE-22**, 574 (1986).
17. J. Rinefierd, S. D. Jacobs, D. Brown, J. Abate, O. Lewis, and H. Applebaum, Laboratory for Laser Energetics Report No. 82, 1978 (unpublished).
18. W. F. Hagen and M. O. Riley, Lawrence Livermore National Laboratory Laser Program Annual Report 1985, UCRL-50021-85 (1986), p. 9-69.
19. M. A. Summers, Medium Average Power Solid State Laser Technical Information Seminar, Lawrence Livermore National Laboratory, Livermore, CA, 4 November 1988.
20. Hoya Optics Inc. product literature, 3400 Edison Way, Fremont, CA 94538.
21. The code used here is an upgraded version of the ZAP Laser Analysis Program written by J. H. Alexander, M. Froost, and J. E. Welch, ARPA Order No. 660, Contract No. N00014-70-C-0341 (June 1971).
22. A. C. Erlandson, Lawrence Livermore National Laboratory Laser Program Annual Report 1985, UCRL 50021-85 (1986), p. 7-20.
23. Technical Bulletin 2, ILC Technology, 399 Java Drive, Sunnyvale, CA 94089.
24. Product of Corning Glass Works, Corning, NY 14831.
25. J. H. Kelly, D. L. Smith, J.-C. Lee, S. D. Jacobs, M. J. Shoup, III, and D. J. Smith, in *Conference on Lasers and Electro-Optics*, Vol. 7, 1988 OSA Technical Digest Series (Optical Society of America, Washington, DC, 1988), p. 380.
26. W. M. Kays and M. E. Crawford, *Convective Heat and Mass Transfer*, 2nd ed. (McGraw-Hill, New York, 1980).
27. F. P. Incropera and D. P. Dewitt, *Fundamentals of Heat and Mass Transfer* (Wiley, New York, 1985).
28. J. M. Eggleston and M. J. Kushner, Opt. Lett. **12**, 410 (1987).
29. J. F. Reintjes, "Stimulated Raman and Brillouin Scattering," in *CRC Handbook of Laser Science and Technology*, Supplement 2: Optical Materials, edited by M. J. Weber (CRC Press, Boca Raton, FL, 1995), Sec. 8, p. 358, Table 8.3.7.
30. These numbers were taken from Ref. 29 and corrected by the factor $\cos(\pi/4)$ to obtain the transverse gain.
31. W. Kaiser and M. Maier, in *Laser Handbook*, edited by F. T. Arecchi and E. O. Schulz-Dubois (North-Holland, Amsterdam, 1972), Vol. 2, p. 1077.
32. J. M. Eggleston *et al.*, Opt. Lett. **7**, 405 (1982).
33. Product of General Electric Company, Silicon Products Division, Naperville, IL 60540.

34. G. J. DeSalvo and J. A. Swanson, Swanson Analysis Systems, Inc. (1 June 1985). (ANSYS is a registered trademark of Swanson Analysis Systems, Inc., Johnson Road, Houston, PA 15342).

35. Product of United Detector Technologies, 12525 Chadron Avenue, Hawthorne, CA 90250.

36. Product of Amoco Laser Company, 1251 Frontenac Road, Naperville, IL 60540.

37. Product of Schott Technologies, Inc., 400 York Avenue, Duryea, PA 18462.

38. M. Takeda, H. Ina, and S. Kobayashi, J. Opt. Soc. Am **72**, 156 (1982).

39. Laboratory for Laser Energetics LLE Review **31**, NTIS document No. DOE/DP/40200-47, 1987 (unpublished), p. 114.

40. R. S. Craxton, IEEE J. Quantum Electron. **QE-17**, 1771 (1981).

Laser Facility Report

This report summarizes activities on the OMEGA laser system for FY96—the first full year of operations. The format for operations has been to allocate laser time to experimental programs in single-week units of nominally 20 target shots. Many experimental programs were supported on the facility, as well as several laser enhancement projects. FY96 laser improvements included 2-D SSD, backlighter, pulse shaping, and an integrated hardware timing system.

The first quarter of FY96 was devoted to activating SSD beam smoothing on OMEGA. The initial plan of implementation of 1-D SSD (LLE U2 Program) was expanded to encompass the full capability of 2-D SSD (LLE U3 Program). This effort required the full resources of the laser drivers and precluded the use of OMEGA for target shots. The objectives of installation, integration, and activation were met, bringing the 2-D smoothing effect to target, combined with DPP[1] beam uniformity enhancements.

Second-quarter accomplishments included the activation of a third laser source capable of feeding the OMEGA beamlines as a backlighter. This wholly separate laser system—the backlighter driver—can feed 20 beams of OMEGA with one pulse shape, while the other 40 beams are fed by either the SSD or main driver. A large proportion of the planar-foil backlit beam imprinting and acceleration target shots used this flexible feature of OMEGA.

Pulse shaping was added to the OMEGA laser system during the third quarter FY96. This system allows the generation of selected temporal pulse shapes from 180-ps to 3-ns duration. Each input pulse shape design compensates for frequency conversion and gain saturation effects in the OMEGA system. The leading edge of the laser pulse experiences the largest gain and the rest of the pulse has a gain related to the cumulative amount of energy preceding it. Precompensation is accomplished by applying a specific voltage to an integrated optical waveguide modulator that shapes an optical pulse in such a way that when injected into the system produces the desired pulse shape on target.

Target interaction experiments were divided among a number of internal LLE campaigns and external NLUF and National Laboratory users. Internal campaigns followed the LLE Program Plan, which is summarized in Table 68.VII (see. p. 226).

In summary, 30 weeks of FY96 were used for target shots and 22 weeks were dedicated to modifying the laser for increased uniformity and functionality. During the 30 weeks of target shooting, 588 individual target shots were taken (average of 20/week). Of the 22 weeks when targets were not shot, 14 were used for the U2/U3 Program, 4 for activation of pulse shaping, and 4 for maintenance and laser calibration shots.

The shot summary for OMEGA for FY96 is as follows:

Driver	900
Beamline	221
Target	588
Total	1709

REFERENCES

1. Laboratory for Laser Energetics LLE Review **65**, NTIS document No. DOE/SF/19460-117, 1996 (unpublished), p. 1.

Table 68.VII: LLE Program Plan

Laser Physics Programs		Progress summary
PB1	Demonstration of 3%–4% rms beam-to-beam energy balance	Complete
U1	Implementation of optimized distributed phase plates (DPP)	Initial 60-beam experiments completed; manufacturing problems caused premature damage of epoxy DPP's. Replacement with ion-etched DPP's is planned for FY97.
U2	Implementation of 1-D SSD	Complete
U3	Implementation of 2-D SSD	Interim bandwidth of 0.6×1.5 Å complete
U4	Implementation of polarization rotators	Prototype complete and tested
PS1	Temporal pulse shapes on target with contrast ratios of 20:1	Complete
Target Physics Programs		
PP2	Implosion experiments with varying convergence ratio	Supported with 60-beam shots
S1	Planar-foil Rayleigh-Taylor growth-rate experiments	Supported with backlighter, pulse shaping, and SSD
S2	Planar-foil imprinting experiments	Supported with backlighter, pulse shaping, and SSD
S3	Spherical hydrodynamic stability experiments	Supported with pulse shaping and SSD, 60-beams shots
HE1	Surrogate (noncryogenic) hydrodynamic-equivalent experiments	Supported with 60-beam shots
NLUF	Proposals as reported in LLE Review	Supported several users with target shots
ID	Indirect drive on OMEGA	Proof-of-principle experiment completed

NLUF NEWS

Proposals for FY96

Nine proposals were submitted for consideration by the NLUF Steering Committee for FY96. The proposals included four for x-ray spectroscopy and one each for cryogenic target characterization; nuclear calibration; hohlraum diagnostic development; high-resolution, low-energy x-ray imaging of laser-irradiation imprinting; and optical imaging of the critical surface. These proposals were reviewed on 20 December 1995 by the following technical committee:

Dr. John Apruzese	(Naval Research Laboratory)
Dr. Joseph D. Kilkenny	(Lawrence Livermore National Laboratory)
Dr. Jeffrey P. Quintenz	(Sandia National Laboratory)

Approved proposals are listed in Table 68.VIII.

The OMEGA shots for proposals by Prof. Griem, Dr. Seely, and Prof. Hooper were carried out, and their FY96 activities on OMEGA are essentially complete. Professor Padalino's work on nuclear diagnostics calibration at SUNY Geneseo is also nearly completed. Professor Su is continuing to analyze the results of OMEGA experiments, and Prof. MacFarlane has shots scheduled on the Nova facility under an NLUF grant. Professor Mizuno's work on OMEGA will begin when appropriate long-scale-length plasma conditions are generated and characterized on OMEGA.

Table 68.VIII: Approved FY96 NLUF proposals.

Proposal Number	Principal Investigator	Institution	Proposal Title
194	Hans R. Griem	University of Maryland	Electric Field Measurements from Satellites to Forbidden Line Ratios in an OMEGA Upgrade Laser-Produced Plasma
196	Stephen Padalino	State University of New York at Geneseo	Calibration of Neutron Diagnostics for OMEGA
197	Joseph J. MacFarlane	University of Wisconsin, Madison	Development of Soft X-Ray Tracer Diagnostics for Holhlraum Experiments
199	John F. Seely	Naval Research Laboratory	High-Resolution Imaging of Early-Time Imprinting Using Normal-Incidence Multilayer Mirrors
200	Qichang Su	Illinois State University	Diagnostics of Core-Shell Mixing with Absorption and Emission Spectra of a Doped Layer
201	Katsuhiro Mizuno	University of California, Davis	Applications to Optical Micrograph Image Diagnostic, and Instability at the Quarter Critical Density
202	Charles F. Hooper, Jr.	University of Florida	Time-Resolved Plasma Spectroscopy of Imploded Gas-Filled Microballoons: Continuum Lowering and Pusher Dynamics

Proposals for FY97

Seven proposals were submitted to NLUF for FY97. The proposals included two experiments on x-ray spectroscopy from imploded capsules, two on laser scattering in long-scale-length plasmas, and one each on diagnostics for laser-beam-imprinting studies, studies of the nonlinearity of free space, and x-ray polarization. The proposals were reviewed on 8 August 1996 by the following technical committee:

Dr. John Apruzese	(Naval Research Laboratory)
Prof. Tudor Johnston	(Institut National de la Recherche Scientifique)
Dr. Kevin McGuire	(Princeton University)
Dr. Richard Petrasso	(Massachusetts Institute of Technology)

The committee approved five proposals for funding as shown on Table 68.IX

Table 68.IX: Approved FY97 NLUF proposals.

Proposal Number	Principal Investigator	Institution	Proposal Title
203	R. Paul Drake	University of Michigan	Laser Scattering from Long-Scale-Length Plasmas on OMEGA
204	Charles F. Hooper, Jr.	University of Florida	Time-Resolved Plasma Spectroscopy of Imploded Gas-Filled Microballoons: Emphasis on Two-Temperature Diagnostics, Line Shifts, and Pusher Dynamics
205	John F. Seely	Naval Research Laboratory	Study of 2-D Laser-Beam Imprinting Using a Double-Crystal Monochromator
206	Steven H. Batha	Fusion Physics and Technology	Is Filamentation the Origin of Stimulated Raman Scattering (SRS)? The Spatial Coherence of SRS
207	Hans R. Griem	University of Maryland	Early-Time Measurements of Soft X-Ray Emissions in an OMEGA Upgrade Laser-Produced Plasma

Publications and Conference Presentations

Publications

S.-H. Chen, J. C. Mastrangelo, T. N. Blanton, A. Bashir-Hashemi, and K. L. Marshall, "Novel Glass-Forming Liquid Crystals. IV. Effects of Central Core and Pendant Group on Vitrification and Morphological Stability," Liq. Cryst. **21**, 683 (1996).

C. T. Cotton, "Design of an All-Spherical, Three-Mirror, Off-Axis Telescope Objective," in *OSA Proceedings of the International Optical Design Conference*, edited by G. W. Forbes (Optical Society of America, Washington, DC, 1994), Vol. 22, pp. 349–351.

D. Golini, S. Jacobs, Y. Zhou, E. Fess, and M. Atwood, "Aspheric Surface Generation Requirements for Magnetorheological Finishing," in *OSA TOPS on Extreme Ultraviolet Lithography, 1996*, edited by G. D. Kubiak and D. Kania (Optical Society of America, Washington, DC, 1996), Vol. 4, pp. 98–102.

S. D. Jacobs, B. E. Gillman, J. C. Lambropoulos, T. Fang, Y. Zhou, D. Golini, and M. Atwood, "The Effect of the Coolant on the Glass Work and the Diamond Tool in Deterministic Microgrinding," in *Precision Grinding of Brittle Materials* (ASPE, Raleigh, NC, 1996), pp. 121–126.

Y. Lin, T. J. Kessler, and G. N. Lawrence, "Design of Continuous Surface-Relief Phase Plates by Surface-Based Simulated Annealing to Achieve Control of Focal-Plane Irradiance," Opt. Lett. **21**, 1703 (1996).

C. J. McKinstrie and E. A. Startsev, "Electron Acceleration by a Laser Pulse in a Plasma," Phys. Rev. E **54**, R1070 (1996).

C. I. Moore, J. P. Knauer, and D. D. Meyerhofer, "Reply to Comment on 'Observation of the Transition from Thomson to Compton Scattering in Multiphoton Interactions with Low-Energy Electrons'," Phys. Rev. Lett. **77**, 2335 (1996).

J. D. Schnittman and R. S. Craxton, "Indirect-Drive Radiation Uniformity in Tetrahedral Hohlraums," Phys. Plasmas **3**, 3786 (1996).

F. Yang, J. Y. Zhou, V. Kordonski, and S. D. Jacobs, "Indentation Size Effect of Thermoset Polymer: Allyl Diglycol Carbonate (CR-39)," J. Mater. Sci. Lett. **15**, 1523 (1996).

Forthcoming Publications

E. L. Alfonso, S.-H. Chen, M. D. Wittman, S. Papernov, and D. Harding, "A Parametric Study of Microencapsulation Approach to the Preparation of Polystyrene Shells," to be published in Polymer.

R. Betti, V. N. Goncharov, R. L. McCrory, and C. P. Verdon, "Linear Theory of the Ablative Rayleigh-Taylor Instability," to be published in the Proceedings of the 24th ECLIM, Madrid, Spain, 3–7 June 1996.

T. R. Boehly, D. L. Brown, R. S. Craxton, R. L. Keck, J. P. Knauer, J. H. Kelly, T. J. Kessler, S. A. Kumpan, S. J. Loucks, S. A. Letzring, F. J. Marshall, R. L. McCrory, S. F. B. Morse, W. Seka, J. M. Soures, and C. P. Verdon, "Initial Performance Results of the OMEGA Laser System," to be published in Optics Communications.

S.-H. Chen, J. C. Mastrangelo, H. Shi, T. N. Blanton, and A. Bashir-Hashemi, "Novel Glass-Forming Organic Materials.

3. Cubane with Pendant Nematogens, Carbazole, and Disperse Red 1," to be published in Macromolecules.

S.-H. Chen, H. Shi, B. M. Conger, D. Katsis, and J. C. Mastrangelo, "Novel Vitrified Liquid Crystals and Potential Applications," to be published in the Proceedings of the Materials Research Society 1996 Spring Meeting, San Francisco, CA, 8–12 April 1996.

S.-H. Chen, H. Shi, B. M. Conger, J. C. Mastrangelo, and T. Tsutsi, "Novel Vitrifiable Liquid Crystals as Optical Materials," to be published in Advanced Materials.

S.-H. Chen, H. Shi, J. C. Mastrangelo, and J. J. Ou, "Thermotropic Chiral Nematic Side-Chain Polymers and Cyclic Oligomers," to be published in Progress in Polymer Science.

A. V. Chirokikh, W. Seka, A. Simon, and R. S. Craxton, "Brillouin Scattering in Long-Scale-Length Laser Plasmas," to be published in Physics of Plasmas.

B. M. Conger, H. Shi, S.-H. Chen, and T. Tsutsui, "Polarized Fluorescence from Vitrified Liquid Crystalline Films," to be published in the Proceedings of the Materials Research Society 1996 Spring Meeting, San Francisco, CA, 8–12 April 1996.

B. DeMarco, C. W. Barnes, K. Kearney, and R. L. Kremens, "Neutron Yield Measurement on the OMEGA Laser System," to be published in the Review of Scientific Instruments.

R. Epstein, "Properties of the Speckle of Focused, Phase-Converted Laser Beams and the Reduction of Time-Averaged Irradiation Nonuniformity in Laser-Driven Plasmas due to Target Ablation," to be published in the Journal of Applied Physics.

P. M. Fauchet, "Photoluminescence and Electroluminescence from Porous Silicon," to be published in the Journal of Photoluminescence (invited).

P. M. Fauchet, "Porous Silicon: Photoluminescence and Electroluminescent Devices," to be published in the Light Emission in Silicon, Semiconductors, and Semimetals Series.

P. M. Fauchet, Ju. V. Vandyshev, Z. Xu, C. W. Rella, H. A. Schwettman, and G. W. Wicks, "Mid-Infrared Femtosecond Spectroscopy of Intersubband Hot Hole Relaxation in Quantum Wells," to be published in the Proceedings of OSA's Tenth International Topical Meeting on Ultrafast Phenomena, San Diego, CA, 28 May–1 June 1996.

D. Fried, R. E. Glena, J. D. B. Featherstone, and W. Seka, "Permanent and Transient Changes in the Reflectance of CO_2 Laser-Irradiated Dental Hard Tissues at $\lambda = 9.3$, 9.6, 10.3, and 10.6 μm and at Fluences between 1–20 J/cm^2," to be published in Lasers in Surgery and Medicine.

V. N. Goncharov, R. Betti, R. L. McCrory, and C. P. Verdon, "Self-Consistent Stability Analysis of Ablation Fronts with Small Froude Numbers," to be published in Physics of Plasmas.

V. N. Goncharov and R. Betti, "Growth Rate of the Ablative Rayleigh-Taylor Instability for Indirect-Drive ICF," to be published in Physics of Plasmas.

M. J. Guardalben, "Canoscopic Alignment Methods for Birefringent Optical Elements in Fusion Lasers," to be published in Optics & Photonics News.

O. E. Hanuch, V. B. Agrawal, S. Papernov, M. delCerro, and J. V. Aquavella, "Posterior Capsular Polishing with the Nd:YLF Picosecond Laser: Model Eye Study," to be published in Investigative Ophthalmology.

D. Jacobs-Perkins, M. Currie, C.-C. Wang, C. Williams, W. R. Donaldson, R. Sobolewski, and T. Y. Hsiang, "Subpicosecond Imaging System Based on Electro-Optic Effect," to be published in the IEEE Journal on Selected Topics in Quantum Electronics.

J. H. Kelly, T. R. Boehly, J. M. Soures, D. L. Brown, R. Boni, R. S. Craxton, R. L. Keck, T. J. Kessler, R. Kremens, S. A. Kumpan, S. A. Letzring, S. J. Loucks, R. L. McCrory, S. F. B. Morse, W. Seka, S. Skupsky, and C. P. Verdon, "The Activation of the Upgraded OMEGA Laser at the University of Rochester," to be published in the SPIE Proceedings of the 15th International Conference on Coherent and Nonlinear Optics, St. Petersburg, Russia, June 1995.

J. H. Kelly, T. R. Boehly, J. M. Soures, D. L. Brown, R. Boni, R. S. Craxton, R. L. Keck, T. J. Kessler, R. L. Kremens, S. A. Kumpan, S. A. Letzring, S. J. Loucks, R. L. McCrory, S. F. B. Morse, W. Seka, S. Skupsky, and C. P. Verdon, "The Activation of the Upgraded OMEGA Laser at the University of Rochester," to be published in the SPIE Proceedings of the 1st Annual International Conference on Solid-State Lasers for Application to Inertial Confinement Fusion (ICF), Monterey, CA, 30 May–2 June 1995.

O. A. Konoplev and D. D. Meyerhofer, "Cancellation of *B*-Integral Accumulation in CPA Lasers," to be published in the Proceedings of OSA's Tenth International Topical Meeting on Ultrafast Phenomena, San Diego, CA, 28 May–1 June 1996.

E. M. Korenic, S. D. Jacobs, S. M. Faris, and L. Li, "Colorimetry of Cholesteric Liquid Crystals," to be published in the Bulletin of the American Physical Society.

K. S. Lebedev, E. A. Magulariya, S. G. Lukishova, S. V. Belyaev, N. V. Malimonenko, and A. W. Schmid, "Reflective Nonlinearities of Nonabsorbing Chiral Liquid Crystals: Frustration of Selective Reflection by Powerful Laser Radiation," to be published in the Bulletin of the American Physical Society.

M. Lindgren, M. Currie, C. Williams, T. Y. Hsiang, P. M. Fauchet, R. Sobolewski, S. H. Moffat, R. A. Hughes, J. S. Preston, and F. A. Hegmann, "Intrinsic Photoresponse of a Y-Ba-Cu-O Superconductor," to be published in Physical Review Letters.

M. Lindgren, M. Currie, C. Williams, T. Y. Hsiang, P. M. Fauchet, S. H. Moffat, R. A. Hughes, J. S. Preston, and F. A. Hegmann, "Ultrafast Photoresponse and Pulse Propagation in High-T_c Superconducting Y-Ba-Cu-O Thin-Film Devices," to be published in the IEEE Journal on Selected Topics in Quantum Electronics.

S. G. Lukishova, S. V. Belyaev, K. S. Lebedev, E. A. Magulariya, A. W. Schmid, and N. V. Malimonenko, "cw and High-Repetition-Rate Lasing in Nd:YAG Resonators with Chiral-Nematic Liquid-Crystal Mirrors: A Study of Nonlinear Responses," to be published in Quantum Electronics.

S. G. Lukishova, S. V. Belyaev, K. S. Lebedev, E. A. Magulariya, A. W. Schmid, and N. V. Malimonenko, "Nonlinear Bleaching in the Selective Reflection of Nonabsorbing Chiral-Nematic Liquid-Crystal Thin Films," to be published in JETP Letters and in Molecular Crystals and Liquid Crystals.

F. J. Marshall and J. A. Oertel, "A Framed Monochromatic X-Ray Microscope for ICF," to be published in the Review of Scientific Instruments.

J. C. Mastrangelo and S.-H. Chen, "Novel Glass-Forming Organic Materials. 2. Cyclohexane and Bicyclooctene with Pendant Pyrenene and Carbazole," to be published in Chemistry of Materials.

J. C. Mastrangelo, S.-H. Chen, T. N. Blanton, and A. Bashir-Hashemi, "Vitrification and Morphological Stability of Liquid Crystals," to be published in the Proceedings of the Materials Research Society Symposium Proceedings 1996 Spring Meeting, San Francisco, CA, 8–12 April 1996.

S. M. McCormack, D. Fried, J. D. B. Featherstone, R. E. Glena, and W. Seka, "Scanning Electron Microscope Observations of CO_2 Laser Effects on Dental Enamel," to be published in the Journal of Dental Research.

R. L. McCrory, "The LLE Direct-Drive Target Physics Experimental Program: First Year of ICF Experiments on OMEGA," to be published in the Proceedings of the 24th ECLIM, Madrid, Spain, 3–7 June 1996 (invited).

C. J. McKinstrie and E. J. Turano, "Spatiotemporal Evolution of Parametric Instabilities Driven by Short Laser Pulses: One Dimensional Analysis," to be published in Physics of Plasmas.

C. J. McKinstrie, V. A. Smalyuk, R. E. Giacone, and H. X. Vu, "Power Transfer between Crossed Laser Beams and the Associated Frequency Cascade," to be published in Physical Review E.

A. Okishev, M. D. Skeldon, S. A. Letzring, W. R. Donaldson, A. Babushkin, and W. Seka, "The Pulse-Shaping System for the 60-Beam, 30-kJ (UV) OMEGA Laser," to be published in the Proceedings of Laser Optics '95 Conference, St. Petersburg, Russia, 27 June–1 July 1995.

A. Okishev and W. Seka, "Diode-Pumped Single-Frequency Nd:YLF Laser for the 60-Beam OMEGA Laser Pulse-Shaping System," to be published in Solid State Lasers VI.

R. D. Petrasso, C. K. Li, M. D. Cable, S. M. Pollaine, S. W. Haan, T. P. Bernat, J. D. Kilkenny, S. Cremer, J. P. Knauer, C. P. Verdon, and R. L. Kremens, "Implosion Symmetry and ρR Measurements of the National Ignition Facility from Nascent 31-MeV Tertiary Protons," to be published in Physical Review Letters.

J. Z. Roach, A. Ninkov, S. W. Swales, and T. Morris, "Design and Evaluation of a Screen CCD Imaging System," to be published in Optical Engineering.

J. Z. Roach and S. W. Swales, "A Network-Based Imaging System for the OMEGA Laser System," to be published in SPIE's Proceedings of the European Symposium on Lasers, Optics, and Vision for Productivity in Manufacturing I, Micropolis, Besangon, France, 10–14 June 1996.

A. W. Schmid, T. J. Kessler, S. Papernov, and J. Barone, "Low-Surface-Energy Photoresist as a Medium for Optical Replication," to be published in Applied Physics Letters.

H. Shi, D. Katsis, and S.-H. Chen, "Dynamics of Defect Annihilation in Vitrified Liquid Crystalline (VLC) Thin Films," to be published in the Proceedings of the Materials Research Society 1996 Spring Meeting, San Francisco, CA, 8–12 April 1996.

H. Shi and S.-H. Chen, "Theory of Circularly Polarized Light Emission from Chiral Nematic Liquid Crystalline Films," to be published in the Proceedings of the Materials Research Society 1996 Spring Meeting, San Francisco, CA, 8–12 April 1996.

M. J. Shoup III, J. H. Kelly, and D. L. Smith, "Design and Testing of a Large-Aperture, High-Gain, Brewster's-Angle Zigzag Nd:Glass Slab Amplifier," to be published in Applied Optics.

A. Simon, "Comparison Between SBS Theories and Experiment," to be published in the Proceedings of the LaJolla Summer School '95, Plasma Physics and Technology (AIP).

J. M. Soures, S. J. Loucks, R. L. McCrory, C. P. Verdon, A. Babushkin, R. E. Bahr, T. R. Boehly, R. Boni, D. K. Bradley, D. L. Brown, J. A. Delettrez, R. S. Craxton, W. R. Donaldson, R. Epstein, R. Gram, D. R. Harding, P. A. Jaanimagi, S. D. Jacobs, K. Kearney, R. L. Keck, J. H. Kelly, T. J. Kessler, R. L. Kremens, J. P. Knauer, S. A. Letzring, D. J. Lonobile, L. D. Lund, F. J. Marshall, P. W. McKenty, D. D. Meyerhofer, S. F. B. Morse, A. Okishev, S. Papernov, G. Pien, W. Seka, R. W. Short, M. J. Shoup, III, M. D. Skeldon, S. Skupsky, A. W. Schmid, D. J. Smith, S. Swales, M. D. Wittman, and B. Yaakobi, "The Role of the Laboratory for Laser Energetics in the National Ignition Facility Project," to be published in Fusion Technology.

M. D. Wittman, R. Q. Gram, H. Kim, C. K. Immesoete, S. G. Noyes, and S. Scarantino, "Increased Retention Time for Hydrogen and Other Gases by Polymer Shells Using Optically Transparent Aluminum Layers," to be published in the Journal of Vacuum Science and Technology.

W. Xiong, Y. Kostoulas, X. Weng, P. M. Fauchet, and R. Sobolewski, "Femtosecond Study of the Electronic Structure in Semiconducting Y-Ba-Cu-O," to be published in Physical Review B.

Z. Xu, Ju. V. Vandyshev, P. M. Fauchet, C. W. Rella, H. A. Schwettman, and C. C. Tsai, "Ultrafast Excitation and De-excitation of Local Vibrational Modes in a Solid Matrix: The Si-H Bond in Amorphous Silicon," to be published in the Proceedings of OSA's Tenth International Topical Meeting on Ultrafast Phenomena, San Diego, CA, 28 May–1 June 1996.

B. Yaakobi, F. J. Marshall, and J. A. Delettrez, "Abel Inversion of Cryogenic Laser Target Images," to be published in Optics Communications.

B. Yaakobi, F. J. Marshall, and R. Epstein, "High Temperature of Laser-Compressed Shells Measured with Kr^{+34} and Kr^{+25} X-Ray Lines," to be published in Physical Review E.

J. D. Zuegel and W. Seka, "Direct Measurements of Lower-Level Lifetime in Nd:YLF," to be published in the Bulletin of the American Physical Society.

J. D. Zuegel and W. Seka, "Upconversion and Reduced $^4F_{3/2}$ Upper-State Lifetime in Intensely Pumped Nd:YLF," to be published in Optics Letters.

Conference Presentations

S.-H. Chen, H. Shi, B. M. Conger, and J. C. Mastrangelo, "Novel Vitrifiable Liquid Crystalline Materials," International LCD Symposium, Hsin-Chu, Taiwan, 8–9 July 1996 (invited).

D. D. Meyerhofer, "Multiphoton-Electron Scattering Experiments," International Conference on Atomic Physics, Amsterdam, Netherlands, 4–9 August 1996.

The following presentations were made at the XXI International Conference on Low Temperature Physics, Prague, Czech Republic, 8–14 August 1996:

R. Adam, W. Kula, J. M. Murduck, C. Pettiette-Hall, and R. Sobolewski, "Laser-Induced Modification of the Critical Current in Y-Ba-Cu-O Step-Edge Josephson Junctions."

M. Lindgren, M. Currie, C. Williams, S. H. Moffat, R. A. Hughes, F. A. Hegmann, J. S. Preston, T. Y. Hsiang, and R. Sobolewski, "Picosecond Photoresponse of $YBa_2Cu_3O_{7-\delta}$ Thin Films."

S. D. Jacobs and D. Golini, "Chemomechanical Aspects of Material Removal with Magnetorheological Finishing," A Workshop on Chemical-Mechanical Polishing, Lake Placid, NY, 18–21 August 1996.

M. Lindgren, M. Currie, C. Williams, S. H. Moffat, R. A. Hughes, F. A. Hegmann, J. S. Preston, T. Y. Hsiang, and R. Sobolewski, "$YBa_2Cu_3O_{7-\delta}$ Thin Film Picosecond Photodetectors," 1996 Applied Superconductivity Conference, Pittsburgh, PA, 25–30 August 1996.

The following presentations were made at the 26th Anomalous Absorption Conference, Fairbanks, AK, 26–30 August 1996:

R. Betti, R. Epstein, V. N. Goncharov, R. L. McCrory, and C. P. Verdon, "Dynamic Stability and Linear Feedthrough in ICF Implosions."

T. R. Boehly, D. D. Meyerhofer, J. P. Knauer, D. K. Bradley, R. L. Keck, J. A. Delettrez, V. A. Smalyuk, J. M. Soures, and C. P. Verdon, "Laser Imprinting Studies Using Multiple-UV-Beam Irradiation of Planar Targets."

D. K. Bradley, J. A. Delettrez, and P. A. Jaanimagi, "Initial Mix Experiments on the 60-Beam OMEGA Laser System."

R. S. Craxton and J. D. Schnittman, "Tetrahedral Hohlraums—A Way to Achieve Time-Independent Uniformity on the NIF?"

S. Cremer and S. Skupsky, "Diagnosing High-ρR Implosions Using Elastically Scattered DT Neutrons."

J. A. Delettrez, D. K. Bradley, and C. P. Verdon, "Modeling of Mix due to the Rayleigh-Taylor Instability in Burnthrough Experiments Using the One-Dimensional Hydrodynamic Code *LILAC*."

R. Epstein, "Time Averaging of Irradiation Nonuniformity in Laser-Driven Plasmas due to Target Ablation."

A. C. Gaeris, Y. Fisher, J. A. Delettrez, and D. D. Meyerhofer, "Brillouin Scattering of Picosecond Laser Pulses in Preformed, Short-Scale-Length Plasmas."

V. N. Goncharov, R. Betti, R. L. McCrory, and C. P. Verdon, "Ablative Rayleigh-Taylor Instability: Applications of the Linear Theory to Target Designs Relevant to Inertial Confinement Fusion."

C. J. McKinstrie and E. A. Startsev, "Multiple-Scale Derivation of the Relativistic Ponderomotive Force."

J. D. Schnittman and S. M. Pollaine, "Tetrahedral Hohlraums on the NIF."

W. Seka and A. V. Chirokikh, "Plasma Diagnostics on OMEGA."

R. W. Short, "Filamentation of Laser Light in Inhomogeneous Plasmas: Effects of Refraction and Plasma Flow."

A. Simon, "Raman Scattering in Gas-Filled Hohlraums and Gasbags."

V. A. Smalyuk, C. J. McKinstrie, R. E. Giacone, and H. X. Vu, "Power Exchange between Crossed Laser Beams and the Associated Frequency Cascade."

E. A. Startsev and C. J. McKinstrie, "Electron Acceleration by a Laser Pulse in a Plasma."

R. P. J. Town, R. W. Short, and C. P. Verdon, "Fokker-Planck Simulations of Foam-Buffered Targets."

E. J. Turano and C. J. McKinstrie, "Spatiotemporal Evolution of Stimulated Raman Scattering."

O. A. Konoplev, L. Zheng, and D. D. Meyerhofer, "Ultrashort-Pulse Laser Technique to Measure Crystal Axis Orientation," SOMR–96, Rochester, NY, 28 August 1996.

S. G. Lukishova, K. S. Lebedev, E. A. Magulariya, S. V. Belyaev, N. V. Malimonenko, and A. W. Schmid, "Nonlinear Bleaching of Non-absorbing Cholesteric Liquid-Crystal Mirrors by cw and Pulsed High-Power Laser Radiation," Europe-EQEC '96, Hamburg, Germany, 8–13 September 1996.

The following presentations were made at the Eleventh Target Fabrication Specialists' Meeting, Orcas Island, WA, 9–12 September 1996:

M. Bonino, R. Q. Gram, D. Harding, S. Noyes, J. Soures, and M. Wittman, "Retention of D_2 and DT in Plastic Shell Targets Using Thin Aluminum Layers."

M. D. Wittman, S. A Letzring, K. J. Lintz, S. Scarantino, D. R. Harding, S. J. Loucks, J. M. Soures, W. T. Shmayda, and R. Matsugu, "An Overview of the Tritium-Filling Capabilities at the Laboratory for Laser Energetics."

D. D. Meyerhofer, "Multiphoton-Electron Scattering Experiments," International Conference on Multiphoton Physics, Garmish-Partenkirchen, Germany, 30 September–4 October 1996.